Title
Optimization Studies of Liquid Metal Systems for a Fusion Power Reactor

Author
Jiang, Yuchen

Publication Date
2023

Peer reviewed|Thesis/dissertation

UNIVERSITY OF CALIFORNIA

Los Angeles

Optimization Studies of Liquid Metal Systems for a Fusion Power Reactor

A dissertation submitted in partial satisfaction

of the requirements for the degree

Doctor of Philosophy in Mechanical Engineering

by

Yuchen Jiang

2023

ABSTRACT OF THE DISSERTATION

Optimization Studies of Liquid Metal Systems for a Fusion Power Reactor

by

Yuchen Jiang
Doctor of Philosophy in Mechanical Engineering
University of California, Los Angeles, 2023
Professor Jeffrey D. Eldredge, Chair

In liquid metal (LM) blankets of a fusion power reactor, the fluid flow is under the influence of strong electromagnetic forces resulting from applied plasma-confining magnetic field. The two major concerns of the blanket design are: (1) the compatibility issues between structural materials and high-temperature flowing LM and, (2) high 3D Magnetohydrodynamic (MHD) pressure drop that arises from the interaction between the magnetic field and induced electric currents. To help address these issues, three topics are investigated numerically using the COMSOL Multiphysics software.

The first topic is a characterization of a LM (PbLi) flow in the thermal convection loop (TCL), which is used in the experimental corrosion studies. Two modeling tools, a thermohydraulics code and a computational model in COMSOL Multiphysics, have been developed, tested and then applied to the analysis of fluid flow and heat transfer in a TCL. Such a device has recently been used to experimentally evaluate corrosion compatibility of APMT (Fe–21Cr–5Al–3Mo) steel with high-temperature molten eutectic lead-lithium (PbLi) alloy at Oak Ridge National Lab, TN, USA. The 1D thermohydraulics code allows for rapid calculations of the loop parameters as a function of the applied heat flux. The supplemental

COMSOL finite-element computations provide detailed 3D velocity and temperature field data but are much more time consuming. Both modelling tools demonstrate an excellent agreement in the computed circulation velocity as well as maximum and minimum temperatures. The performed TCL analysis focuses on flow development in the "hot" and "cold" legs, formation of Dean vortices in corner regions, blocking effect of the immersed samples, and radiative and convective cooling effects under the experiment-relevant conditions for Prandtl number $Pr = 0.015$, Grashof numbers $Gr \sim 10^7$, and Reynolds numbers $Re \sim 10^4$.

The second topic is the optimization studies of the inlet manifold design with gradual expansion. MHD flows in a manifold of a liquid metal blanket can significantly contribute to the blanket pressure drop, which is a feasibility issue for almost all liquid metal blanket concepts. In this topic, optimization studies for a prototypic inlet manifold that feature flow expansion are performed for three expansion angles θ, $45°, 60°$ and $75°$, expansion ratio of 4, and a wide range of Hartmann (Ha) and Reynolds (Re) numbers: $1000 < Ha < 10000$, and $50 < Re < 1000$ aiming at the MHD pressure drop reduction and a more uniform flow distribution at the exit of the manifold. The 150 flow cases computed with COMSOL Multiphysics in 3D provide an extended database for the pressure drop coefficient, which is used to construct a correlation for the 3D MHD pressure drop. In addition, many data analyses were performed to characterize the flow inside the manifold and access the most important flow characteristics, such as the recirculation flow bubble that appears when the liquid metal enters the expansion region and the flow development length as a function of Ha, Re and θ.

The third topic is the LM MHD flow in blanket supply ducts where high MHD pressure drop is related to a space-varying (fringing) magnetic field. Similar to the manifold cases, high MHD pressure drop is caused by 3D MHD effects, which are studied numerically for a non-conducting rectangular duct for $1000 < Ha < 10000$, $1000 < Re < 10000$ and four values of the magnetic field gradient in the fringing field region. A total of 80 cases have been computed and the corresponding pressure drop coefficients calculated to deduce a correlation

for 3D MHD pressure drop based on linear regression analysis. Strong 3D effects have been observed in almost all computed cases as demonstrated by comparison against the quasi-fully developed MHD flow as well as the transverse pressure difference.

The dissertation of Yuchen Jiang is approved.

Xiaolin Zhong

Timothy S. Fisher

Sergey Y. Smolentsev

Jeffrey D. Eldredge, Committee Chair

University of California, Los Angeles

2023

To my family ...

who always support me

throughout my journey

TABLE OF CONTENTS

LIST OF FIGURES

LIST OF TABLES

ACKNOWLEDGMENTS

The past four years have witnessed one of the toughest challenge in my life: striving to get my Ph.D. degree. The world and myself have been through so many things but we all hanged on until brightness came. I am really grateful and I would like to express my sincere gratitude to the following individuals and organizations who have contributed significantly to the completion of this dissertation.

First and foremost, I would like to thank my academic advisor, Dr. Sergey Smolentsev, for his invaluable guidance, unwavering support, and expertise throughout this research journey. His insightful feedback and constructive criticism have been instrumental in shaping this dissertation. Apart from the rigorousness attitude towards research and patience for detailed modification of papers, Dr. Smolentsev has also helped me practiced my independent research ability as an individual, enhanced my competence of dealing with problems, and navigated me through the pandemic.

I am deeply grateful to my research committee, comprising Prof. Jeff Eldredge, Prof. Tim Fisher, and Prof. Xiaolin Zhong, for their valuable insights and thoughtful suggestions that have greatly enhanced the quality of this research work. I feel really blessed that I have the opportunity to know Prof. Eldredge, who is always kind hearted and willing to help. When I was studying as a Master student, he's really patient in answering questions and giving me viable suggestions on my future career. It was he who found me this position and gave me the chance to take myself to a higher level.

I extend my appreciation to my colleagues and fellow researchers at UCLA, whose collaboration and intellectual discussions have enriched my understanding and provided valuable perspectives. Dr. Yi Yan showed great enthusiasm to discuss fusion-related modeling and topics with me, and he also answered many vague questions related to the software COMSOL Multiphysics. I want to thank people from HyperComp Dr. Peter Huang for collaboration on the paper and comparison of data. I am also excited to know people from Oak Ridge

National Lab (ORNL) and have the honor to work on promising projects with them from Department of Energy.

I would like to acknowledge the financial support provided by the US Department of Energy under contract DE-SC0020979. Their generous grant has enabled me to conduct the necessary numerical studies and gather crucial data for this research.

Furthermore, I would like to express my heartfelt gratitude to my family and friends for their unwavering support, encouragement, and understanding. Their love and belief in my abilities have been a constant source of inspiration and motivation.

Finally, I am thankful to all the participants who volunteered their time and contributed to this study. Without their involvement and cooperation, this research would not have been possible.

VITA

2018–2020 Master's student at University of California, Los Angeles under Mechanical and Aerospace Engineering Department

2019–2023 Graduate student researcher at University of California, Los Angeles under Mechanical and Aerospace Engineering Department

PUBLICATIONS

Y. Jiang, Modeling and Simulation of a New Tethered Wind Power System, 2018 2nd International Conference on Green Energy and Applications (ICGEA), Singapore, 2018, pp. 183-187.

Y. Jiang, S. Smolentsev, J. Jun, B. Pint, C. Kessel, Prediction of PbLi fluid flow and temperature field in a thermal convection loop for qualification of fusion materials, International Journal of Heat and Mass Transfer, 172, 2021, 121198.

Y. Jiang, M. Sun, R. Xiong, Design of a noninvasive diabetes detector based on acetone recognition, Journal of Physics: Conference Series 1026, 2018,: n.pag.

S. Smolentsev, T. Rhodes, Y. Jiang, P. Huang, C. Kessel, Status and progress of liquid metal thermofluids modeling for the U.S. fusion nuclear science facility, Fusion Science and Technology, 77:7-8, 2021, 745-760.

Y. Jiang, S. Smolentsev, Optimization studies for a manifold of a liquid metal blanket of a fusion reactor, Fusion Engineering and Design, accepted with minor revision.

CHAPTER 1

Introduction

Fusion technology is a promising way of producing electricity for its clean emission and high energy density reactions. The design of liquid metal (LM) blankets used for sustainable energy conversion is among the most important engineering challenges to be addressed towards a future fusion facility. Two major concerns regarding liquid metal blanket designs are the corrosion of structural materials which jeopardizes the safety of the facility and reduces its lifetime, and high magnetohydrodynamic (MHD) pressure drop of the liquid breeder flows in the blanket conduits that may become unacceptable due to high stresses in the flow containing solid structure and a need for high pumping power.

In order to solve various engineering and scientific problems associated with the flow of electrically conducting liquid breeders (such as eutectic alloy lead lithium $PbLi$ or pure lithium Li) in the presence of a strong plasma confining magnetic field, understanding of the fluid flow behaviors in the harsh blanket environment is necessary. This includes effects of strong electromagnetic loads, high temperature and temperature gradients associated with volumetric and surface heating, electromagnetic Lorentz forces and complex blanket geometry. On the other hand, development of experimental facilities, new experiments and associated computations are also required to accomplish the major design and analysis goals. Eventually, the optimization studies would be required to further advance the liquid metal systems and improve the effectiveness of the experimental investigations.

In this dissertation, three problems related to liquid metal systems have been identified and then studied through 3D numerical computations, including the optimization analysis.

They are: (1) liquid metal flows and heat transfer in the so-called Thermal Convection Loop (TCL), which is an experimental device for studying liquid metal corrosion by generating a buoyancy-driven flow, (2) MHD flows in inlet/outlet blanket manifolds with optimized gradual expansion geometry to reduce the 3D MHD pressure drop, and (3) MHD flows in a fringing magnetic field to simulate conditions of the liquid breeder flow in the blanket supply system where high MHD pressure drops are expected due to sudden changes in the applied magnetic field. The first problem is purely hydrodynamic, while the other two are MHD problems that involve both the fluid flow (Navier-Stokes) and electromagnetic (Maxwell) equations. The proposed analyses include numerical computations and also development of pressure drop correlations that can be used by blanket engineers and designers. By characterizing the flow patterns in complex shape blanket conduits and associated MHD flow pressure drops, a better understanding of the blanket physics can be achieved that would eventually help in the development of a robust blanket design. The pressure drop correlations are useful in optimizing piping systems of a blanket to reduce the required pumping power, thus reducing the electricity cost. Using such correlations is much easier compared to the expansive full 3D numerical computations for the entire blanket circuit. The data and correlations acquired are generic and can be used in the design process of any liquid metal blanket.

CHAPTER 2

Literature review

2.1 Background of fusion reactor and fusion blanket concepts

As an explanation to reveal the importance of understanding physics in MHD flow within fusion power reactors, a brief introduction to the fusion nuclear reactor is provided. Different from nuclear fission where single heavy nuclei are split apart in a small reaction to release energy, nuclear fusion involves the combination of two light nuclei to form a heavier nuclei, and thus converting mass to energy. Even though the mass difference of single tiny reaction is infinitesimal, the Einstein's famous equation $E = mc^2$ tells that the total energy generated by all same reactions combined would be enormous. The most straightforward creations of this type of process are the sun and stars in the galaxy. Based on the choices of light nuclide, various fusion reactions can be realized, among which the Deuterium (D)-Tritium (T) cycle grabs attention around the world. D and T are hydrogen isotopes and can be fused to produce energy and maintain the reaction process. The process can be expressed by ${}^{2}_{1}H(D) + {}^{3}_{1}H(T) \rightarrow {}^{4}_{2}He(\alpha) + {}^{1}_{0}n + 17.58MeV$ with neutron kinetic energy of $14.06MeV$ and alpha particle kinetic energy of $3.52MeV$. To make the process possible, tritium which doesn't exist naturally needs to be generated, in this case through neutron reaction with lithium (Li) in some form, which is why Li is a must-have in fusion reactor. In this way, enough tritium is generated to create a sustainable fuel cycle.

The plasma in a fusion reaction core can reach 100 million degrees celsius, which is extremely high and beyond imagination. Traditional materials are not able to tolerate this

condition. The most realistic approach is to apply a strong enough plasma confining magnetic field via toroidal and poloidal superconducting magnets. "Tokamak" is such a well known device and also the main study object of current fusion reactor designs. The magnetic field not only confines the hot plasma, but also prevents it from touching any structure materials.

Renewable and pollution-free energy is always seen as a necessity towards future sustainable development, with fusion reactor being a long-lasting and promising way of providing electricity. For this reason, the development of a blanket system for a fusion power reactor that provides self-sufficient tritium breeding and efficient conversion of the extracted fusion energy to electricity, while meeting all design limitations is among the most vital fusion science and technology goals.

In order to meet the design requirements, different blanket concepts have been proposed around the world. From the phase type view, solid breeder blanket and liquid breeder blanket are developed. The solid breeder blanket often uses lithium ceramic (Li_2O, Li_4SiO_4, Li_2TiO_3, Li_2ZrO_3) as tritium breeder and helium or water as coolant. Liquid breeder blanket is often concerned as a suitable way of achieving the target. Inside this type of blanket, liquid metals are often used for power conversion and tritium breeding. Typical breeders include liquid metals and molten salts. Molten salts have low conductivity and high Prandtl number, but high melting point, chemistry, and tritium control problems limit their application. Liquid metals are often preferred for their high thermal conductivity and low viscosity. Candidates are pure lithium and the eutectic lead-lithium alloy. Dominant issues of using liquid metals include MHD effect, chemical reactivity (Li), and tritium permeation ($PbLi$).

Despite all mentioned concepts, there is no perfect solution. All these concepts have their own feasibility and attractiveness issues to be resolved. In this research, the focus is on liquid metal blanket design and optimization. Liquid metal blanket concepts are potentially more promising for its high heat removal, adequate tritium breeding ratio possible without beryllium neutron multiplier in liquid metals, relatively simple design, low pressure,

low pumping power, but feasibility issues arise because of existence of magnetic field, including high pressure drop due to interaction of strong plasma confining magnetic field with electrically conducting fluid, and enhanced corrosion at high operation temperature.

For liquid metal blanket design, major classifications are self-cooled blanket, separately cooled blanket and dual coolant blanket chronologically. In a self-cooled blanket, liquid breeder is circulated at high enough speed to also serve as coolant for the first wall. This is problematic for high flow rates because the large pressure drop caused by MHD effect will exceed the allowable stress limits of the structural material. Also, insulation coatings are vulnerable to cracks and cannot efficiently reduce the pressure drop. To solve this problem, Water-Cooled Lead Lithium (WCLL) blanket and Helium-Cooled Lead Lithium (HCLL) blanket were proposed, which belong to the separately cooled blanket concepts. In this type of blankets, the liquid metal is circulated only at low speed for tritium extraction while all the surface and volumetric heat is removed by a separate coolant like water or helium (He) gas. However, the separately cooled blanket concept suffers from low coolant exit temperature dictated by the maximum allowable temperature of the structural material. Moreover, it is still subject to MHD effects due to magnetic field transients and the need to circulate the liquid metal for tritium recovery. In order to compensate for the defects of these two concepts, dual coolant blanket concept was introduced, where the first wall and structure are cooled with separate coolant (He) while the liquid metal is used for "self-cooling" in the breeder zone.

The detailed illustrations of examples of each liquid metal blanket type are as follows: Figure 2.1 shows the US self-cooled lithium/vanadium blanket, which is composed of oblique poloidal manifolds and toroidal channels. The function of the toroidal ones where lithium flows in a velocity up to $1m/s$ is to protect the poloidal manifolds from surface heat flux as well as volumetric heating. The manifolds are designed to have larger cross section area to reduce pressure drop. Nevertheless, the biggest pressure drop occurs when the toroidal channels turn into poloidal direction. Insulating coatings were considered but were not

tolerant enough to small defects. The HCLL blanket design is demonstrated in Figure 2.2.

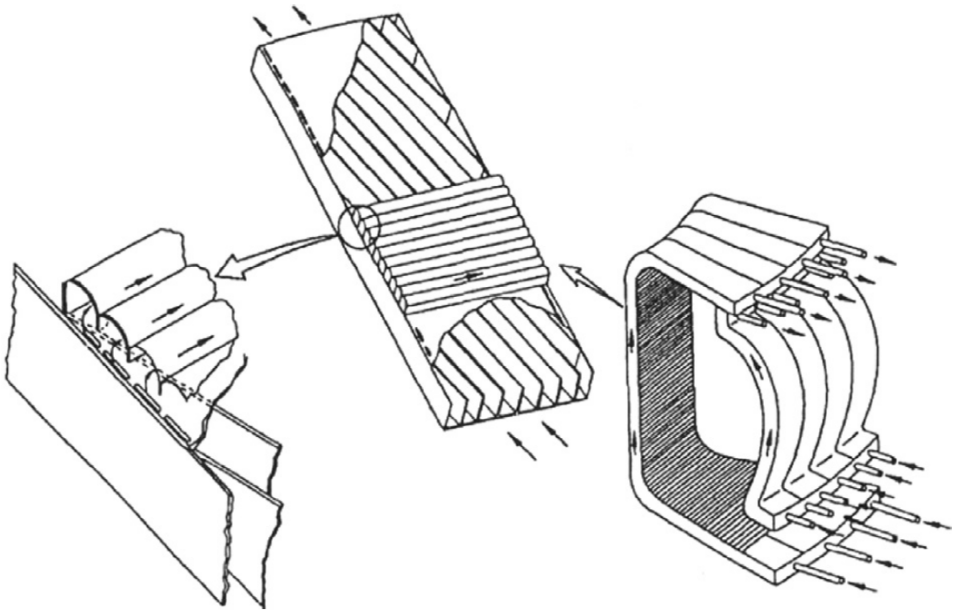

Figure 2.1: Self-cooled lithium/vanadium blanket (poloidal/toroidal flow).

It utilizes the available structure and materials but requires $PbLi$ to flow in a slow velocity ($1mm/s$) while using He for cooling purpose. Due to the relatively larger velocity in the feeding system compared to the ducts, the pressure drop is high and possibly stagnant flow will cause tritium permeation from $PbLi$ to He, therefore resulting in low thermal efficiency and high tritium loss. The WCLL blanket is similar as the HCLL blanket, except using water as coolant to remove heat, with illustration shown in Figure 2.3. This type of design is considered applicable to EU DEMO reactor and also a possible candidate of ITER. As shown in the figure, the $PbLi$ flow slowly recirculates in the blanket with a velocity of $1mm/s$. All heat generated in the blanket is absorbed by water flowing in numerous double-walled tubes. Tritium needs to be extracted from both water and liquid metal. The major drawback of this blanket is safety issues associated with hydrogen generation in case of water-lithium reactions. Finally, the schematic configuration of DCLL blanket is shown in Figure 2.4. The advantages of this concept are high temperature allowance and high efficiency of the system. Basically, high temperature $PbLi$ flows at a speed around

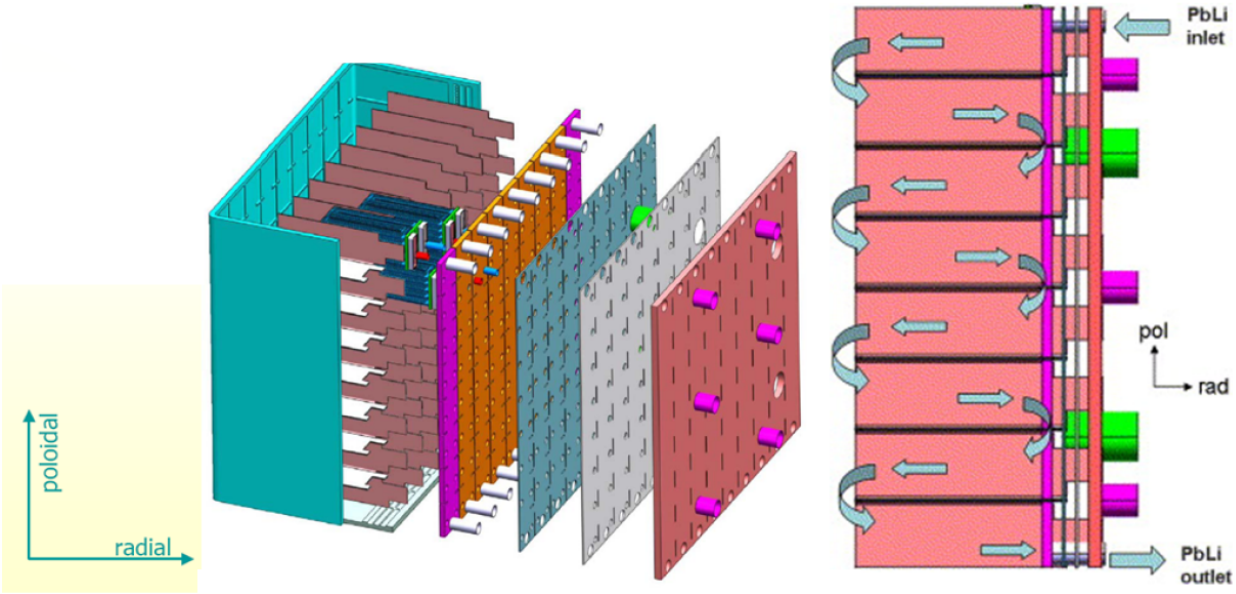

Figure 2.2: EU HCLL blanket: (left) general view, (right) *PbLi* flow path.

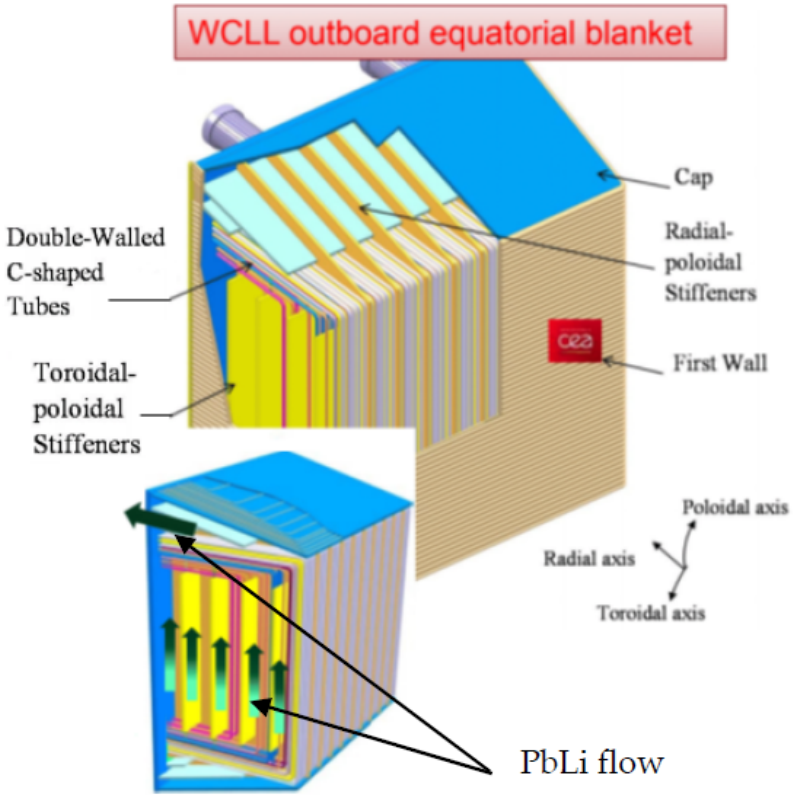

Figure 2.3: Schematics of the WCLL blanket for EU DEMO.

$10cm/s$ in large rectangular poloidal ducts, which breeds tritium and removes volumetric heat. Additionally, pressurized He gas is used solely to lower the temperature of the RAFM (Reduced Activation Ferritic/Martensitic) steel wall and other structural materials under critical point. Flow channel inserts (FCI) made of SiC ceramics are placed around the flow channel for thermal and electrical insulation. There are two mainstream approaches

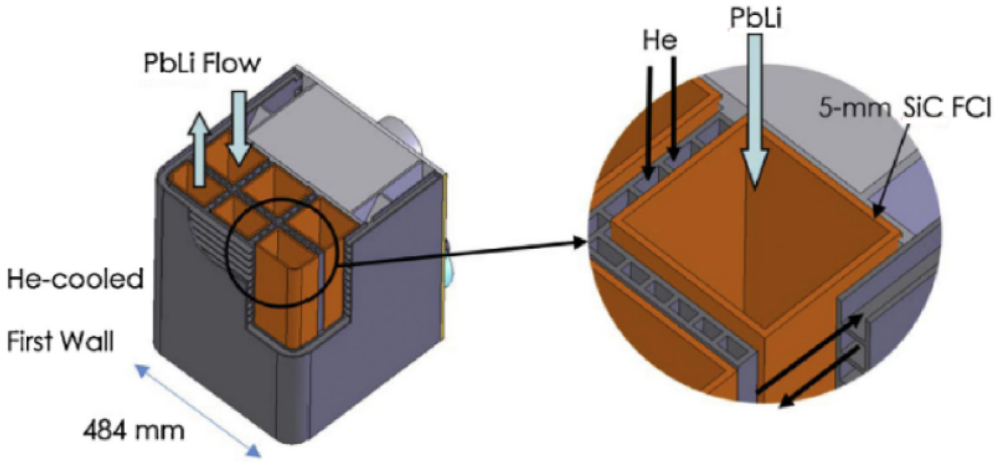

Figure 2.4: DCLL blanket with poloidal channels and SiC flow channels inserts.

for DCLL blanket. On the left of Figure 2.5 shows the so called "banana" type, with only poloidal ($10m$) channels and manifold at the bottom. The second type of blanket is shown in the right half of figure, in which modular blankets ($2m$) are piled up with shared manifold. The detailed comparison between these two types are unknown so far. As is mentioned, pressure drop originated from interaction of magnetic field with electrically conducting fluid can be the key issue of blanket design, with "Blanket Comparison and Selection Study" (BCSS) [7] limiting the maximum MHD pressure drop in a blanket to be $2MPa$. This is why feasible ways of mitigating MHD pressure drop is important. In order to achieve the goals, liquid metal magnetohydrodynamics (LM MHD) should be carefully studied. Former studies have predicted a pressure drop possibly higher than $2MPa$ for self-cooled blanket, and an overall pressure drop lower than $2MPa$ achievable for separately cooled as well as dual coolant blanket.

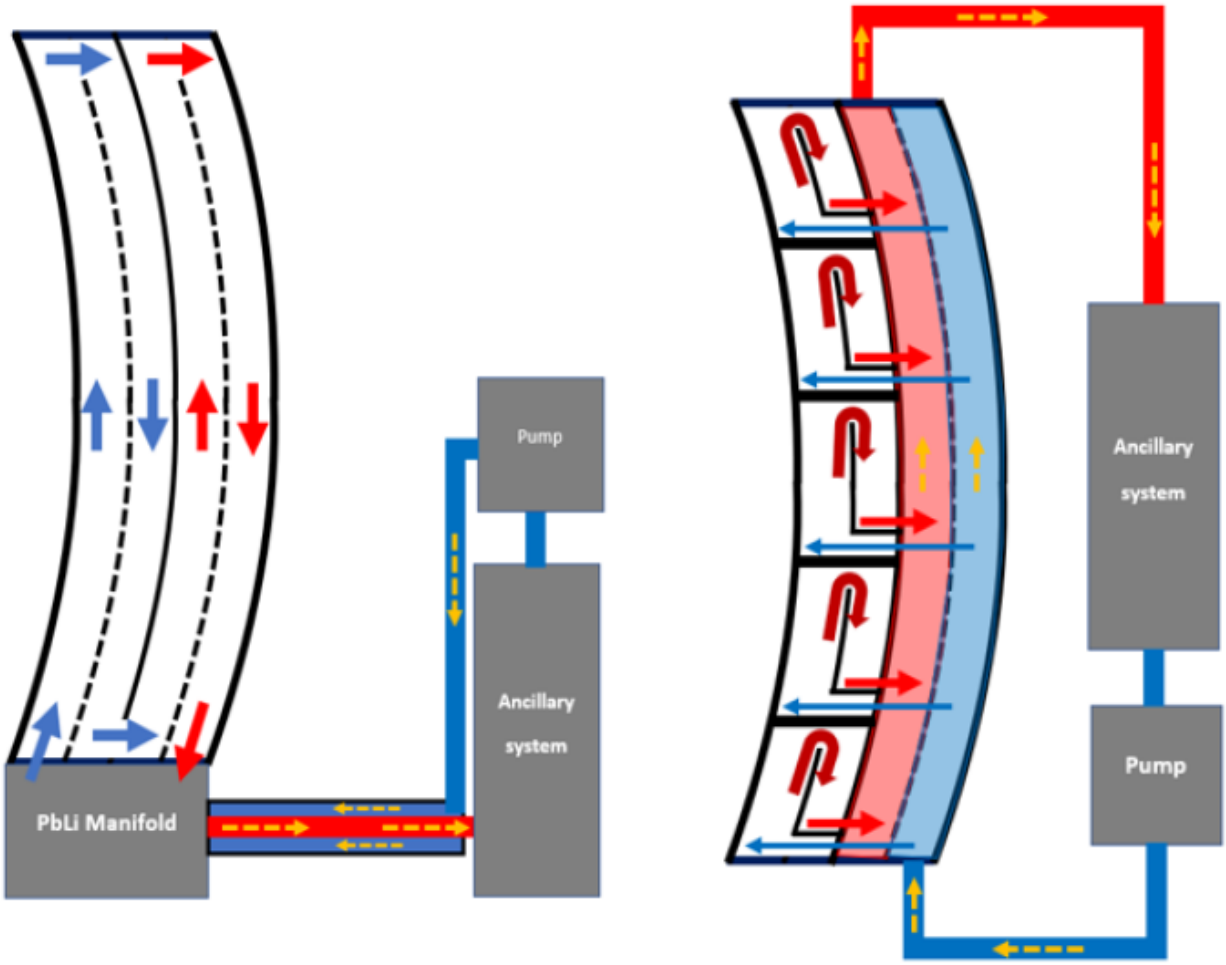

Figure 2.5: Two possible designs of the DCLL blanket, (left) full segment "banana" blanket; and (right) modular blanket.

The MHD pressure drop can originate from many sources. As a whole, the pressure drop exists in the blanket and as well in the ancillary equipment. From the fusion blanket perspective, the design of inlet/outlet manifold, the feeding pipes, the duct elbow, and the way nonuniform fringing magnetic field changes the flow can cause pressure loss. Several factors contribute to the significance of reducing pressure drop:

1. The structure material may experience excessive stress above its limit, therefore cause structure failure and key safety issues.

2. High total pumping pressure requires high power input for feeding the flow, which will diminish the energy efficiency of the blanket.

3. There is no available high capacity liquid metal pumps that can be used to compensate the high pressure drop.

Typically, the pressure drops in a blanket are caused mainly by geometric variations and magnetic field effects, which can be divided into 2D MHD pressure drop ΔP_{2D} or 3D MHD pressure drop ΔP_{3D} based on MHD flow characteristics. The 2D MHD flow occurs when the rectangular duct or circular pipe is sufficiently long under uniform transverse magnetic field so that the flow can be considered as fully-developed after certain distance. This type of flow exists in parallel poloidal ducts as well as radial supply pipes. The induced electric currents are closed loops in 2D cross-sectional planes. Therefore, the corresponding flow-opposing Lorentz force is only in the axial direction. The 2D pressure drop is caused by viscous friction and Lorentz force, with Lorentz force dominating when the duct wall is insulating due to electric current merely existing in the flow. For MHD electrically conducting walls, depending on the relative relation of wall conductance ratio and Hartmann number, the form of 2D pressure drop can be established.

Besides 2D fully developed duct flow, the MHD flow in a bend, expansion or contraction with complex geometry and altered flow direction can essentially be considered as 3D from a geometry aspect. In 3D MHD flows, three velocity components are present with mainly

axial electric current affecting the flow perpendicular to the axial direction. The axial current loop is very unique because it closes inside the fluid, therefore diminishing the effect of wall conductivity on 3D MHD flow. Also, sudden change of magnetic field, wall conductivity which will basically reshape the fully developed flow characteristics can lead to 3D MHD formation. Oftentimes, the resulting ΔP_{3D} can be comparable or even higher than ΔP_{2D} in MHD flow.

2.2 *PbLi* flow in a thermal convection loop

A Thermal Convection Loop (TCL), also known as a Natural Circulation Loop (NCL), is an experimental device, in which a circulation-type fluid flow is generated by heating and cooling some portions of a fluid-containing closed circuit. In general, the presence of a fluid density gradient in a gravitational field does not ensure the existence of a circulating flow. Therefore, natural circulation in a fluid filled closed loop is always established by placing a heat sink in the loop above the heat source, similar to natural convection. By doing this, the flow driving force is the buoyancy force associated with the difference in the fluid density between the "hot" and "cold" fluid. In engineering practices, such buoyancy-driven flow loops are considered as relatively inexpensive flow devices compared to more complicated forced convection loops where the fluid motion is driven by a pump. Depending on areas of application, there can be many TCL designs varying in dimensions, materials, heating/cooling schemes, flow configurations and type of working fluids. Due to its simplicity, low cost, noise free and maintenance free operation, thermal convection loops have been intensively used in experimental studies of fluid flow and heat/mass transfer for fission reactors [8], chemical extractors [9], electronic cooling systems [10], solar heaters [11], geothermal applications [12], cryogenic refrigeration systems [13], turbine blade cooling [14], thermosiphon reboilers [15], and refrigeration and air conditioning systems [16].

The flow and heat transfer characteristics of TCLs are illustrated in various ways, with

Sabharwall et al. [17] theoretically analyzing the stability of TCLs for liquid metal reactors. A generalized flow equation was proposed by [18] for natural convection loops with laminar and turbulent regions in the flow simultaneously and a stability map was constructed to guide the flow characterization in such loops. In the majority of related studies, a thermal convection loop was used to characterize corrosion processes of candidate materials immersed in the flowing hot liquid at various temperatures and velocities [1, 2, 19, 20, 21, 22, 23, 24, 25]. Most of these studies were aimed at qualification of structural and functional materials to be used in a fusion power reactor. In fusion applications, such as liquid metal or molten salt blankets [26], high corrosion losses are expected because of the use of pure lithium, lithium containing alloys or molten salts as breeders/coolants, which are chemically aggressive to most of the steels and ceramics. High corrosion losses in a high-temperature blanket and deposition of corrosion products in a cold sections of the breeder circuit are considered to be among the most critical blanket feasibility issues [26]. The corrosion losses raise significantly with temperature and to a lesser degree with velocity. For example, the Sannier's equation for corrosion of ferritic steels in a turbulent $PbLi$ flow [27] suggests that the material mass loss depends on the $PbLi$ temperature T as $e^{-25690/1.98T}$ and on the velocity U_0 as ${U_0}^{0.875}$. To interpret correctly the corrosion data, it is important to have the flow and temperature field in the loop well characterized. With the modern computers and up-to-date numerical techniques, this goal can be achieved through computations as the experimental diagnostics is often limited and more expensive.

2.3 MHD flow in a manifold

A very important part of the fusion reaction facility blanket design is the liquid metal breeder supply and collection system, which includes inlet manifold for flow distribution, poloidal ducts for blanket functionality, and outlet manifold for flow gathering. A manifold is shaped such that the flow can be expanded or contracted from entrance to exit. The inlet manifold

located at the entrance of a blanket is responsible for distributing "cold" breeder from a feeding pipe into a breeding zone and cooling channels. The outlet manifold at the exit of the blanket collects "hot" breeder from multiple ducts inside the blanket into a single pipe through which the flowing liquid leaves the blanket towards the blanket ancillary system. A typical manifold system can be illustrated with the example of a Dual Coolant Lead Lithium (DCLL) blanket [28], where eutectic lead-lithium ($PbLi$) alloy is used for breeding tritium and cooling the breeding zone, while helium gas is used for cooling the First Wall (FW) and the internal blanket structure. In the DCLL inlet manifold, the $PbLi$ flows first in a smaller size radial duct or pipe, enters the expansion region of a larger size, and from there is distributed into several poloidal ducts in the breeding zone. The outlet manifold has a similar geometry but unlike the inlet manifold, the LM flow features a contraction. When flowing through the manifold in the presence of a strong plasma-confining magnetic field, the LM breeder experiences strong electromagnetic forces responsible for a significant 3D MHD pressure drop [29]. As shown in several studies (see e.g. [4]), the highest MHD pressure drop in the manifold is caused by a sudden change in the flow geometry (i.e. expansion or contraction) due to strong flow opposing forces associated with the formation of an internal MHD shear layer in the flowing liquid, often referred to as the Ludford layer [30]. Because of this, studies of MHD pressure drop in a manifold are often narrowed to the analysis of MHD flows in the expansion (inlet manifold) or contraction (outlet manifold) region. Due to its unique geometry, manifolds contribute to up to 50% of the total pressure drop of the entire blanket [31].

The basic problem of MHD flow in a rectangular or circular duct with insulating wall or conducting wall under uniform magnetic field has been addressed since middle of last century, with three different dimensionless parameters: Ha (Hartmann number) which is related to ratio of electromagnetic force and viscous force, Re (Reynolds number) describing the ratio of inertial force and viscous force, as well as N (interaction number) representing ratio of electromagnetic force and inertial force. Hartmann [32] and Shercliff [33, 34] first

derived the analytical solution for velocity distribution of MHD duct flow in a transverse magnetic field bounded by insulating wall perpendicular to the field, with relation for linear pressure drop. They discovered the MHD sublayer near the wall with the rest of flow (core) being highly uniform. The thin boundary layer was then called "Hartmann layer". After that, Chang et al. [35] obtained exact solutions for MHD duct flow in a perfectly conducting channel. Hunt [36] found solutions for two special cases with MHD flow bounded by both walls perpendicular and parallel to the magnetic field. The behavior of flow near the side wall which is parallel to the field is quite interesting. Hunt et al. [37] studied MHD flow in a rectangular duct with insulating Hartmann walls and perfectly conducting side walls using a boundary layer technique. They found the thickness of Hartmann layer near the wall perpendicular to the magnetic field to be scaled as $O\left(Ha^{-1}\right)$, while side layer near the wall parallel to the magnetic field to be scaled as $O\left(Ha^{-\frac{1}{2}}\right)$. Walker [38] used asymptotic expansions to study the fully developed MHD duct flow with a small conductance ratio. Ludford [39] identified a new type of internal layer along magnetic field lines when the flow is diverged by an obstacle at high Hartmann numbers. Hunt et al. [30] studied 2D version of the layer in a diverging wall over a body. Their conclusion was that the structure of the flow depends on the relative magnitude of Ha and N. The mathematical definition of the two dimensionless parameters will be given later.

In the 90s, with the rapid advancement of computer technology, numerical tools became available for simulation of MHD flow characteristics. Sterl [40] conducted a numerical study on rectangular duct MHD flow with varying wall conductivity. More recently, Zhou et al. [41] numerically examined the MHD flow in a circular pipe with self-developed code for high Ha tolerance.

MHD duct flow can be described using three parts: the highly uniform core flow, Hartmann layer and side layer. In the Hartmann layer, the flow exhibits larger velocity gradient and changes from uniform flow velocity to zero at the wall in a very short distance, which is the Hartmann layer thickness $O\left(Ha^{-1}\right)$. The side layer of insulating duct exhibits similar

behavior as Hartmann layer. While for the side layer of conducting duct, the flow will be accelerated dramatically in the cross section. The side layer is thicker than Hartmann layer and scale as $O\left(Ha^{-\frac{1}{2}}\right)$ in the rectangular duct and $O\left(Ha^{-\frac{2}{3}}\right) \sim O\left(Ha^{-\frac{1}{3}}\right)$ in the circular pipe.

The unique shape of MHD flow in a duct is closely related to induced electric current in the liquid metal, which will generate corresponding Lorentz force on the flow. The Lorentz force can be of several orders of magnitude higher than the inertial and viscous forces, and is the source of pressure drop. Wall conductivity can influence the pressure drop. For insulating duct, the entire current loop is inside the fluid domain. For conducting duct however, the current can exist in the wall and create a totally different distribution near the wall. Therefore, FCIs are used to help reduce the pressure drop.

Since nearly half of the total pressure drop occurs in the manifold, MHD flow in expansion and contraction ducts have been studied by many researchers. Bühler [42] derived solutions for inductionless inertialess MHD flow in a rectangular duct expanding in the direction parallel to the applied strong uniform magnetic field using core flow approximation. The core flow (inviscid) and boundary layers (viscous Hartmann layer and side layer) as well as the added "expansion layer" formed by the sudden expansion of the duct geometry were analyzed, for conducting and insulating duct. Detailed flow characteristics were explained using electric potential, current density and Lorentz force. Experimental study of similar duct was given by Horanyi et al. [43], with a Ha up to 5500, which is close to real blanket conditions. Mistrangelo [44] developed a numerical tool to study the MHD in duct flow, using case of a rectangular duct with perfectly conducting wall and expansion parallel to magnetic field as an example. By changing the magnetic flux intensity and the inertial force, effects on current distribution and pressure drop were shown. The importance of inertia forces is shown in [45] as well. Bühler et al. [46] also did experimental study under fusion-relevant numbers and revealed the 3D MHD pressure drop caused by 3D electric currents as well as examined flow structure predicted analytically in [47] at the expansion region.

Aitov et al. [48], Myasnikov et al. [49] and Kumamaru [50] numerically investigated the MHD flow in rectangular expansion duct with insulating walls, while Myasnikov et al. [49], Mistrangelo [44] and Kim [51] accomplished the same geometry cases with conducting walls. Kim [52] and Kumamaru [53] studied flow with same geometry but with sudden contraction.

Before 2018, poor-accuracy semi-empirical correlations were used to predict the ΔP_{3D} in manifold. Since the contribution of the pressure drop comes from many sources depending on the flow and applied magnetic field, a relation incorporating the inertial and electromagnetic effects is constructed with formula same as hydraulic pressure loss: $\Delta P_{3D} = k_p N \frac{\rho U^2}{2}$, where k_p is a coefficient strongly depending on flow geometry. Here N is the interaction number, while ρ and U are fluid density and velocity. This relation was applied in many manifold studies involving insulating/conducting walls [54], rectangular duct/circular pipe [55].

In 2018, Rhodes et al. [4] built the accurate correlations of ΔP_{3D} for the inlet manifold with sudden expansion taking into consideration the manifold geometry and inertial, viscous as well as electromagnetic force balance regimes. Recently, it is demonstrated that the same correlations can be applied to outlet manifold with sudden contraction [56]. These conclusions and numerical predictions from the earlier studies are in a good agreement with more recent MHD flow computations for a full DCLL blanket prototype [54, 57] for a strong $5T$ magnetic field. The research regarding gradual expansion/contraction manifold MHD flow is still rare, and the effect of expansion length on pressure drop is still unknown. No correlations on pressure drop of this type of manifold has been established.

2.4 MHD flow in a fringing magnetic field

A fringing magnetic field is a peripheral area of magnetic field outside the magnet core. In the core, the magnetic field can be assumed as uniform and parallel, while decaying of the field occurs near the edges, thus forming the fringing magnetic field. As a special case of MHD flow effect, the 3D MHD pressure drop brought by the spatially varying magnetic field

can play an important role in designing fusion reactor blankets. With a fringing magnetic field described by hyperbolic function, the electrically conducting liquid metal flow will experience an increase in magnitude of magnetic field at the entry and a decrease at the exit. This simulates the effects of a more realistic nonuniform conservative magnetic field on inlet and outlet pipes connected to manifold, which is non-negligible. The flow profile is fully developed hydrodynamic when entering the magnetic field region, where it changes to "M shape" due to 3D electric current induced by magnetic field interaction with flow. When exiting the fringing magnetic field, the flow will slowly return to hydrodynamic with possible transition from laminar to turbulent state due to lack of Lorentz force to suppress the instability. Analytical approach to calculating the pressure drop using integration method for such flow was proposed by Miyazaki et al. [6]. Reed et al. [5] carried out experiments on flow in an electrically conducting rectangular duct. The numerical simulations of 3D fringing magnetic field MHD flow generally adopt two types of descriptions for the magnetic field. The first is a reduced axial direction-dependent only field with decay (non-conservative/inconsistent), while the second is a curl/divergence free full field with all three spatial components (conservative/consistent). Reed et al. [5], Votyakov et al. [58], Moreau et al. [59] and Zhou et al. [60] numerically studied the flow with reduced field in a rectangular duct, with conducting and/or insulating walls. Reed et al. [5], Chico et al. [61], Li et al. [62] and Pulugundla et al. [63] performed similar studies on circular pipes. In Moreau et al. [59, 64] and Chico et al. [61], the differences in results calculated by using simplified versus full magnetic field for rectangular duct were analyzed, which were included in Li et al. [62], Li et al. [65], Pulugundla et al. [63] as well. The studies reveal that difference in pressure and velocity distribution for two types of magnetic fields mainly exists in downstream area, and is more obvious for electrically conducting pipe than for insulating one. The improvement of using full consistent magnetic field on results is limited, with computational cost increased. From an engineering aspect, it is generally acceptable to use a reduced filed to simulate the MHD flow in a fringing magnetic field. Chico et al. [61] compared the results of MHD flow with reduced and full magnetic

field in circular pipes. These studies show that using reduced magnetic field assumption can accurately predict the flow characteristics before the inflection point of the field, where the gradient of the field is steepest. After that, due to 3D axial current effects, the results may not be precise enough compared with full field experimental data. Moreover, the flow in a fringing magnetic field exhibits great resemblance as that in a uniform field, making prediction of pressure drop utilizing correlations for the fully developed flow possible. However, real fusion reactors have much steeper magnetic field gradient and the extent to which the pressure drop relation can apply still remains to be determined.

CHAPTER 3

Main goals of study

The main goals of the current study include:

1. Characterization study of a *PbLi* flow driven by buoyancy forces in a TCL, including analysis for the bulk circulation velocity, maximum and minimum temperatures, distribution of velocity and temperature in the loop, corner flow patterns and the influence of inserted specimens and their shape and size on the flow and heat transfer. The most important goal is to elucidate the effect of the applied heat flux on the bulk flow velocity and minimum and maximum temperatures in the loop. This is needed to further characterize the effect of the flow in the thermal convection loop on the corrosion of immersed samples as the corrosion rate is known to be strongly dependent on the fluid velocity and especially its temperature. This will eventually help to explain various corrosion data acquired by experiments, which are often contradicting.

2. Optimization of the manifold design where the liquid from the small-size duct enters the large-size duct through a gradual transition section (inlet manifold) or vice versa from a large to a small duct (outlet manifold). In such flows, high 3D MHD pressure drop is caused due to axial currents generated in the expansion or contraction region. The main goal of this study is to perform parametric numerical studies for the inlet and outlet manifold flows and then use the obtained data for the 3D MHD pressure drop to deduce pressure drop correlations. The expectation is that the manifold design with gradual expansion (or contraction) will demonstrate significantly lower MHD pressure drop compared to the design with a sudden change of the duct geometry.

3. Characterization studies of MHD flows and 3D MHD pressure drop in a duct or pipe flow of liquid metal in a fringing magnetic field. These studies will include parametric 3D MHD computations for a broad range of Hartmann and Reynolds numbers. The obtained results will be used to deduce correlations for the MHD pressure drop caused by sudden changes in the applied magnetic field. A part of this study is investigation of the influence of the applied magnetic field distribution and intensity in the fringing field region on the flow. The most important goal here is to look at the flow physics related to 3D effects and provide better prediction of the related MHD pressure drop.

CHAPTER 4

Problem formulation

4.1 Governing equations

In real blanket, the geometry is complex with applied magnetic field and neutron volumetric heating. Therefore, the buoyancy-driven flow and MHD effect are present simultaneously in momentum equation, and coupled with energy equation. The electric currents are described by Ohm's law and charge conservation. To formulate the real problem, two approximations are adopted. The first one is inductionless approximation, which states that for the magnetic field composed of applied and induced terms $\mathbf{B}_{total} = \mathbf{B} + \mathbf{B}_i$, the second term can be neglected if magnetic Reynolds number R_m is much smaller than unity, $R_m \ll 1$. The magnetic Reynolds number is a dimensionless number characterizing the relative strength of induction of a magnetic field by fluid motion over magnetic diffusion. The second assumption is the Boussinesq approximation, where the fluid density is treated as a constant except in the buoyancy force term, for which a linearized function of fluid density with respect to temperature is used.

Finally, using all these approximations, the MHD flow with volumetric heating can be described by the Eqs. 4.1∼4.5, which corresponds to the problem shown in Figure. 4.1:

$$\frac{\partial \rho}{\partial t} + \nabla \cdot (\rho \mathbf{v}) = \frac{D\rho}{Dt} + \rho \left(\nabla \cdot \mathbf{v}\right) = 0 \tag{4.1}$$

$$\frac{\partial \mathbf{v}}{\partial t} + \mathbf{v} \cdot \nabla \mathbf{v} = -\frac{1}{\rho}\nabla P + \nu \nabla^2 \mathbf{v} + \mathbf{g} - \beta \mathbf{g}(T - T_0) + \frac{1}{\rho}\mathbf{J} \times \mathbf{B} \tag{4.2}$$

$$\rho C_p \left(\frac{\partial T}{\partial t} + \left(\mathbf{v} \cdot \nabla\right) T\right) = k \nabla^2 T + q''' \tag{4.3}$$

$$\mathbf{J} = \sigma\left(-\nabla\phi + \mathbf{v} \times \mathbf{B}\right) \tag{4.4}$$

$$\nabla \cdot (\sigma \nabla \phi) = \nabla \cdot (\sigma \mathbf{v} \times \mathbf{B}) \tag{4.5}$$

In the above equations, ρ is the fluid density, $\mathbf{v}$ is the velocity vector, ν is kinematic viscosity, P is the pressure, $\mathbf{g}$ is the gravity vector, β is thermal expansion coefficient, T and T_0 are temperature field and reference temperature, $\mathbf{J}$ is the electric current vector, $\mathbf{B}$ is the magnetic flux density vector, C_p is specific heat capacity, k is thermal conductivity, σ is electrical conductivity, q''' is volumetric heating value, and ϕ is electric scalar potential.

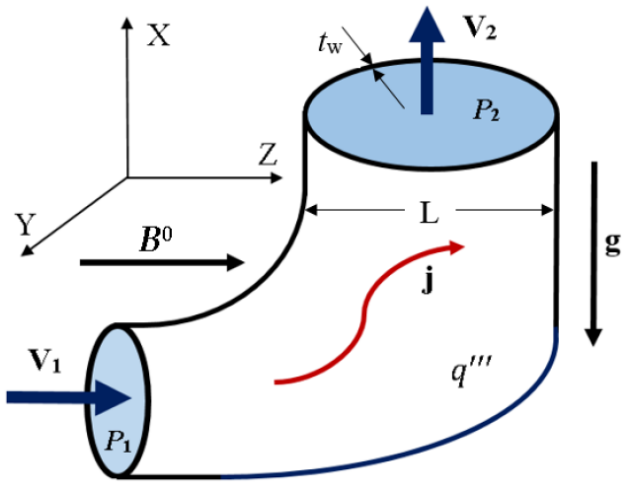

Figure 4.1: Sketch of a pressure driven LM flow in a complex geometry thin-walled duct with applied magnetic field and volumetric heating in the presence of gravity forces.

Specifically, the three dimensional form of the Lorentz force term in Navier-Stokes equations and the induced current term in electric current density can be written as: $\mathbf{J} \times \mathbf{B} = (J_y B_z - J_z B_y)\hat{i} + (J_z B_x - J_x B_z)\hat{j} + (J_x B_y - J_y B_x)\hat{k}$, $\mathbf{v} \times \mathbf{B} = (vB_z - wB_y)\hat{i} + (wB_x - uB_z)\hat{j} + (uB_y - vB_x)\hat{k}$, where $\hat{i}, \hat{j}, \hat{k}$ are the orthogonal unit vectors in Cartesian coordinates.

According to the physical nature of the problems, the governing equations can be simplified and solved with the application of various boundary conditions. Two models are established using part of the equations.

4.1.1 Governing equations for hydrodynamic flows with buoyancy effects

The first model involves hydrodynamic flow in a TCL with buoyancy forces caused by surface heating and cooling. In all cases, the flow is incompressible, so that the continuity Eq. 4.1 can be simplified as:

$$(\nabla \cdot \mathbf{v}) = 0 \tag{4.6}$$

The momentum of the flow is described by omitting the Lorentz force term and preserving buoyancy force in Eq. 4.2:

$$\frac{\partial \mathbf{v}}{\partial t} + \mathbf{v} \cdot \nabla \mathbf{v} = -\frac{1}{\rho} \left(\nabla \left(p - \rho \mathbf{g} z \right) \right) - \beta \mathbf{g} \left(T - T_0 \right) + \nu \nabla^2 \mathbf{v} \tag{4.7}$$

The energy equation can be simplified to the form without volumetric heating:

$$\rho C_p \left(\frac{\partial T}{\partial t} + \left(\mathbf{v} \cdot \nabla \right) T \right) = k \nabla^2 T \tag{4.8}$$

4.1.2 Governing equations for MHD flows

The second model is used to characterize the MHD flow in a duct or pipe.

Similarly, the continuity equation can be written as Eq. 4.6.

The momentum equations can be written by omitting the buoyancy force and gravity term in Eq. 4.2 as:

$$\frac{\partial \mathbf{v}}{\partial t} + \mathbf{v} \cdot \nabla \mathbf{v} = -\frac{1}{\rho} \nabla p + \nu \nabla^2 \mathbf{v} + \frac{1}{\rho} \mathbf{J} \times \mathbf{B} \tag{4.9}$$

Eq. 4.4 and Eq. 4.5 needs to be used for solving electric currents in the MHD flow.

4.2 Dimensionless parameters

The governing equations for MHD flow can be non-dimensionalized using characteristic quantities: the bulk velocity $\bar{U}$ as scale for velocity, B_0 for magnetic field, L for length, ΔT for temperature. Other scales can be expressed by these basic ones: $\frac{L}{\bar{U}}$ for time, $\bar{U} B^2 L \sigma$ for

pressure, $\bar{U}BL$ for electric potential and $\bar{U}B\sigma$ for electric current density. Therefore, the dimensionless equations can be written in Eqs. 4.10∼4.14:

$$\nabla \cdot \tilde{\mathbf{v}} = 0 \tag{4.10}$$

$$\frac{\partial \tilde{\mathbf{v}}}{\partial \tilde{t}} + \tilde{\mathbf{v}} \cdot \nabla \tilde{\mathbf{v}} = -\nabla \tilde{p} + \frac{1}{Fr^2}\frac{\mathbf{g}}{g} + \frac{1}{Re}\nabla^2 \tilde{\mathbf{v}} + N \cdot \tilde{\mathbf{J}} \times \tilde{\mathbf{B}} \tag{4.11}$$

$$\frac{\partial \tilde{T}}{\partial \tilde{t}} + (\tilde{\mathbf{v}} \cdot \nabla)\, \tilde{T} = \frac{1}{Re \cdot Pr}\tilde{k}\nabla^2 \tilde{T} + \tilde{q}''' \tag{4.12}$$

$$\tilde{\mathbf{J}} = -\nabla \tilde{\phi} + \tilde{\mathbf{v}} \times \tilde{\mathbf{B}} \tag{4.13}$$

$$\nabla \cdot \left(\sigma \nabla \tilde{\phi}\right) = \nabla \cdot \left(\sigma \tilde{\mathbf{v}} \times \tilde{\mathbf{B}}\right) \tag{4.14}$$

The dimensionless numbers include Re, Gr, Ha, Fr and N. The dynamic viscosity is represented by μ and gravity scalar value by g. The Reynolds number is defined by: $Re = \frac{\rho \bar{U} L}{\mu} = \frac{\bar{U} L}{\nu}$, which characterizes the ratio of inertial force to viscous force. The Grashof number $Gr = \frac{g\beta L^3 \Delta T}{\nu^2}$ is the ratio between buoyancy force and viscous force. The Hartmann number $Ha = B_0 L\sqrt{\frac{\sigma}{\mu}}$ represents the square root of electromagnetic force over viscous force. While the interaction number, related to Re and Ha by $N = \frac{Ha^2}{Re} = \frac{\sigma {B_0}^2 L}{\rho \bar{U}}$, states the ratio between electromagnetic force and inertial force. The Froude number $Fr = \frac{\bar{U}}{\sqrt{gL}}$ is the ratio of inertial force to gravity. The Prandtl number, $Pr = \frac{C_p \mu}{k} = \frac{\rho C_p \nu}{k}$, is the ratio of momentum diffusivity to thermal diffusivity. The aforementioned wall conductance ratio for problems with conducting duct or pipe is defined by $c_w = \frac{\sigma_w t_w}{\sigma_f L}$, giving the relative conductance of wall compared to fluid, where σ_w is the duct wall electrical conductivity, t_w is the wall thickness, σ_f is the fluid electrical conductivity.

4.3 Boundary conditions

In order to make the solution of mathematical models unique, various boundary conditions need to be added. There are three classes of boundary conditions for physics appearing in the problem of MHD flow: fluid flow, electric current with magnetic field, and heat transfer.

For fluid flow domain, the no-slip and no flow through condition are always satisfied. Basically, the fluid with viscosity should stick to the wall at fluid/wall interface, whether it is static or moving. To write in equation form we have: $\mathbf{v}_t|_{wall} = v_{wall}$, $\mathbf{v}_n|_{wall} = 0$, which means the tangential component of fluid velocity at the wall equals to the wall velocity, and the normal component of fluid velocity vanishes at the physical boundary. The inlet and outlet conditions can be classified as combinations of velocity and pressure. Fully developed velocity and electric current condition can be used with constant temperature and no pressure gradient for the inlet if variations of flow characteristics along axial direction are negligible for MHD flow. The outlet features a "continuative" boundary representing zero derivatives for all quantities except pressure. The pressure is often set to be zero at the outlet.

While for electric currents in fluid and solid wall, the electric contact is perfect if no contact resistance exists between the fluid/solid interface. The component of electric current normal to the wall and electric potential are continuous under this circumstance. However, the tangential component of electric current, due to different conductivities of fluid and solid wall, will experience a sudden change. The thin wall boundary condition can be applied when the wall thickness is negligible compared to the characteristic length of the duct, which implies that the electric current, though exists in the wall, flows only in tangential direction with the normal variation neglected. On the contrary, the thick wall boundary implies no penetration of current at the outside wall of the duct which corresponds to zero normal component of electric current, similar to the no flow through condition. As a whole, the flow duct is electrically insulated on all boundaries to form a closed area for electric currents to circulate. If the electrically conducting wall has a different electrical conductivity compared to the liquid metal inside, the insulation should be applied to the outer boundaries of the wall.

For thermodynamic processes occurring in fluid and solid domain such as conduction, convection and radiation, three types of boundary conditions can be imposed. The first type is called "Dirichlet" boundary condition, which gives the temperature value at the boundary.

This is almost always a simplified assumption which can be expressed by $T_{wall} = T_0(x, y, z, t)$. The second type is Neumann boundary condition, with normal heat flux specified. This is related to the temperature gradient at the boundary and can be written as: $-\mathbf{n} \cdot (-k\nabla T) = q_0(x, y, z, t)$. If $q_0 = 0$, it implies thermal insulation. The last type is in the form of Robin boundary condition, or physically Newton's law of cooling, which is a mixed one depending on both T and ∇T. The mathematical form is $-\mathbf{n} \cdot (-k\nabla T) = h(T_{ext} - T)$, in which the heat transfer coefficient h and external temperature T_{ext} are the key controlling parameters. Typically, T_{ext} is fixed by the problem and h can be calculated by empirical relations. For natural convection, gas has a heat transfer coefficient of $h = 2 \sim 25 W/(m^2 \cdot K)$ and liquid of $h = 50 \sim 100 W/(m^2 \cdot K)$. For forced convection, the heat transfer coefficient is significantly higher, with gas of $25 \sim 250 W/(m^2 \cdot K)$ and liquid of $100 \sim 20,000 W/(m^2 \cdot K)$. Besides the three forms of boundary conditions, radiation which occurs when large temperature difference exists needs to be considered, and the rate of radiation per square meter area can be expressed by $q = \epsilon\sigma (T_h^4 - T_c^4)$ if an hot object is radiating energy to its cooler surroundings.

CHAPTER 5

Characterization of $PbLi$ flows in thermal convection loop (TCL)

In this study, the main goal is the development of computational tools and characterization of fluid flow and temperature fields in a TCL under specific conditions of the corrosion experiments. The analysis is limited to a particular experimental facility and operation conditions employed at the Oak Ridge National Lab (ORNL), USA. This type of facility has been used in experimental studies of corrosion behavior of fusion materials for decades. The Corrosion Science & Technology Group at ORNL has a long experience of using TCLs for materials qualification. In one of the first experimental campaigns dated back to 1982 [25], three TCLs were constructed to perform experiments on corrosion of $Fe-Ni-Cr$ alloys in the flowing molten salt $NaNO_3-KNO_3$ at temperatures around $600°C$. Natural circulation of the salt was induced in these closed loops through controlling the temperature profile by heating one of the two $\sim 0.8m$ vertical sections and cooling the other. The loops were designed to allow the insertion and removal of corrosion coupons with minimal disruption of the salt flow. The corrosion coupons of approximately $0.019 \times 0.008 \times 0.001m$ were placed within the "hot" and "cold" legs. Tubing for the loops ranged from 0.019 to $0.025m$ in outside diameter (OD) and from 0.002 to $0.003m$ in wall thickness. The nominal salt velocity U_0 was $0.04m/s$ and the temperature difference between the hottest and coldest liquid in the loop, $\Delta T = T_{max} - T_{min}$, was from 150 to $250K$ depending on the loop. Such TCL designs were adopted in several subsequent experimental campaigns at ORNL, varying in materials and heat loads. In the most recent studies [1, 2], several similar corrosion loops

were constructed to explore the upper temperature limit of a breeding fusion blanket utilizing eutectic $Pb-17$at.$\%Li$ alloy as a coolant and breeder.

In [2], three mono-metallic thermal convection loops were fabricated from alloy APMT ($Fe-21Cr-5Al-3Mo$) and operated with commercial $PbLi$ at peak temperatures of 550°C, 600°C and 650°C, and ΔT of $85 \sim 115K$. The outside diameter of the TCL tubes was nominally $0.0267m$ with a wall thickness of $0.0031m$. The vertically oriented sections of the TCL were approximately $0.5m$ apart, and the not quite horizontal sections (about 1:4 slope) were about $0.75m$ apart as shown in Figure 5.1. Heating was provided using clamshell heaters placed around the bottom, near-horizontal section and one of the two vertical sections ("hot leg"). The heated portions of the loop were heavily insulated while other unheated portions ("cold leg") were only lightly insulated.

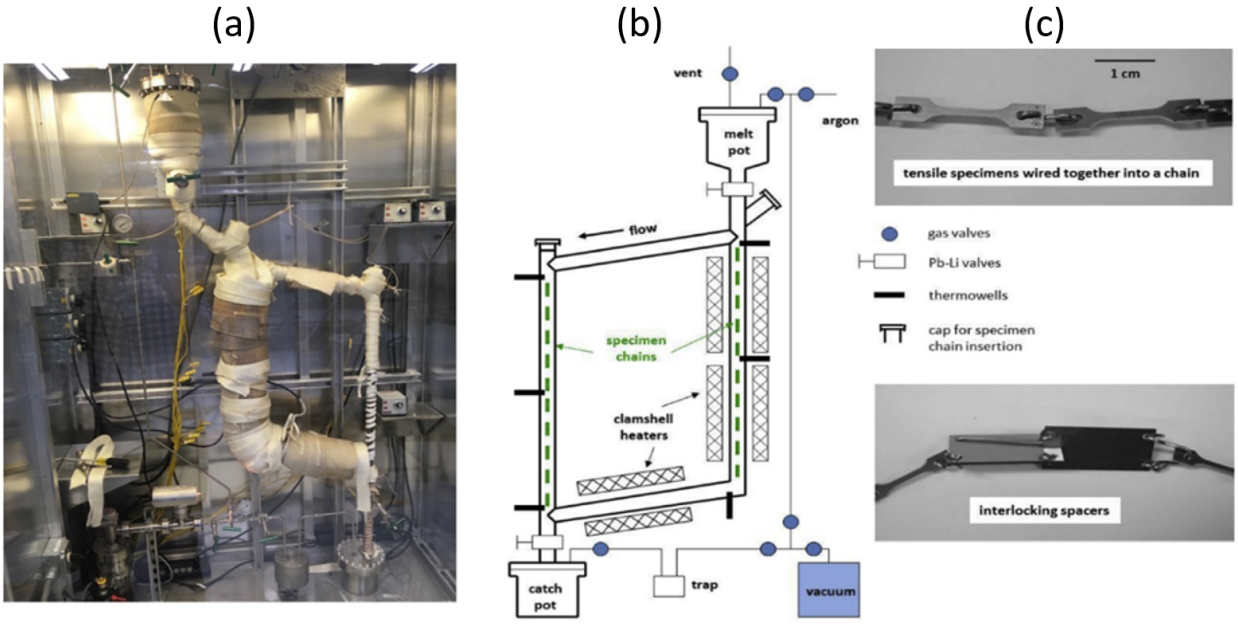

Figure 5.1: ORNL $PbLi$ thermal convection loop: (a) picture, (b) schematics and (c) "dog-bone" samples and spacers [1, 2] immersed in the liquid.

Two chains of APMT "dogbone" $0.0254m$ long specimens including six spacers were hung in the hot and cold legs of the loop to evaluate corrosion losses after $1000h$ exposures in each

experiment. Most APMT specimens were pre-oxidized to form alumina prior to exposure and exhibited small mass losses. Specimens without pre-oxidation exhibited higher mass losses. While promising for increased blanket temperatures, the small mass losses suggest that the surface oxide is not completely stable. However, even at the highest temperature, there was no indication of classic dissolution/precipitation behavior, suggesting that higher temperature compatibility may be possible. Based on the temperature data in [1, 2], in these experimental studies, the Grashof number defined here as $Gr = \frac{g\beta\Delta T d^3}{\nu^2}$ (g is the acceleration due to gravity, ν is the kinematic viscosity, $d = 2R$ is the inner pipe diameter, and β is the thermal expansion coefficient of $PbLi$) varied in the range $(2.0 \sim 3.0) \times 10^7$. The Prandtl number $Pr = \frac{\nu}{\alpha}$ was 0.015. The estimated nominal velocity in the experiment was around $0.07 m/s$, suggesting the hydrodynamic Reynolds number around 10,000.

The Re and Gr magnitudes in the experiments suggest that the $PbLi$ flows were turbulent. In addition, taking into account the presence of sharp corners and corrosion specimens hanging in the $PbLi$, unsteady flow features can be expected. Such flow conditions were reproduced in computations in the present study using two modeling tools. The first one is a user-defined model for a buoyancy-driven flow in the TCL implemented in COMSOL Multiphysics [66]. The second is a newly developed thermohydraulics code. Both the computational model in COMSOL and the thermohydraulics code were developed to cover laminar and turbulent flow regimes for Re numbers below and above the turbulence threshold. The thermohydraulics code also has an option for adding an applied transverse magnetic field to simulate special experiments where a permanent magnet is used to reproduce conditions of a MHD flow, similar to that in a liquid metal blanket.

5.1 Mathematical formulation of the problem

The flow in TCL uses the first model mentioned in Section 4.1, therefore Eqs. 4.6∼4.8 are solved for this problem. The corresponding boundary conditions need to be applied.

For the reason that the TCL is a closed loop, there is no inlet/outlet condition for the flow. The pipe wall has no slip boundary condition at the fluid-solid interface. The temperature boundary condition can be formulated separately for hot and cold legs. For the hot leg, the constant heat flux boundary is a Neumann boundary condition, which can be expressed by:

$$-k\frac{\partial T}{\partial r} = q'' \text{ at } r = R \tag{5.1}$$

For the cold leg, it has convective or Robin type boundary condition written as:

$$-k\frac{\partial T}{\partial r} = h(T - T_{air}) \text{ at } r = R \tag{5.2}$$

in which h is the heat transfer coefficient that characterizes the rate of heat loss from the cold leg into the surrounding air of the temperature T_{air}. In this problem, the convection and radiation heat transfer are both present and cannot be negligible against each other, such that a total heat transfer coefficient is estimated $h = h_c + h_r$. Unlike h_c which depends solely on material and natural/forced convection, the radiation-based h_r strongly depends on temperature. A linearized equation is often used in general engineering practice $h_r = \epsilon\sigma(T + T_{air})(T^2 + T_{air}^2)$, where ϵ is the thermal emissivity of the surface and $\sigma = 5.67 \times 10^{-8} W/(m^2 \cdot K^4)$ is the Stefan-Boltzman constant. Under the conditions of experimental studies [1, 2], the coefficients are estimated as $h_c = 5 \sim 10 W/(m^2 \cdot K)$ and $h_r = 30 \sim 60 W/(m^2 \cdot K)$, which shows that in a high temperature convection loop, the radiation effect is very important to consider. In this study, for simplicity, the applied heat flux q'' for hot leg and heat transfer coefficient h for cold leg are assumed constant and uniform. When steady state is achieved, the heat flux should balance with heat loss.

5.2 Validation case for the numerical tool

Before going to full three-dimensional analysis of model similar to the experiment, computational tool-COMSOL Multiphysics 5.4 was tested for ability to successfully predict simpler case results. Mixed convection flow in a vertical pipe was picked and this case can be solved

analytically, as illustrated in Figure 5.2. A verified code was already established to examine the accuracy of COMSOL predicting the results. The verification code solves the following set of non-dimensionalized equations:

$$\begin{cases} \frac{1}{\tilde{r}}\frac{d}{d\tilde{r}}\left(\tilde{r}\frac{d\tilde{\theta}}{d\tilde{r}}\right) = 2\tilde{u}_z\left(r\right) \\ 0 = -\frac{d\tilde{p}^*}{d\tilde{z}} + \frac{1}{Re}\frac{1}{\tilde{r}}\frac{d}{d\tilde{r}}\left(\tilde{r}\frac{d\tilde{u}_z}{dr}\right) + \frac{Gr}{Re^2}\tilde{\theta}\left(r\right) \end{cases} \tag{5.3}$$

with boundary conditions and constraints:

$$\begin{cases} \int_0^1 2\tilde{r}\tilde{u}_z d\tilde{r} = 1 \\ \int_0^1 2\tilde{r}\tilde{u}_z\tilde{\theta} d\tilde{r} = 1 \end{cases} \tag{5.4}$$

Comparison of results from COMSOL and code [3] for velocity distribution at fully-developed region is shown in Figure 5.3. Clear observation of good match between both results can prove that COMSOL is a robust tool in solving mixed convection problems when applying different heat flux values.

5.3 Computational setup in COMSOL

The computational setup of the problem depends on flow characterizing parameters. Unlike the majority of natural convection flows where the liquid flows upwards near the hot wall and downwards near the cold wall, such that the mean velocity is zero due to the mass conservation, the flow in the TCL is of a circulation type [17, 67]. For this reason, a standard Reynolds number similar to that in forced convection flows can be constructed using the circulation velocity as introduced in section 1 to distinguish between laminar and turbulent flows. In the experimental studies in [18], transition to turbulence was studied in a TCL facility, which was very similar to that in the present study. The flow was found to be laminar if $Re < 900$. For $900 < Re < 3200$, the TCL flow is transitional from laminar to turbulent. It becomes fully turbulent if $Re > 3200$. Based on these data, in the present

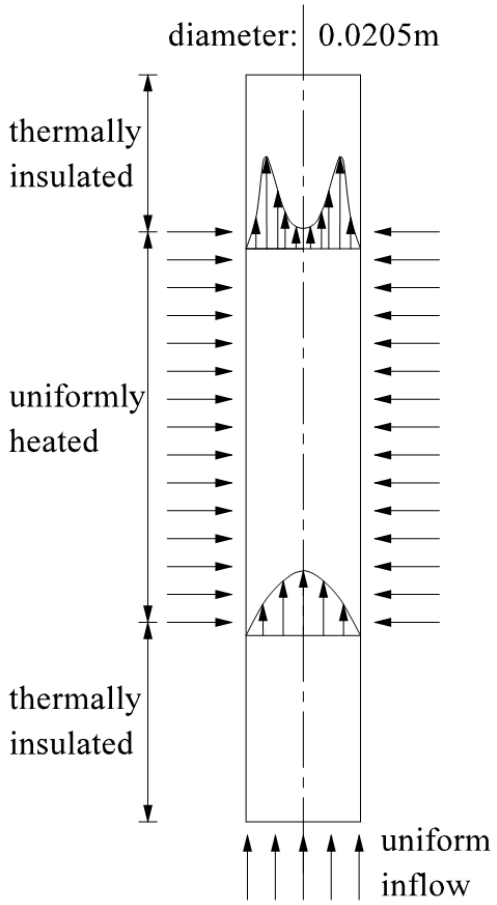

Figure 5.2: Schematic illustration of fluid flow in vertical heated pipe for validation.

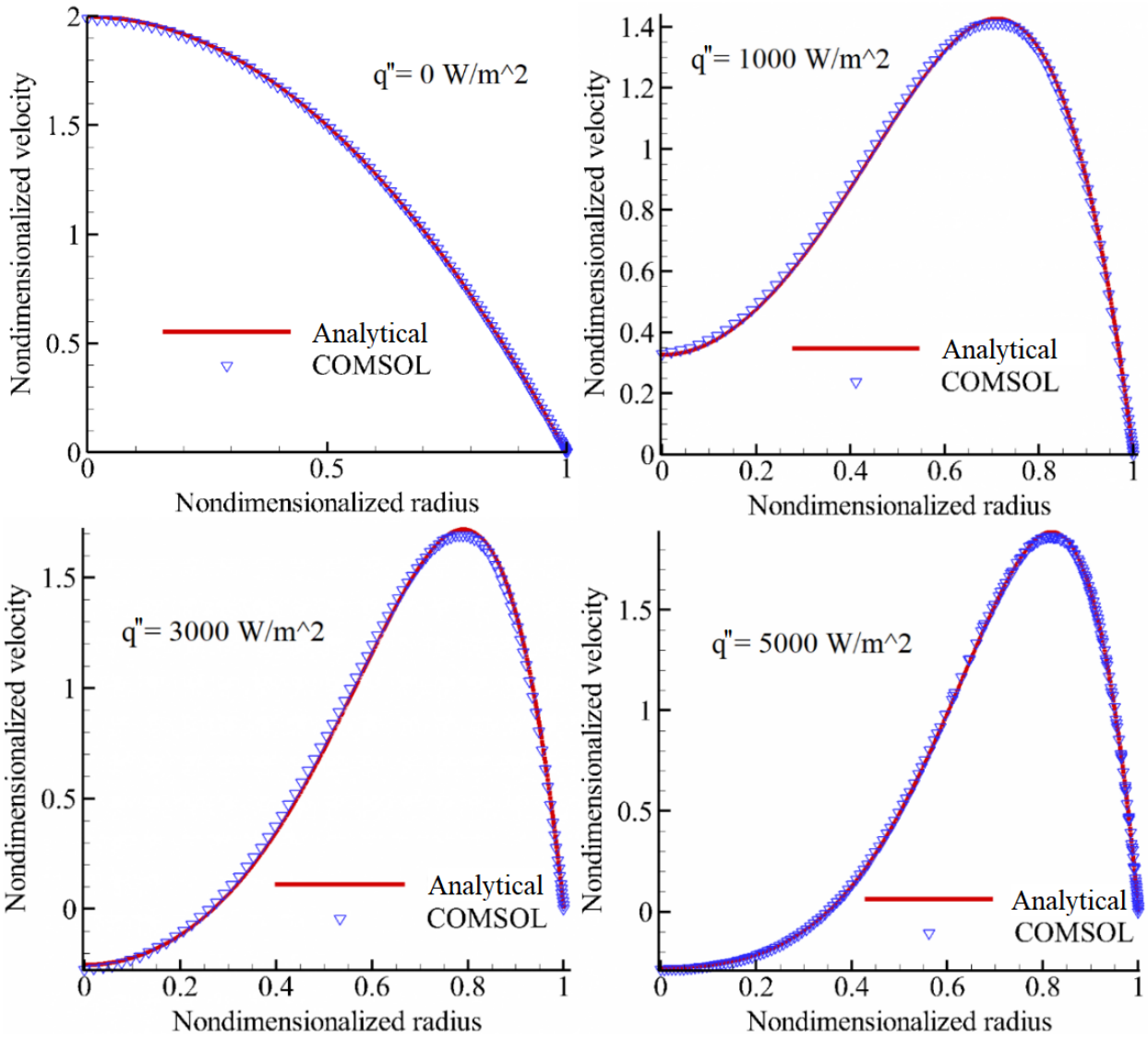

Figure 5.3: Comparison of results given by computational code [3] and COMSOL.

study $Re_{cr} = 3200$ was used as the Reynolds number threshold. Most of the analysis in this study was performed for flow velocities $U_0 > 0.05m/s$ ($Re > 7200$) using a turbulent flow solver. Several turbulence models are offered in COMSOL [66]. In this study, the classical $k - \epsilon$ model was chosen [68]. The model introduces two additional transport equations and two dependent variables: the turbulent kinetic energy k, and the turbulent dissipation rate, ϵ. The turbulent viscosity added into momentum equation is modeled by two variables as: $\mu_T = \rho C_\mu \frac{k^2}{\epsilon}$, where C_μ is a model constant [68]. Standard wall-functions were used as boundary conditions to simulate turbulence properties in the near-wall region.

In COMSOL, a finite-element stationary solver or a time dependent solver can be selected in various forms to determine the coupling and sequence of calculations. In this study, both the stationary solver and time dependent solver were employed as it is not a priori known if the flow is stationary or transient.

In stationary computations, fluid flow, heat transfer, and non-isothermal flow physics are solved at the same time. The computations are based on the segregated approach using the algebraic multigrid solver embedded in the software with a convergence criterion of 10^{-3} as a default. Convergence criteria of 10^{-4} to 10^{-6} were also implemented to compare with the default case. The segregated approach has a maximum iteration number of 400, and pseudo time stepping for stabilization and acceleration with initial CFL number of 3. The multigrid solver uses maximum number of iterations of 500 and residual tolerance of 0.01.

For time dependent computations, a more robust "fully coupled" solver with the residual tolerance of 10^{-6} was used to reproduce the transient flow behavior. The solver uses an automatic Newton-Raphson method for better convergence with maximum iteration number of 50. The backward differentiation formula (BDF) is used for time stepping. A small initial time step of $0.001s$ was set to ensure a more accurate prediction of the flow at the beginning. The time step is gradually increased in the course of the computations as the results become steadier by choosing "free" time stepping in COMSOL settings. Both stationary and time dependent solvers use the same spatial mesh of tetrahedral second order elements and first-

order shape functions.

A mesh sensitivity study was performed first. Three types of meshes were tested for the case with no samples as shown in Figure 5.4, including coarse, normal and fine meshes. As there is almost no difference in the results between the normal and fine meshes (see Table 5.1), the normal mesh was considered sufficient, such that the most of the computations in this study were conducted on the normal mesh. It should be noted that the cases with the immersed samples require very fine meshes to resolve the temperature field inside the samples, pipe walls and fluid. The number of mesh elements in such cases is enormous (75,935,516) resulting in very time-consuming computations of full 7 days using a 32-core workstation with 512 Gb RAM.

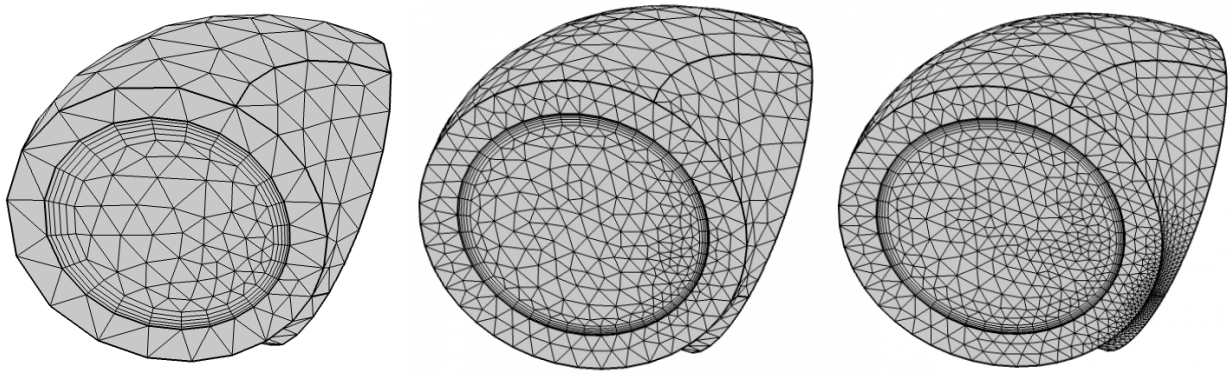

Figure 5.4: Tetrahedral meshes with different density used in COMSOL computations: (left) coarse, (middle) normal and (right) fine.

In addition to the mesh sensitivity study, other testing effort included comparison between the results obtained with the stationary and time dependent solver. When using the time dependent solver, the computations were started from the zero velocity and $T = T_0$ and continued over a long period of time corresponding to several full fluid circulations in the loop. To assure convergence, the applied heat flux was varied exponentially in time over about 20 seconds from zero to the maximum value. As shown in Figure 5.5, the time dependent flow evolves eventually to a steady state. In a few cases, at the highest Re numbers, the flow

Table 5.1: Summary of computed results for three meshes, coarse, normal and fine for $q'' = 20kW/m^2$ and $h = 45W/(m^2 \cdot K)$.

Mesh quality	Number of elements	Computational time, s	Average velocity, m/s	Average temperature, $°C$
Coarse	353829	4541	0.070439	457.99
Normal	800656	10928	0.070453	458.22
Fine	1871981	18847	0.070457	458.26

was observed to exhibit slightly unsteady periodic behavior with the period of about $40s$. However, even in these cases, the difference with the predictions obtained with the stationary solver did not exceed a few percent such that most of the computational results shown below were obtained with the stationary solver assuming that the steady state solution exists.

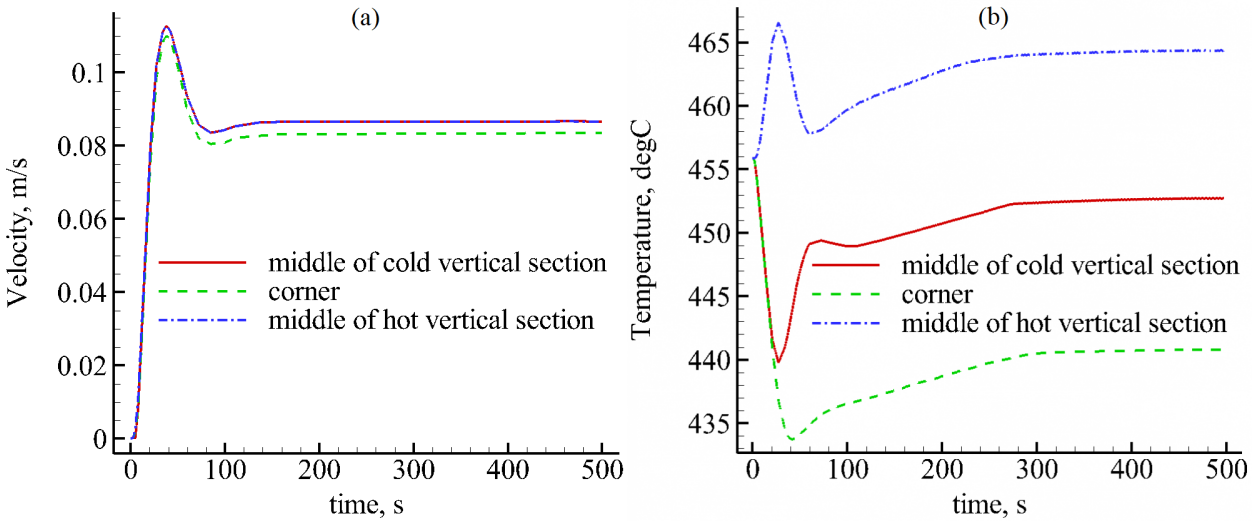

Figure 5.5: Time history computed with the time dependent solver at $q'' = 20kW/m^2$ and $h = 45W/(m^2 \cdot K)$: (a) velocity, and (b) temperature.

5.4 Results and discussion of 3D computations using COMSOL

5.4.1 Reference case

To characterize the velocity distribution and temperature field in the TCL, a reference case was selected first, which is the thermal convection loop without samples (Figure 5.6), with the applied heat flux q'' in the hot leg of $20kW/m^2$ and the heat transfer coefficient h in the cold leg of $45W/(m^2 \cdot K)$. The heat transfer coefficient includes both convective and radiative components such that about 15% of heat in the cold leg is removed by air through convection and the rest is by radiation. In addition to the loop schematics, Figure 5.6 shows 2D cross-sectional velocity and temperature isolines in the middle of the vertical part of the hot leg. More details of the flow and temperature field in the reference case are shown in Figure 5.7∼5.9. Figure 5.7 shows velocity profiles at several positions along the vertical sections of the hot and cold legs. Interestingly, the velocity distributions of the hot and the cold leg are anti-symmetric. For example, both the hot leg and the cold leg velocity profile right downstream of the corner have the same shape with a velocity peak near the outer pipe wall and a plateau-like distribution near the inner wall. Further downstream, the velocity profiles become more uniform. Eventually, almost fully developed flow in both legs is achieved at a relatively short distance of about $0.2m$ downstream from the corner. The flow remains fully developed over the major part of each vertical section of about $0.5m$ as seen in Figure 5.8.

When approaching the corner, the velocity profile in the vertical section of the loop becomes non-uniform again. The most significant changes in the flow field occur in the corners themselves, where the flow demonstrates two large stationary vortices as shown in Figure 5.8. Such large vortices are known in the hydrodynamics of pipe flows as Dean vortices [69]. Their formation is caused by centripetal forces when a fluid is moving along a straight pipe that after some point becomes curved, e.g. in a bend. As a result, the generated secondary motion is superimposed on the primary flow with the fluid in the center of the

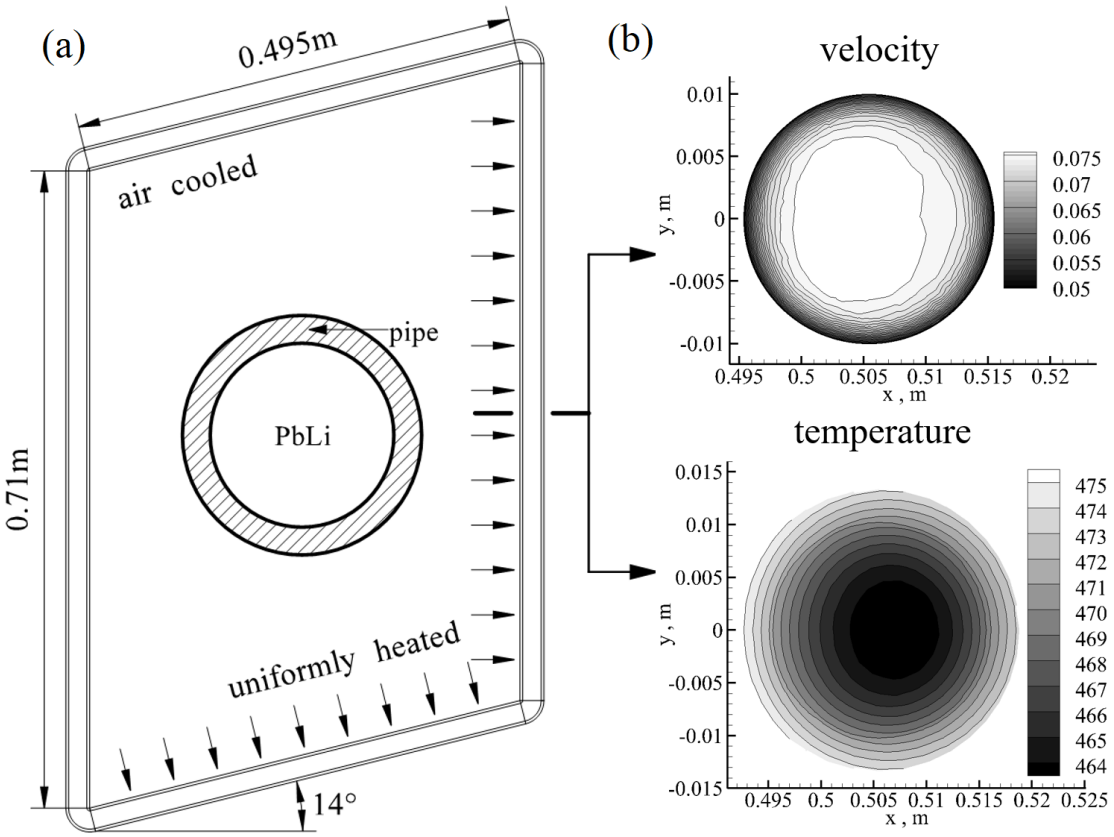

Figure 5.6: Reference case: TCL loop without samples, $q'' = 20kW/m^2$, $h = 45W/(m^2 \cdot K)$. (a) TCL schematics. (b) Velocity (top) and temperature (bottom) distributions in the middle of the vertical part of hot leg.

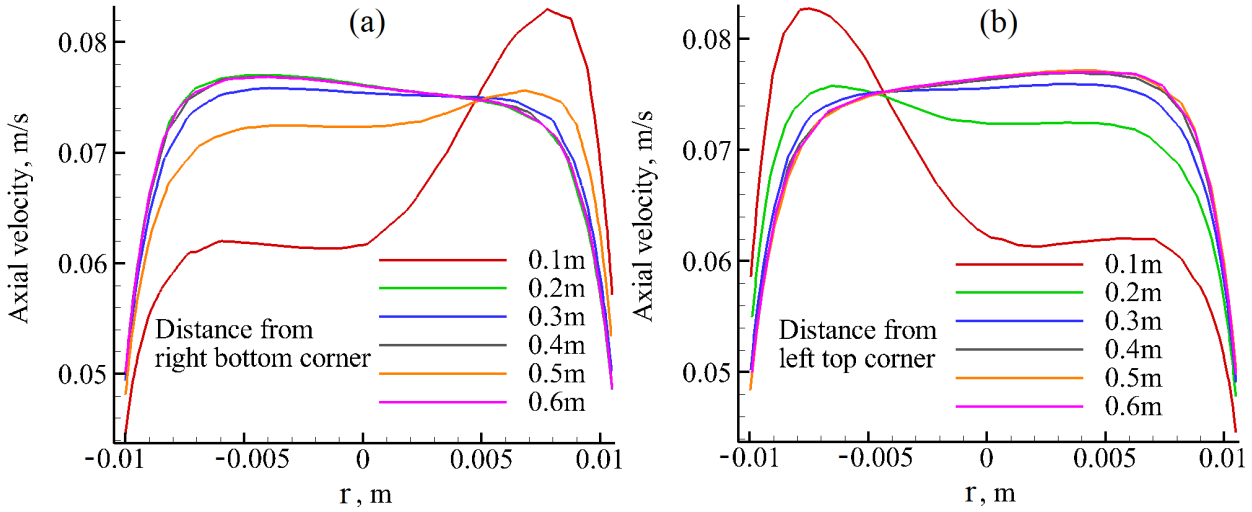

Figure 5.7: Velocity profiles in the reference case in the (a) "hot" and in the (b) "cold" leg.

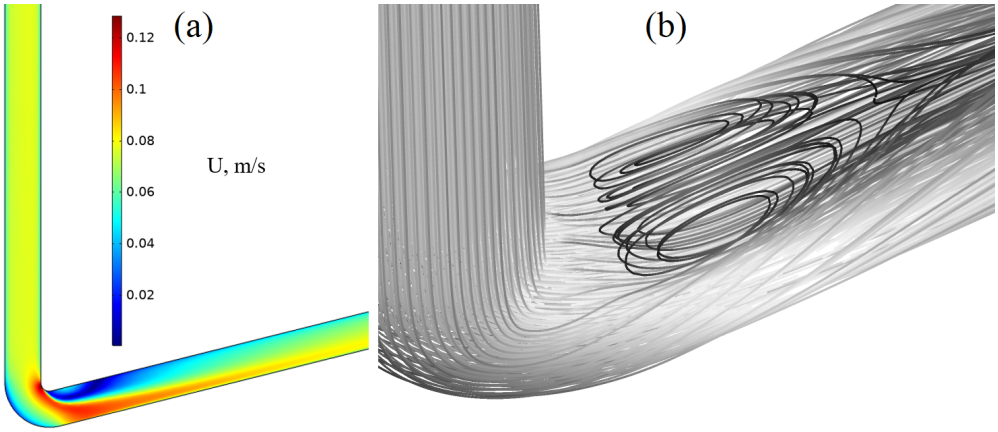

Figure 5.8: Reference case. Flow development effects. (a) Counter plot of the axial velocity component over the entire loop. (b) Formation of Dean vortices in the TCL corner.

pipe being swept towards the outer side of the bend while the fluid near the pipe wall returns towards the inside of the bend. This secondary motion appears as a pair of counter-rotating cells.

There have been many studies of this phenomenon for laminar, transitional and turbulent flows [70, 71] at different values of the Dean number, which is the key dimensionless parameter that defines laminar to turbulent transitions in flows with abrupt changes in the flow direction [70]. The Dean number is defined as $De = Re\sqrt{\gamma_c}$ where γ_c is the curvature ratio of the bend. Generally, if De is higher than 400, the flow is considered to be fully turbulent [71]. In this study, De varied from about 6500 to 10,000, suggesting a turbulent flow regime. The present findings regarding the flow in the corners are consistent with previous studies for pipe flows in the reference range of De.

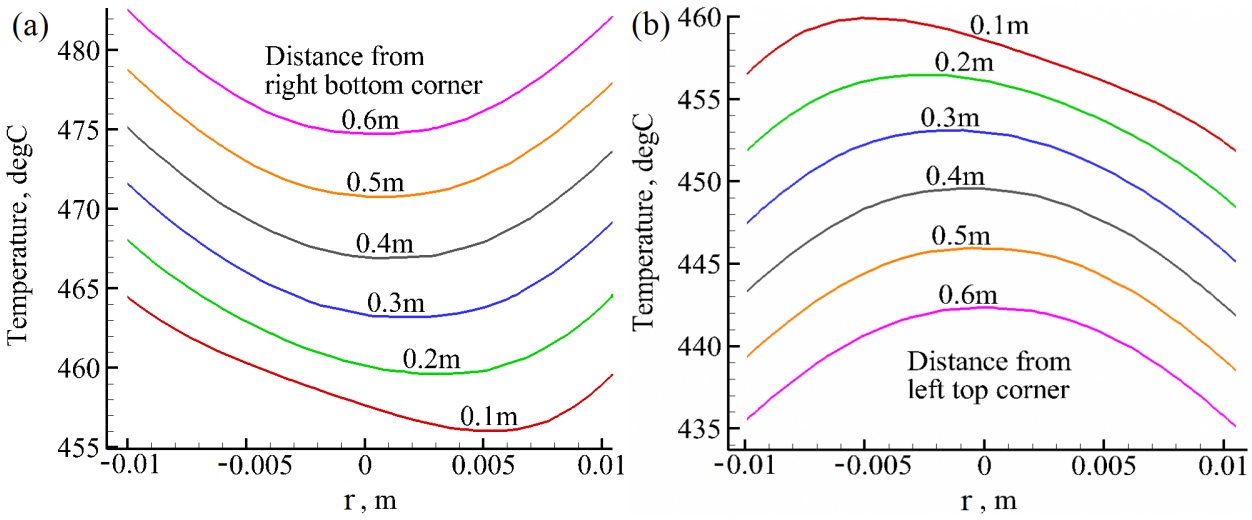

Figure 5.9: Temperature profiles in the reference case in the (a) "hot" the (b) "cold" leg.

Figure 5.9 shows the temperature profiles in the hot and cold legs. Similar to the velocity profiles, they also demonstrate anti-symmetry. The temperature increases almost linearly with the axial distance in the hot leg and decreases in the cold leg in the same manner. Higher temperatures occur near the center of pipe in the cold leg and near the walls in the hot leg. The radial non-uniformity of the temperature profiles can be characterized by the

ratio $\frac{T_{center}}{T_{wall}}$. For almost all temperature profiles plotted in Figure 5.9 in the hot leg, this ratio is about 1.02, so that the temperature profiles demonstrate high degree of uniformity due to the effect of buoyancy forces and turbulent mixing.

5.4.2 Effect of the heat flux

The heat flux is the most important operation parameter of the TCL as it affects the circulation velocity and maximum and minimum temperature in the loop. When planning experiments, a researcher has to select proper heaters to make sure that the required circulation velocities can be established. The velocity magnitude along with T_{max} and T_{min} can be predicted with the thermohydraulics code [72]. The effect of applied heat flux on flow characteristics is shown in Figure 5.10. Further analysis by COMSOL shows the effect of the applied heat flux on the velocity and the temperature field in the loop for three selected heat fluxes, 15, 20 and $26kW/m^2$. The results of these three cases are compared in Figure 5.11. Figure 5.11 shows the effect of q'' on the velocity profile in the middle of the vertical part of the hot leg. Clearly, a higher heat flux results in a higher circulation velocity but the shape of the velocity profile remains about the same. The same trend can be seen in the effect of q'' on the temperature profile in Figure 5.11. As mentioned earlier, the temperature profiles demonstrate high degree of uniformity in the radial direction. Figure 5.12 illustrates the corner flows for the same three heat fluxes. In all three cases, the Dean vortices are clearly seen but no qualitative differences can be observed in the location and size of the vortices.

5.4.3 Effect of the immersed samples

The samples immersed in the $PbLi$ in the loop obstruct the flow, resulting in lower velocities and higher T_{max} and lower T_{min}. This tendency is clearly seen in the results computed with the thermohydraulics code in Figure 5.13 where the circulation velocities and T_{max} and T_{min} are plotted as a function of the local pressure drop coefficient K. To investigate the effect of

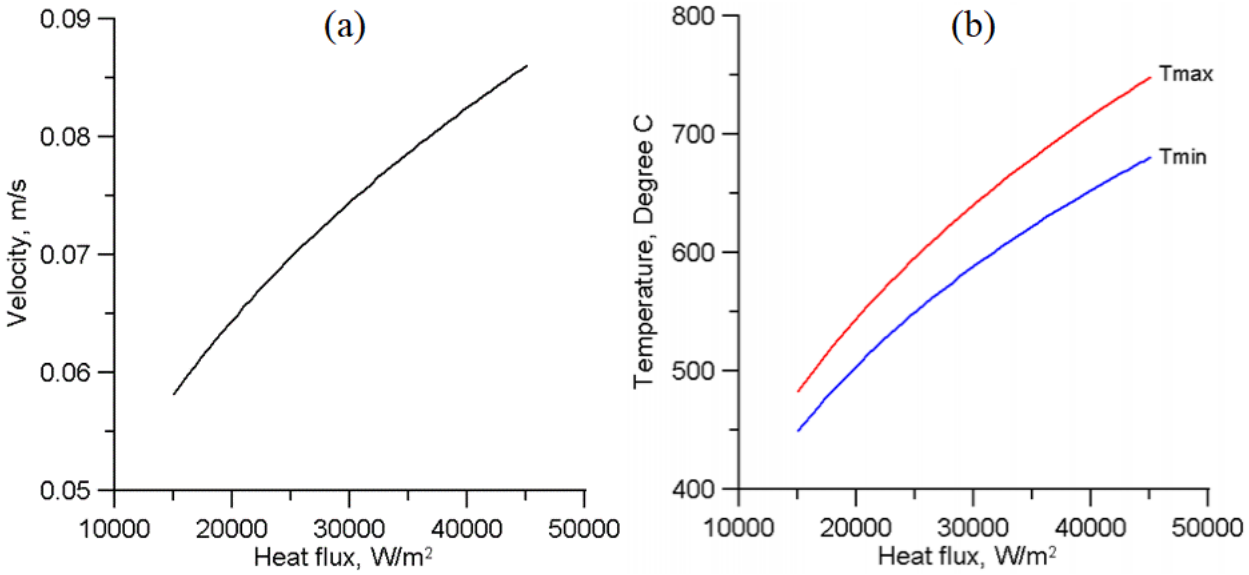

Figure 5.10: The (a) *PbLi* velocity and maximum and minimum *PbLi* temperatures (b) as a function of the applied heat flux in the TCL without samples. The surface emissivity of the cold leg is 0.78 (oxidized steel).

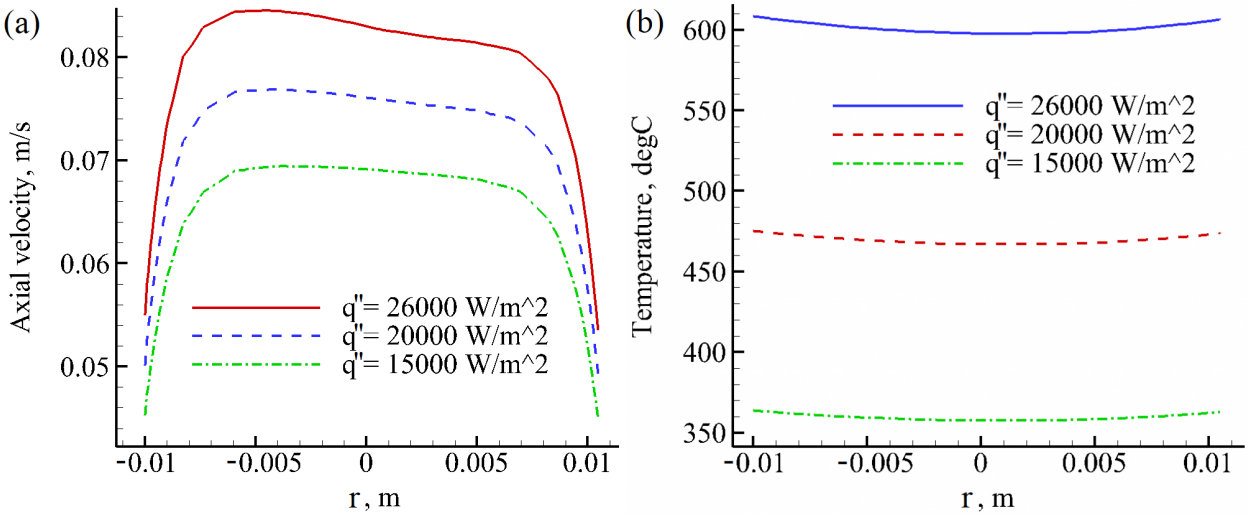

Figure 5.11: Effect of the applied heat flux on the velocity and temperature profile in the TCL in the middle of the vertical section of the "hot" leg. (a) Effect of q'' on the velocity profile. (b) Effect of q'' on the temperature profile.

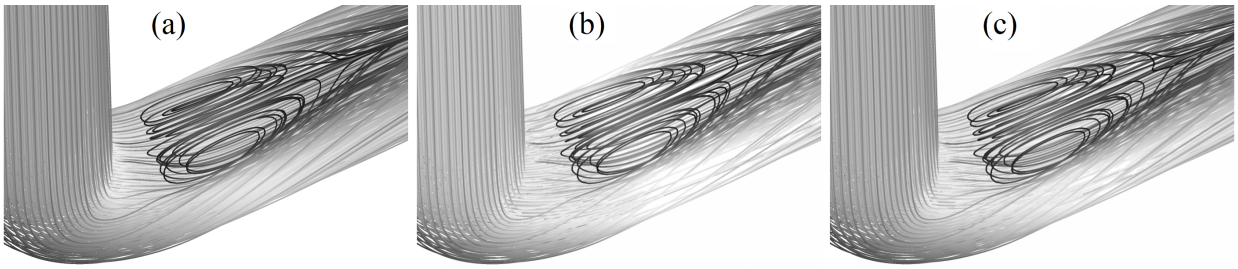

Figure 5.12: Effect of the applied heat flux on the *PbLi* flow in the corner region: (a) $q'' = 15kW/m^2$, (b) $q'' = 20kW/m^2$, (c) $q'' = 26kW/m^2$.

the immersed samples on the flow in more detail, COMSOL computations were conducted for two more cases at the same applied heat flux of $20kW/m^2$ as shown in Figure 5.14. In the case shown in Figure 5.14, the shape of the samples was simplified to elongated bars for faster computations. In the more experiment-relevant case in Figure 5.14, all 20 dogbone samples and 3 spacers in each sample chain were carefully modeled as shown in Figure 5.15. It should be noted that both the bar-like and the prototypic dogbone samples occupy the same volume inside the loop, which is about 1.64% of the entire loop volume. Any difference in the temperature or velocity is thus directly associated with the shape of the samples. Table 5.2 illustrates the differences in the computed results between three cases: the reference case (no samples), bar-like samples and dogbone samples with spacers.

Table 5.2: Summary of COMSOL computations for TCL with and without samples for $q'' = 20\ kW/m^2$ and $h = 45\ W/(m^2 \cdot K)$.

Case	$U,\ m/s$	$T_{max}, °C$	$T_{min}, °C$	$\Delta T, K$
Reference case (no samples)	0.0708	481.63	435.05	46.58
Bar-like samples	0.067	483.85	433.8	50.05
Dogbone samples	0.0568	489.43	430.26	59.17

As seen from the table, the maximum circulation velocity occurs in the TCL loop without samples. Slightly lower velocity (5.5% difference) is seen in the TCL with bar-like samples.

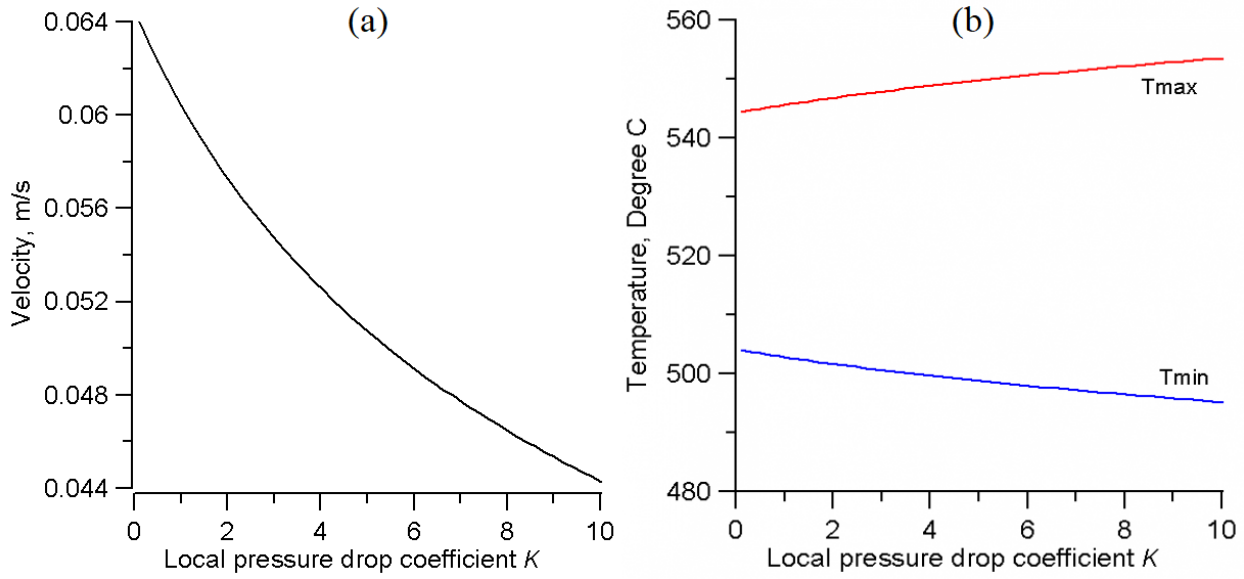

Figure 5.13: Effect of corrosion samples immersed in the liquid metal on the velocity and temperature at $q'' = 20\ kW/m^2$ and $\epsilon = 0.78$: (a) $PbLi$ velocity, and (b) maximum and minimum temperatures.

The lowest velocity occurs in the loop with the dogbone samples (19.8% reduction compared to the reference case). This case also demonstrates the highest temperature difference of all three cases.

Figure 5.16 shows cross-sectional velocity and temperature distributions in the middle of the vertical section of the hot leg where the flow becomes fully developed. There is a clear asymmetry in the velocity distributions such that higher velocity in all three cases occurs in the left (inner) half of the pipe. This might indicate the influence of the corner flows. Figure 5.17 shows the flows in the corner. All three cases demonstrate Dean vortices. Similar to the previous analysis of the applied heat flux, no significant variations have been observed.

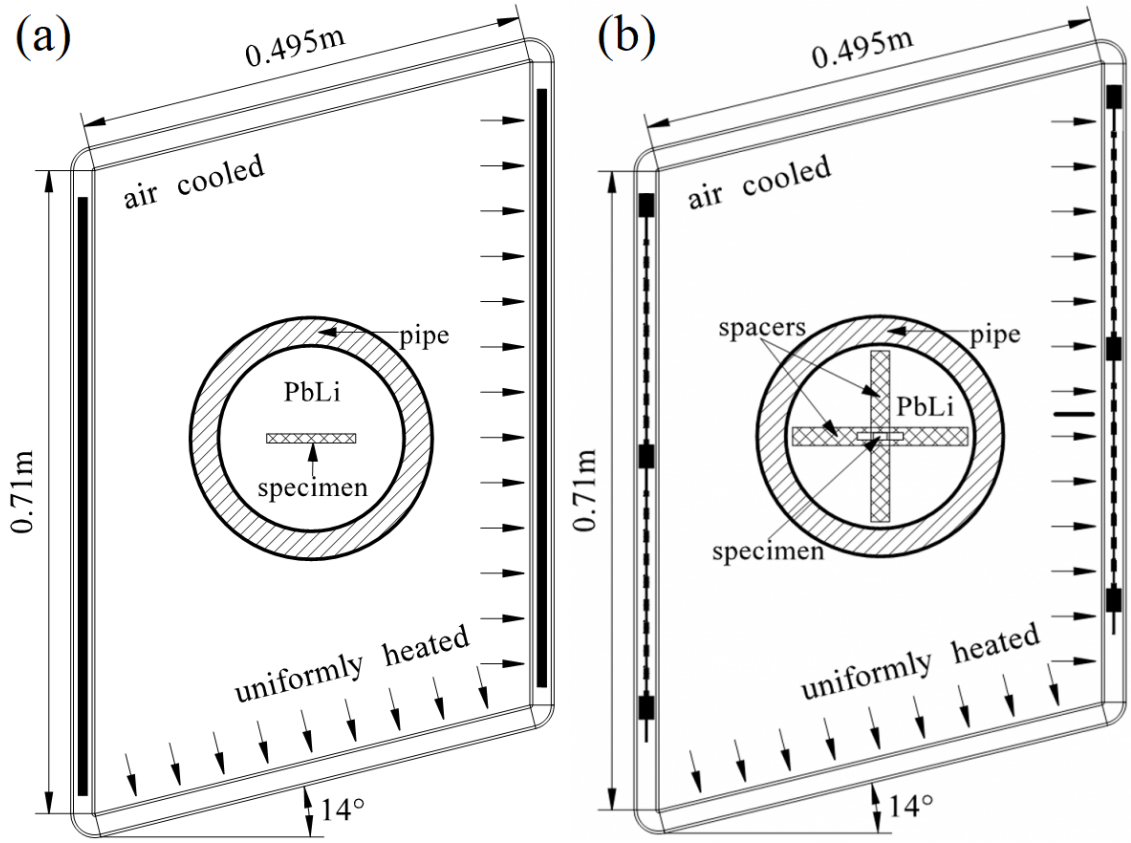

Figure 5.14: Schematics of the TCL loop with the immersed corrosion samples: (a) Simplified bar-like samples, (b) A chain of dogbone samples with spacers.

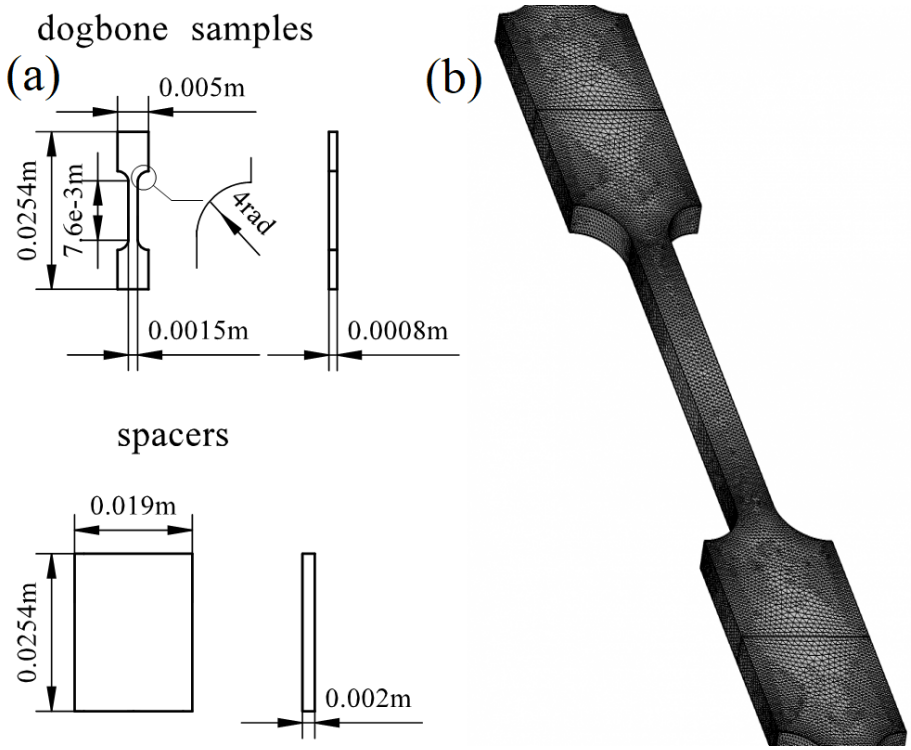

Figure 5.15: Model of dogbone samples and spacers in COMSOL. (a) Schematics with dimensions. (b) Finite-element tetrahedral mesh of 90,000 elements inside each sample.

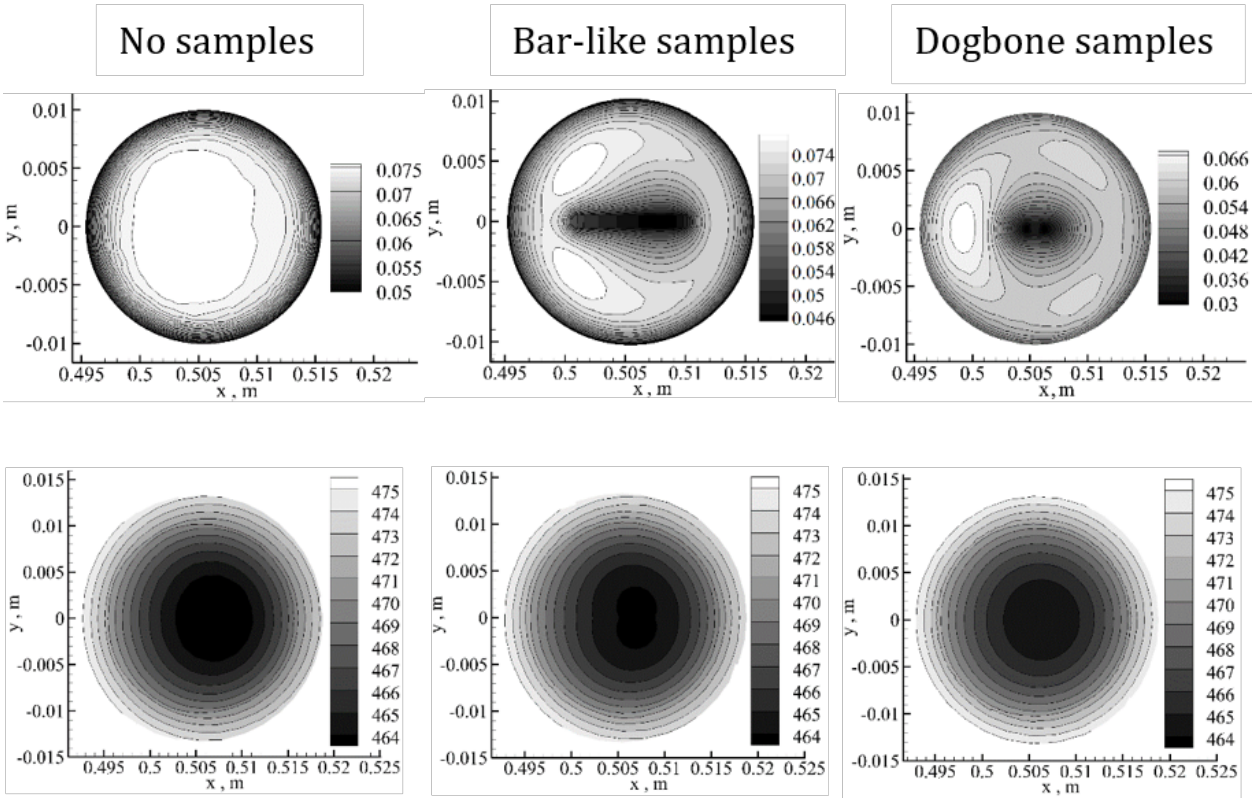

Figure 5.16: Comparison of the (upper) velocity and (lower) temperature distribution in the middle of the vertical section of the "hot" leg, including the case with (left) no samples, (middle) bar-like and (right) dogbone samples.

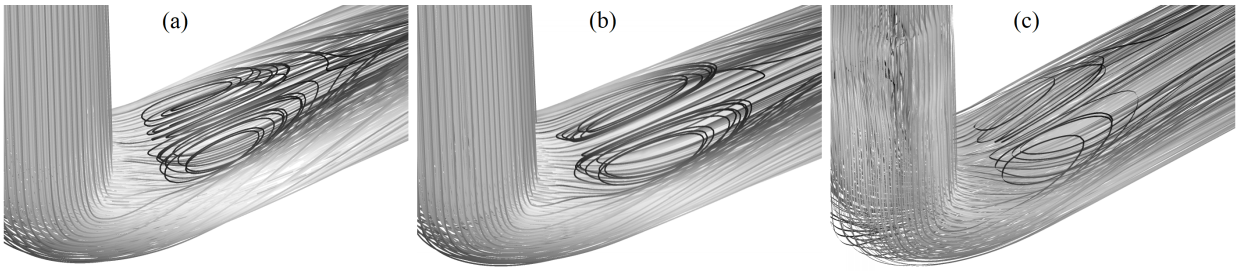

Figure 5.17: Comparison of the flow in the corner region for three cases: (a) with no samples, (b) bar-like and (c) dogbone samples.

5.5 Comparisons between the thermohydraulics code and COMSOL

Comparisons between the thermohydraulics code and COMSOL have been done for the circulation velocity and T_{max} and T_{min} for the TCL flow without samples as shown in Figure 5.18.

The thermohydraulics code is a self-developed code based on Fortran by Dr. Smolentsev to accurately compute all kinds of TCL related parameters. The code solves the bulk flow and heat transfer equations to give an accurate estimate of bulk circulation velocity and temperature values for comparison, combined with other possible effects. The code can also be applied to the data analysis in corrosion experiments to evaluate the effect of temperature and velocity on corrosion rates. The main capabilities of the code include: (1) estimation of the circulation flow velocity and maximum and minimum temperatures in the loop as a function of the applied heat flux, (2) analysis of the flow with and without the samples for various sample shapes and sizes, (3) analysis for laminar and turbulent flows, (4) analysis of the effect of a magnetic field on the liquid metal flow in the loop, and (5) analysis of the cooling conditions in the cold leg, including convection and radiation losses. These capabilities are further. The details of the code and equations solving procedures can be found in [72].

A range of heating power from 1.2 to $3.5kW$ was covered in the computations with the thermohydraulics code while only three flows corresponding to 1.5, 2.0 and $3.6kW$ were computed with COMSOL. For these three flows, the computed parameters with the two codes are in a very good match.

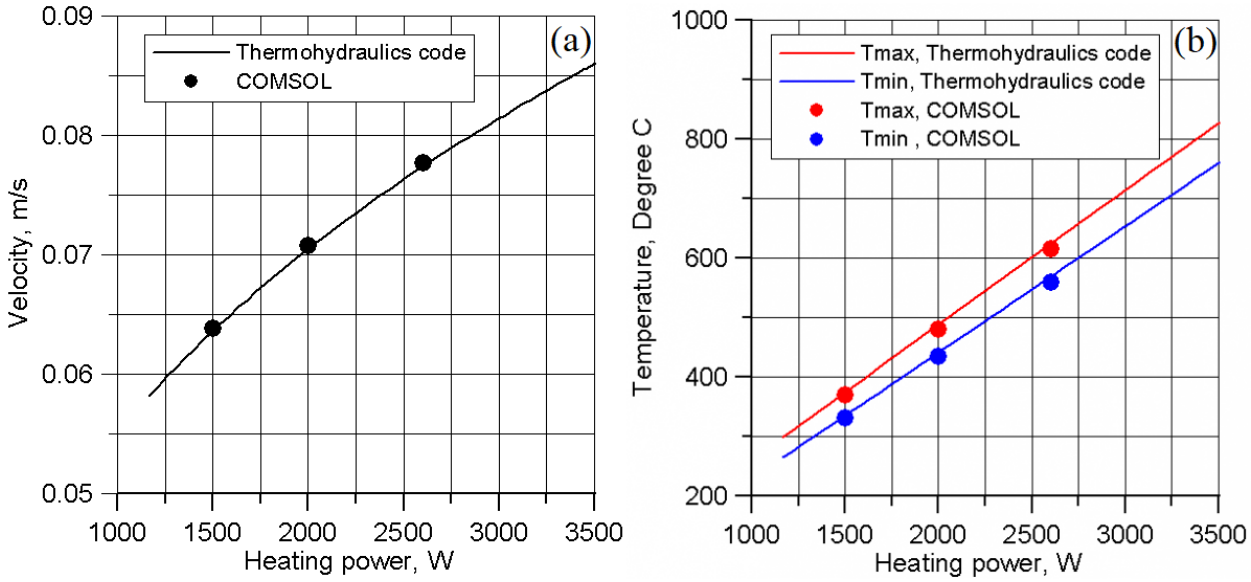

Figure 5.18: Comparisons between the thermohydraulics code and COMSOL at $h = 45W/(m^2 \cdot K)$: (a) $PbLi$ velocity, and (b) maximum T_{max} and minimum T_{min} $PbLi$ temperature.

CHAPTER 6

Optimization studies for blanket manifolds

6.1 Mathematical formulation of the problem

A sketch illustrating an MHD flow in a section of the inlet manifold with a gradual expansion is shown in Figure 6.1. The LM enters the manifold through a small rectangular duct with the width $2d$, height $2a$, and the length L_{in} at the velocity of U_{in}. From there, it flows into the expansion region with the length L_{exp}, and then proceeds into a big rectangular duct of the width $2b$ and the length L_{out}. The entire length of the manifold is $L = L_{in} + L_{exp} + L_{out}$. The flow occurs in the presence of a uniform transverse magnetic field of induction B.

The Cartesian coordinate system is chosen in such a way that the flow occurs along the x axis and the magnetic field is parallel to the y axis. Three expansion angles θ are studied: $45°, 60°$ and $75°$. The fourth case of a sudden expansion $\theta = 90°$, which is shown in Figure 6.2, was studied earlier in [4] and is used here for testing and comparing against the present results. The duct dimensions are shown in Table 6.1. These parameters are kept unchanged in all the computations. The expansion ratio is defined as $\gamma_{exp} = \frac{b}{d}$ and is fixed at 4. The liquid metal eutectic alloy $PbLi$ is used as the working fluid with density ρ, kinematic viscosity ν and electrical conductivity σ defined at the temperature $500°C$ [73] and given in Table 6.2. The duct walls are assumed to be electrically non-conducting, such that the computations are limited to the flow domain. This model is a close approximation to the conditions of a real DCLL blanket where the $PbLi$ flow is decoupled from the electrically conducting steel walls with an insulating flow channel insert (FCI) [74]. The $PbLi$ inlet

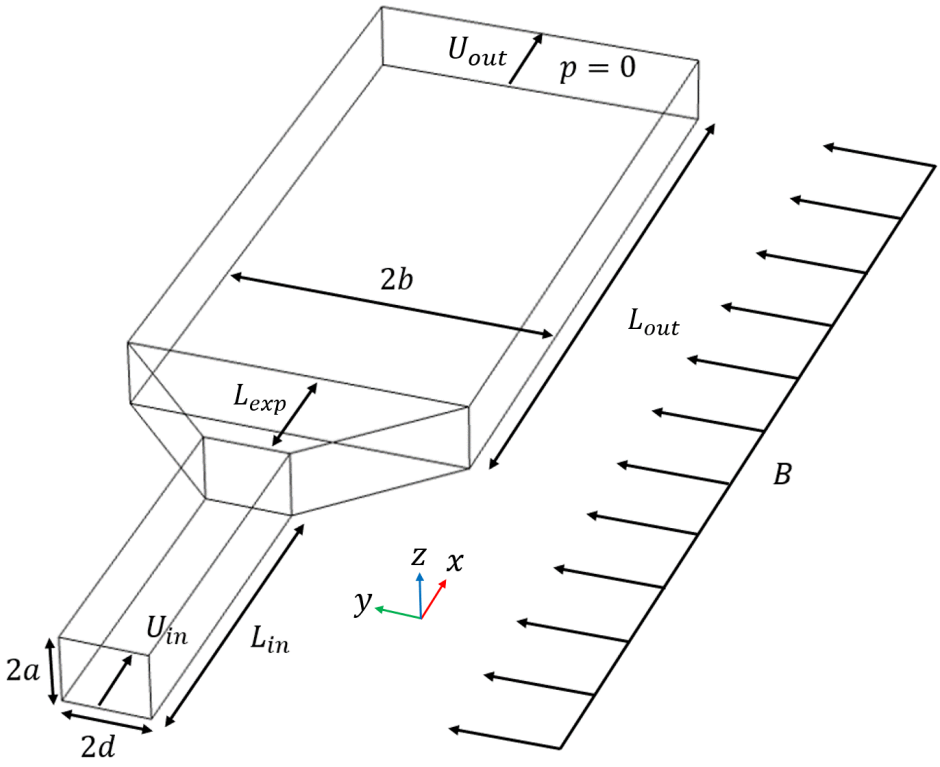

Figure 6.1: Geometry for gradual expansion manifold case.

velocity U_{in} and the magnetic field strength B are varied to assure the Hartmann and Reynolds numbers in the computations up to $10,000$.

Table 6.1: Geometry details of gradual expansion manifold

Upstream duct half width (d)	$0.05\ m$
Downstream duct half width (b)	$4d = 0.2\ m$
Duct half height (a)	$0.8d = 0.04\ m$
Upstream duct length (L_{in})	$4d = 0.2\ m$
Downstream duct length (L_{out})	$4b = 0.8\ m$
Expansion ratio (b/d)	4
Expansion region length (L_{exp})	$3d \cdot cot\theta\ m$

Table 6.2: *PbLi* liquid metal properties used in study

Density (ρ)	$9600\ kg/m^3$
Dynamic viscosity (μ)	$0.0011436\ Pa \cdot s$
Electric conductivity (σ)	$8.1236 \times 10^5\ S/m$

For the described problem of LM MHD flow in blanket inlet manifold, it corresponds to the second model mentioned in section 4.1, solving Eqs. 4.4∼4.6, 4.9. Therefore, the governing equations can be written as:

$$(\nabla \cdot \mathbf{v}) = 0$$

$$\frac{\partial \mathbf{v}}{\partial t} + \mathbf{v} \cdot \nabla \mathbf{v} = -\frac{1}{\rho}\nabla p + \nu \nabla^2 \mathbf{v} + \frac{1}{\rho}\mathbf{J} \times \mathbf{B}$$

$$\mathbf{J} = \sigma\left(-\nabla\phi + \mathbf{v} \times \mathbf{B}\right)$$

$$\nabla^2 \phi = \nabla \cdot (\mathbf{v} \times \mathbf{B})$$

The fluid flow satisfies no slip/no flow through conditions, and the inlet flow is set as fully developed, with a outlet pressure of 0. Electrical insulation needs to be applied to all

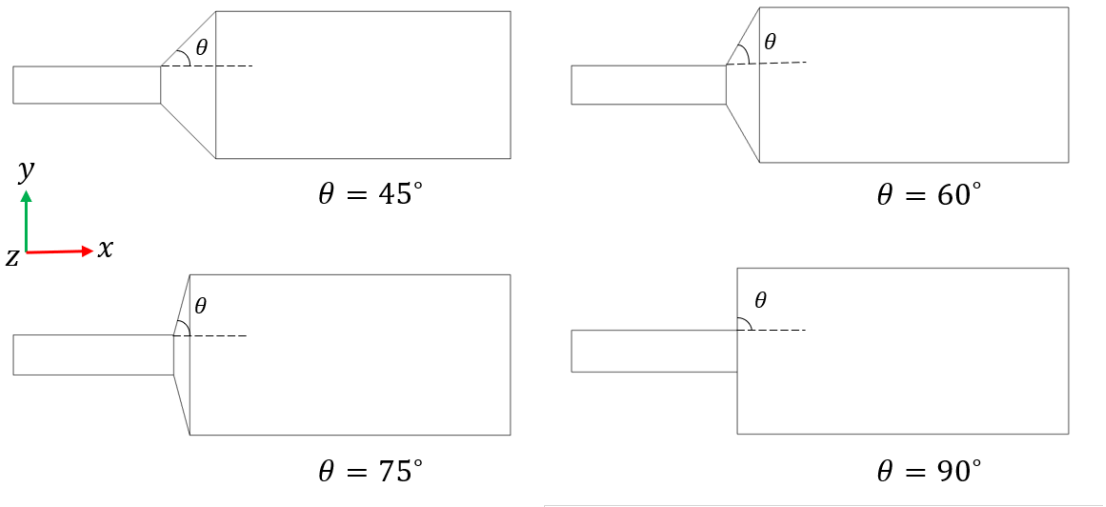

Figure 6.2: Schematic illustration of different expansion angle cases.

the outer boundaries, with current conservation enforced in the fluid domain. The electrical insulation is applied at the outer boundaries, including inlet and outlet. The main dimensionless parameters used for flow characterization and correlation construction are the Ha and Re. The characteristic length is the half duct width of the downstream big duct b and the characteristic velocity is the outflow velocity U_{out} shown in Figure 6.1.

The computational matrix for MHD flow in a manifold is shown in Table 6.3. In the matrix, the Ha varies from 1000 to 10,000, while the Re varies from 1000 to 10,000 as well. The interaction number $\frac{Ha^2}{Re}$ is calculated in the table. It is an indication of relative magnitude of electromagnetic forces and inertia forces. From the geometry perspective, by adjusting L_{exp}, the angle of expansion from small duct to large duct can be changed correspondingly. As mentioned, three different angles are chosen ($\theta = 90°$ has been studied). The total number of cases computed is 150 for 5 different Ha, 10 different Re and 3 expansion angles.

Table 6.3: Interaction number N for different Ha and Re cases

Ha/Re	50	100	200	400	600
1000	20000	10000	5000	2500	1667
3000	180000	90000	45000	22500	15000
5000	500000	250000	125000	62500	41667
7000	980000	490000	245000	122500	81667
10000	2000000	1000000	500000	250000	166667
Ha/Re	1000	2000	3000	5000	10000
1000	1000	500	333	200	100
3000	9000	4500	3000	1800	900
5000	25000	12500	8333	5000	2500
7000	49000	24500	16333	9800	4900
10000	100000	50000	33333	20000	10000

6.2 Validation case for the numerical tool

In order to validate the ability of COMSOL Multiphysics in predicting MHD flow in a duct or manifold, a test case was chosen. As mentioned, fully developed 2D MHD duct flow solutions were obtained by Hartmann, Shercliff and Hunt using Fourier series and Walker using asymptotic expansions. A proper code has already been established to compute the exact solutions given in their papers. However, applicability of fully developed 2D MHD duct flow doesn't necessarily mean an acceptable prediction for 3D MHD flow. The computational tool needs to be further examined for its accuracy in 3D MHD benchmark cases in comparison to existing correlations given for 3D MHD pressure drop. Therefore, the validation problem features the solution of 3D MHD manifold flow in a straight insulating rectangular duct with sudden expansion, when a uniform transverse magnetic field is present. A sketch of the problem is shown in Figure 6.3. The details of geometry used for the validation are shown in Table 6.4.

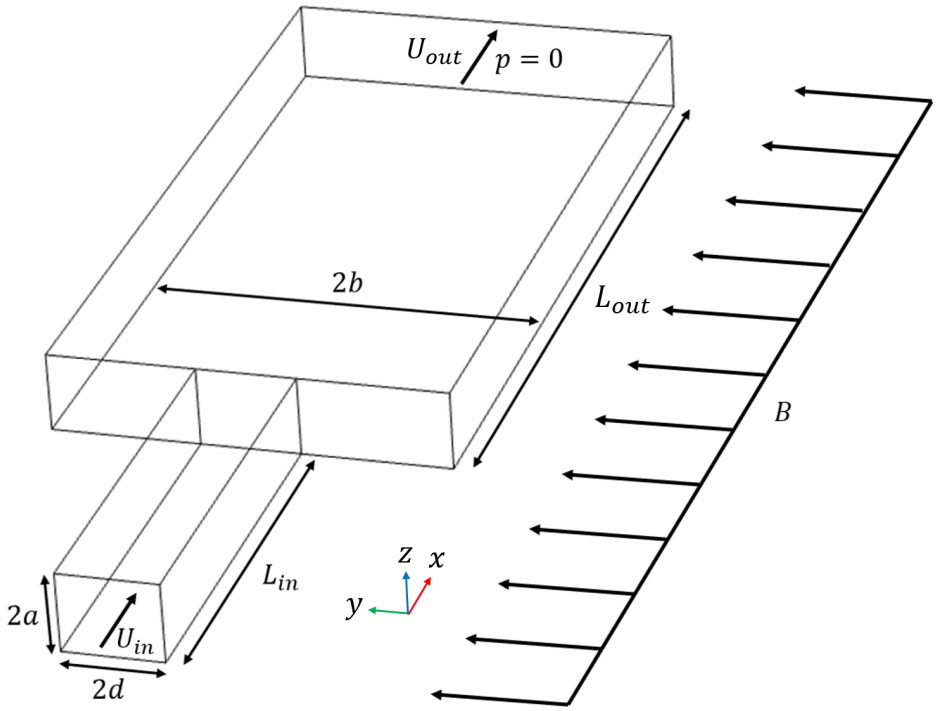

Figure 6.3: Schematic illustration of 3D MHD flow in sudden expansion manifold for validation.

Table 6.4: Geometry details of validation case

Upstream duct half width (d)	$0.05\ m$
Downstream duct half width (b)	$4d = 0.2\ m$
Duct half height (a)	$0.8d = 0.04\ m$
Upstream duct length (L_{in})	$4d = 0.2\ m$
Downstream duct length (L_{out})	$4b = 0.8\ m$
Expansion ratio (b/d)	4

The computational tool needs to be examined for both 2D and 3D MHD flow prediction capability. The results of 2D fully developed MHD flow in a rectangular duct involve both upstream and downstream profiles in two cross sectional directions, which are shown in Figure 6.4. As can be seen from the comparison, COMSOL exhibits perfect description of characteristics for 2D MHD flow.

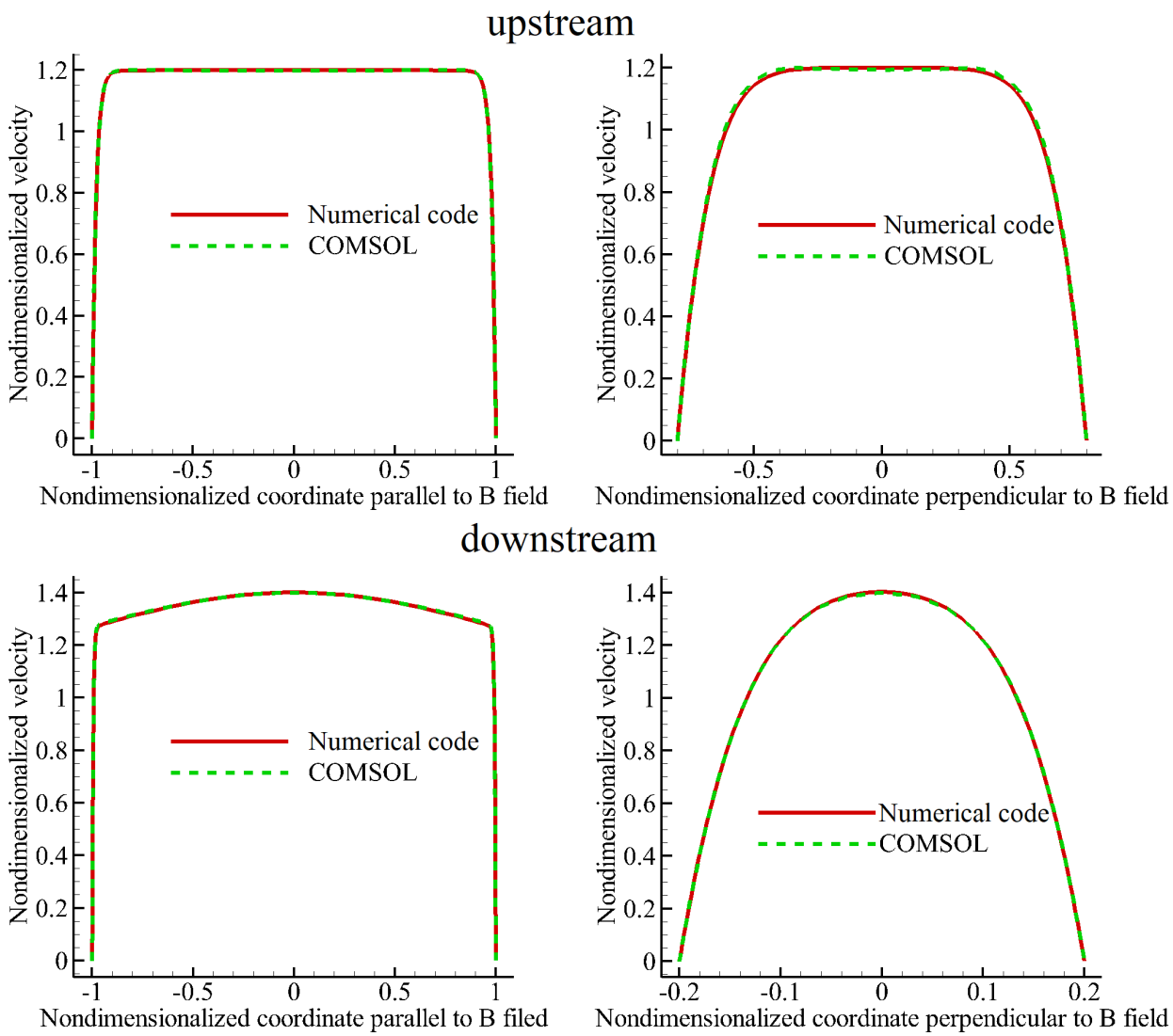

Figure 6.4: Comparison between analytical [3] and computed solution for 2D fully developed MHD flow upstream and downstream.

The 2D fully developed MHD pressure drop relations for both electrically conducting and insulating duct with rectangular or circular cross section can be written in the following form with λ as the pressure drop coefficient:

$$\Delta P = \lambda \frac{\rho U^2}{2} \frac{x}{L},$$

where length scale is defined as:

$$L = \begin{cases} b, \text{ half duct width for rectangular duct} \\ R, \text{ radius for circular pipe} \end{cases}.$$

For rectangular duct and insulating wall, the approximate correlation that takes into account flow resistance in the Hartmann and side layers was obtained by Shercliff [33]:

$$\lambda = \frac{2Ha}{Re} \left(1 - \frac{1}{Ha} - \frac{0.852}{\beta Ha^{\frac{1}{2}}} \right)^{-1}.$$

If Hartmann walls are insulating, side walls are perfectly conducting, then for rectangular duct, Hunt et al. [37] gives:

$$\lambda = \frac{2Ha}{Re} \left(1 - \frac{0.956}{\beta Ha^{\frac{1}{2}}} - \frac{1}{Ha} \right)^{-1}.$$

If all walls are perfectly conducting for a rectangular duct, from Branover [75]:

$$\lambda = \frac{2Ha^2}{Re} \cdot \frac{1}{1 - Ha^{-1} - 2.4 Ha^{-\frac{3}{2}} \beta^{-1}}.$$

For circular pipe and insulating wall, the relation is obtained by Shercliff [76]:

$$\lambda = \frac{3\pi Ha}{4Re} \left(1 - \frac{3\pi}{4Ha} \right)^{-1}.$$

For circular pipe and conducting wall, if $Ha \gg 1$, asymptotic relation was obtained in [77]:

$$\lambda = \frac{3\pi Ha}{4Re} \left(1 + 0.883 c_w Ha - 0.019 \left(c_w Ha \right)^2 \right).$$

In [4], 3D MHD pressure drop correlations ΔP_{3D} were obtained from computations for a wide range of parameters:

$$\Delta P_{3D} = \begin{cases} \frac{\rho U^2}{2}\left(k_{ve} N \cdot Ha^{-1/2} + d_{ve}\right), \frac{Ha^{3/2}}{N} < 3 \\ \frac{\rho U^2}{2}\left(k_{ie} N^{2/3} + d_{ie}\right), \frac{Ha^{3/2}}{N} > 3 \end{cases},$$

where

$$\begin{cases} k_{ve} = 0.31\gamma_{exp} + 3.08 \\ d_{ve} = 342.92\gamma_{exp} - 1563.85 \end{cases}, \begin{cases} k_{ie} = 0.33\gamma_{exp} + 1.19 \\ d_{ie} = -11.55\gamma_{exp}^2 + 85.43\gamma_{exp} - 264.39 \end{cases}.$$

In the test case, $Ha = 1000$ and $Re = 210$, therefore according to the paper [4], $\Delta P_{3D} = 603.0 \times \frac{\rho U^2}{2}$. The result computed by COMSOL, derived from the difference of pressure when assuming fully developed 2D MHD flow, is shown in Figure 6.5 with a predicted $\Delta P_{3D} = 587.2 \times \frac{\rho U^2}{2}$. The relative difference for these two results is 2.6% which indicates a very good match between the empirical correlation and COMSOL computation. Here we should note that U in [4] indicates the bulk velocity downstream of the rectangular duct, which is U_{out} in the sketch.

The validations of 2D and 3D MHD flow cases prove COMSOL to be a suitable tool in computing related MHD problems. A slightly different geometry with the same physical setting will be used in the next part.

6.3 Computational setup in COMSOL

As stated, the main goals of the current study is to compare the 3D pressure drop of different manifold designs and establish the correlations for calculating pressure drop for a more gradual expansion geometry. The sudden expansion validation cases are utilized in further comparisons, while the mainly computed gradual expansion manifold model is shown in Figure 6.1. It adds an extra parameter of expansion length L_{exp} in the geometry, which can be used to adjust the gradualness of the transition from the smaller upstream duct to larger

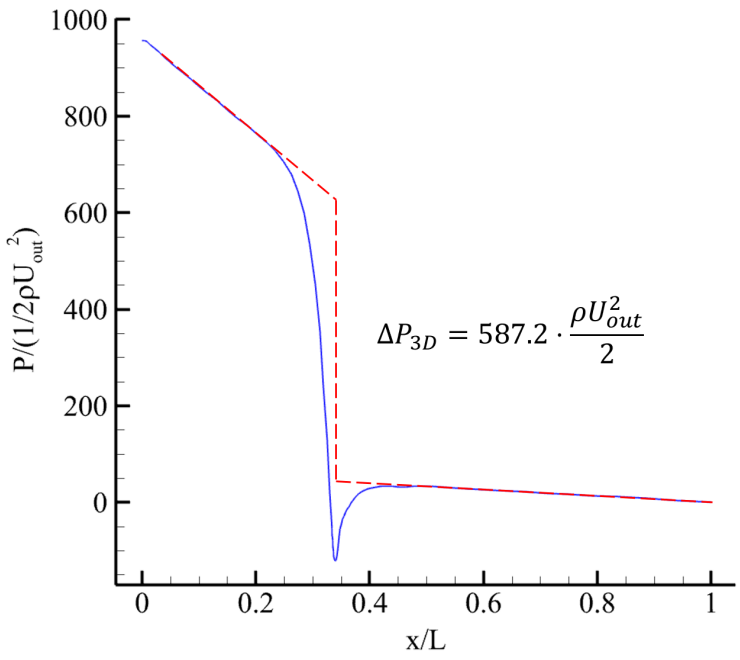

Figure 6.5: Comparison of 3D pressure drop result between relation given by [4] and by validation case in COMSOL.

downstream duct. All other parameters are basically the same as in sudden expansion cases, and the walls are insulating as well.

MHD flow, whether 2D or 3D, is a fluid flow added with electric current loops inside, which generate flow-obstructing Lorentz force that reshapes the flow. Therefore, it cannot be characterized merely by hydrodynamic Re number. For this reason, the dimensionless numbers Re and Ha combined can characterize the flow. Based on experimental data [75], the flow can be considered as laminar if $\frac{Ha}{Re} > (\frac{Ha}{Re})_{cr}$, where $(\frac{Ha}{Re})_{cr} = \frac{1}{130}$ for span-wise magnetic field, $(\frac{Ha}{Re})_{cr} = \frac{1}{225}$ for wall-normal magnetic field, $(\frac{Ha}{Re})_{cr} = 2.5 \times 10^{-2}$ for stream-wise magnetic field. In the planned cases, the lowest Ha/Re combination is $Ha = 1000, Re = 10,000$, which means laminar solver should be chosen for all the cases.

In COMSOL, when using physics definition, various options can be chosen. The "Magnetic and Electric Fields" physics from AC/DC module can help couple the electric current

with the magnetic field applied. However, difficulty arises in defining a single component constant magnetic field corresponding to the middle part of magnets as in the problem. Also, the induced magnetic field are not present under inductionless approximation when magnetic Reynolds number is much smaller than unity. On the other hand, under "Electric currents" physics the magnetic field can be manually coupled into "external current density" term, where the flow-induced currents can be taken into consideration. Meanwhile, in "Laminar flow" physics, the Lorentz force can be inserted in the equation as a volume force term, with its formula mentioned before. In this way, the manual coupling of electric currents and fluid flow can be realized.

Based on the already exist analytical solutions for duct MHD flow, the flow in this type of problems is expected to reach a steady state. Primarily, a finite element based stationary solver is selected.

In stationary computations, the electric currents and laminar flow are solved simultaneously. The direct solver was chosen by using "PARDISO" (Parallel Direct Sparse Solver), which can take advantage of shared memory multiprocessors to solve large sparse linear systems of equations. However, the direct solvers, although significantly faster than iterative solvers, consume a lot of memory. Even though an "out of core" mode can be turned on to allocate extra memory using hard disc drive, the speed is rather limited in data transmission. Therefore, the storage of RAM (512GB) was used only. A "fully coupled" or "segregated" approach are tested for the trade-off between memory and computational time for such a complicated computation. The fully coupled solver is more memory consuming compared to the segregated solver, but it was found to be significantly faster. For example, the case of $Ha = 1000, Re = 210, \theta = 60^\circ$ required about 6 hours to converge with the fully coupled solver while the use of a segregated solver resulted in more than 10 days of computations. It should be noted that upon convergence, both solvers give the same results, shown in Figure 6.6. In all the cases, the "Double dogleg" nonlinear solver was chosen. The nonlinear solver is a sophisticated combination of the Steepest descent and Newton-Raphson methods,

which has a maximum iteration number of 100. The whole solver uses a relative residual tolerance of 1×10^{-6}, meaning that both linear and nonlinear solver need to meet this criterion for convergence.

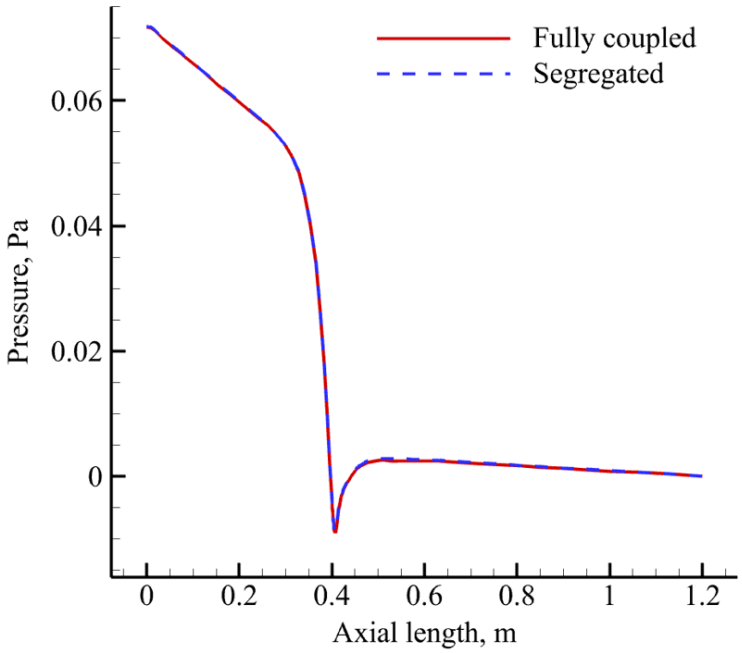

Figure 6.6: Pressure distribution along center axis for fully coupled and segregated approach, $Ha = 1000, Re = 210, \theta = 60°$.

Firstly, a mesh sensitivity study was performed for the case. Due to the symmetric nature of the problem in direction parallel to magnetic field, the geometry is reduced into half to enable a more rapid computation using direct solver. Corresponding symmetry boundaries are added for fluid flow and electric currents. Three types of meshes were constructed for the gradual expansion geometry, with coarse, normal and fine mesh details shown in Figure 6.7. The axial pressure and fully developed velocity profile for selected cross section of three cases are shown in Figure 6.8. From the comparison, conclusion can be made that the normal mesh is enough to resolve the problem. It includes 50 points for the side layer direction with 12 in the side layer, 40 points for half of the geometry in Hartmann layer direction (parallel to magnetic field) with 8 points in Hartmann layer. In the axial direction there are a total

of 110 points with nonuniform distribution. The mesh cells are made clustered near the beginning and end of expansion region to capture flow variations and the total number of mesh elements is 220,000.

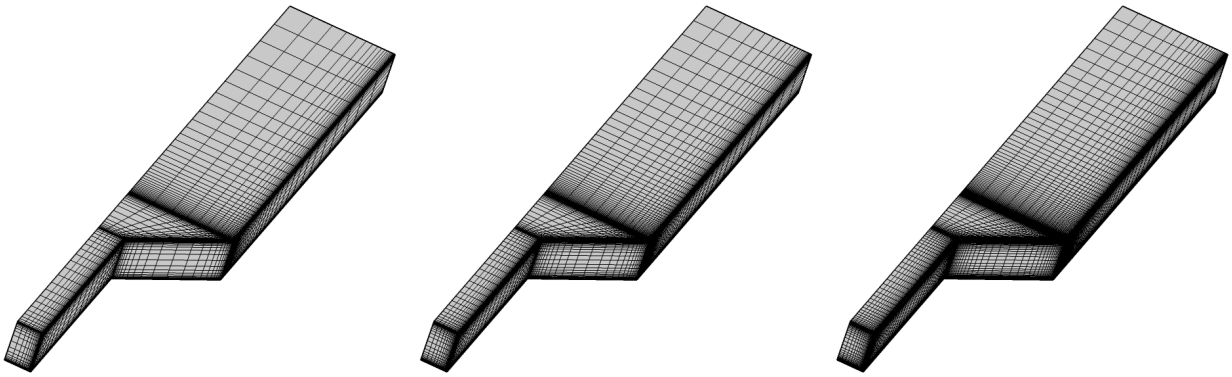

Figure 6.7: Structured meshes with different density used in COMSOL computations: (left) coarse, (middle) normal and (right) fine.

6.4 Flow characterization and distributions

For MHD flow in a manifold, the flow characteristics, including velocity distributions, electric potential, electric currents, and pressure distribution are shown in the current section.

In the small upstream duct and large downstream duct, the flow exhibits fully developed 2D MHD characteristics after certain distance. In fact, the small and big ducts were chosen to be long enough compared to the expansion region to make sure that the MHD flow in these two sections is about fully developed to assure that the flow in the expansion, which is of the most interest in this study, is not affected by the inlet and outlet. The case with $Ha = 1000, Re = 210, \theta = 45^{\circ}$ is chosen to represent this phenomenon. The 2D fully developed velocity profile for small duct is shown in Figure 6.9(a) and large duct shown in Figure 6.9(b). The velocity possesses a highly uniform core with thin boundary layers near the wall. In the fully developed flow region upstream in the smaller duct and

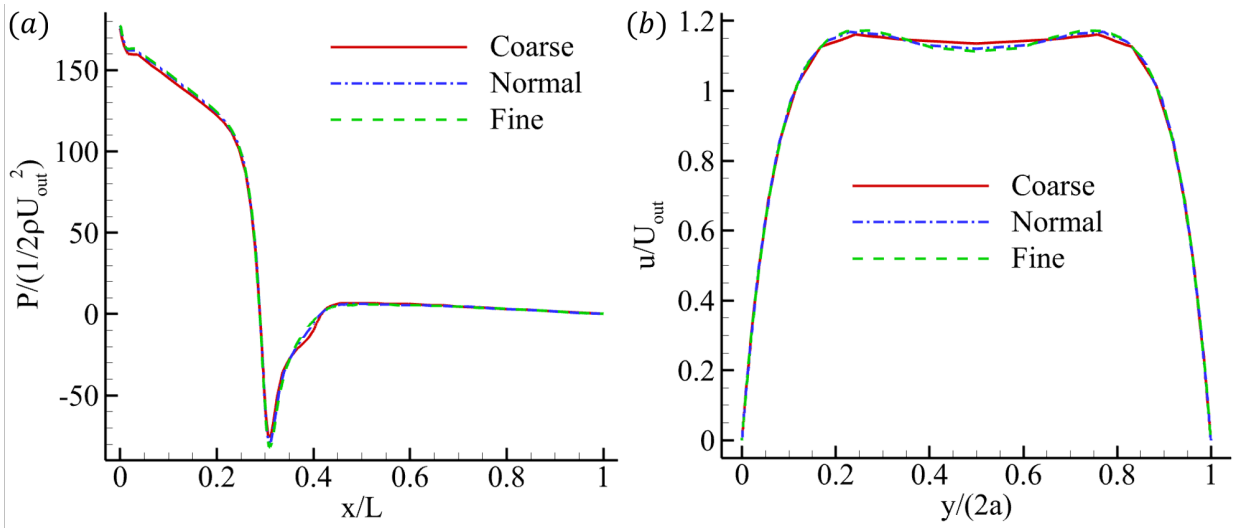

Figure 6.8: Comparison of computed results for three meshes, coarse, normal and fine, (a) axial pressure and (b) velocity profile.

downstream in the larger duct, the electric currents are two dimensional, and so is the flow. The electric currents form loops in the half cross section and are symmetric with respect to the geometric symmetry plane, shown in Figure 6.10. The electric potential change for fully developed upstream and downstream duct are shown in Figure 6.11(a) and Figure 6.11(b). From the figures, a linear change of electric potential can be observed for both the upstream and downstream duct, which corresponds to the steady state solution for 2D MHD duct flow.

To further characterize the 3D MHD flow, similar variables are plotted for the whole geometry. Here, the case of inlet manifold with insulating wall, and $Ha = 5000$, $Re = 1000$, $\theta = 60°$ is chosen to demonstrate the flow patterns, shown in Figure 6.12. These parameters are about in the middle of the computational matrix, such that the observed flow features are common to almost all computed cases. When the flow enters the expansion region from the small duct, it experiences 3D effects, while in the small inlet duct itself and in the big outlet duct the flow is mostly 2D. When entering the expansion region, the flow experiences strong electromagnetic forces, resulting in the deflection of the flow from its main axial direction towards the walls as seen in Figure 6.12(a)(b). The velocity profile here becomes

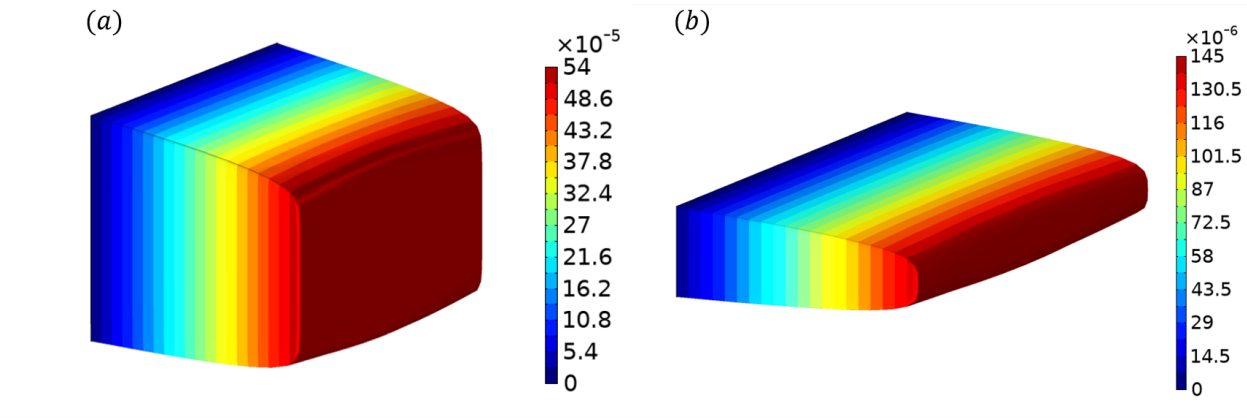

Figure 6.9: Upstream and downstream fully developed MHD flow velocity profile for case $Ha = 1000,\ Re = 210, \theta = 45°$.

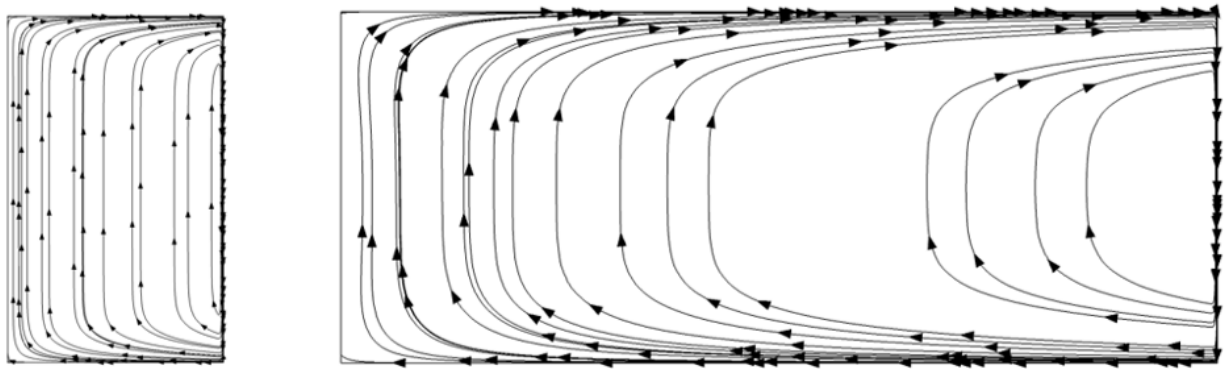

Figure 6.10: Electric currents in the half cross section for half of upstream and downstream duct for case $Ha = 1000,\ Re = 210, \theta = 45°$.

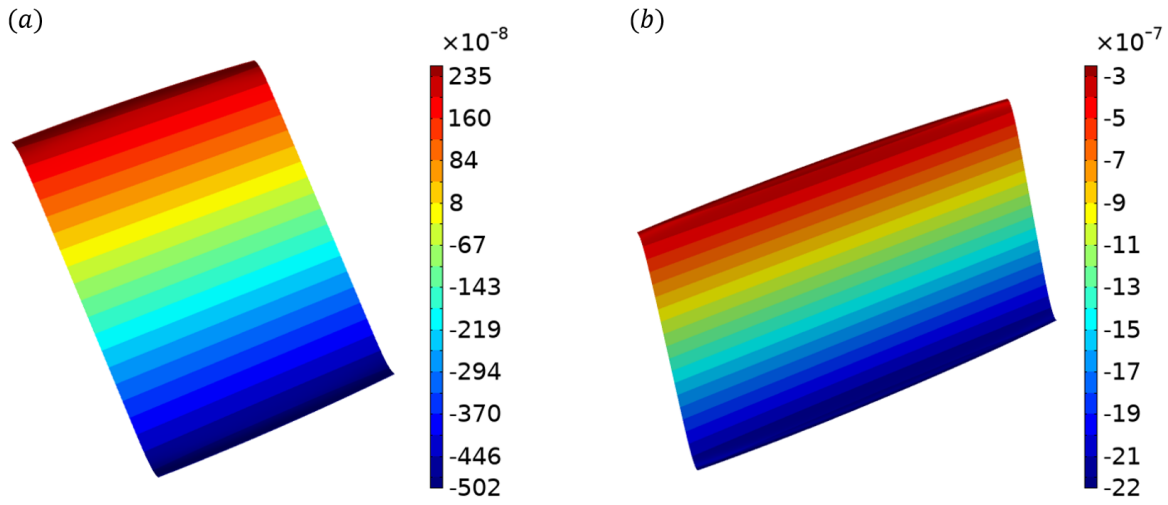

Figure 6.11: Upstream and downstream electric potential for case $Ha = 1000$, $Re = 210, \theta = 45°$.

"M-shaped" with high velocity near-wall jets at the manifold top and bottom and a velocity deficit region in the central part of the cross-section. In this part, the velocity is negative due to the formation of a recirculation zone ("recirculation flow bubble"), which consists of a pair of two symmetric counter-rotating standing vortices as seen in Figure 6.12(c). The vortices occupy the entire expansion region and even extend downstream of it. The associated electric current distribution in the expansion region is 3D with the dominant axial current component, shown in Figure 6.12(d). The pressure distribution along the duct axis in Figure 6.12(e) is linear with the axial distance over the small and big ducts where the flow is about fully developed. There are significant non-linear changes in the pressure within the expansion region, including an abrupt pressure drop at the exit of the small duct and a pressure recovery zone downstream. As seen from this figure, the most significant pressure drop occurs in the expansion region. The associated 3D MHD pressure drop ΔP_{3D} is defined at the middle of the expansion region as also shown in Figure 6.12(e). This definition of the ΔP_{3D} is used throughout the paper for all computed cases. These observations of the flow are consistent with all previous studies of MHD flows in the expansion region,

including [42, 44, 45, 56, 50].

The more detailed illustration of the 3D electric currents phenomenon is shown in Figure 6.13. During the expansion, the electric potential distribution changes, which causes the electric currents to flow in the axial direction. For 2D electric currents, the circuit closes in the cross sectional area of the duct, while for 3D electric currents, the circuit exists in the bulk fluid and the induced Lorentz force in the direction perpendicular to the magnetic field will push the flow to the side layers, therefore shaping the velocity as the profile shown in Figure 6.12(c).

Figure 6.14 shows the pressure contour and streamlines in the side layer, where $z = a - \frac{a}{2\sqrt{Ha}}$. Similar to the sudden expansion case, the flow right after the expansion will exhibit different behaviors. Here we define two critical lines, x_1 and x_2 to help understand the flow in the side layer. The flow to the left of x_1 flows into the expansion wall, the flow between x_1 and x_2 enters the Hartmann wall and the flow to the right of x_2 stays in the core flow region. This indicates that due to the distribution of pressure and Lorentz force, the flow will be separated and redistributed in the side layer, especially when the majority of flow in the expansion region enters the side layers. The electric currents and Lorentz force z component $(\mathbf{J} \times \mathbf{B})_z$ contour in the side layers are plotted in Figure 6.15. In the small duct near expansion, the electric currents are still 2D, and are restricted in the cross-sectional area. Near the expansion, the currents become 3D and have both negative and positive x components. Such a current path will lead to a Lorentz force in the $+y$ direction in the middle of the expansion region and $-y$ direction near the wall. This helps explain the observation that the pressure is higher in the center flow and lower near the wall.

Figure 6.16 takes a closer look at the z component of Lorentz force in the side layer. Here, we can conclude that near the expansion where geometry changes, the Lorentz force induced by axial currents reaches a maximum value, and then decreases further downstream. The uneven distribution across the duct is caused by the difference in the magnitude of the axial current, and thus driving the flow upwards or downwards in the y direction.

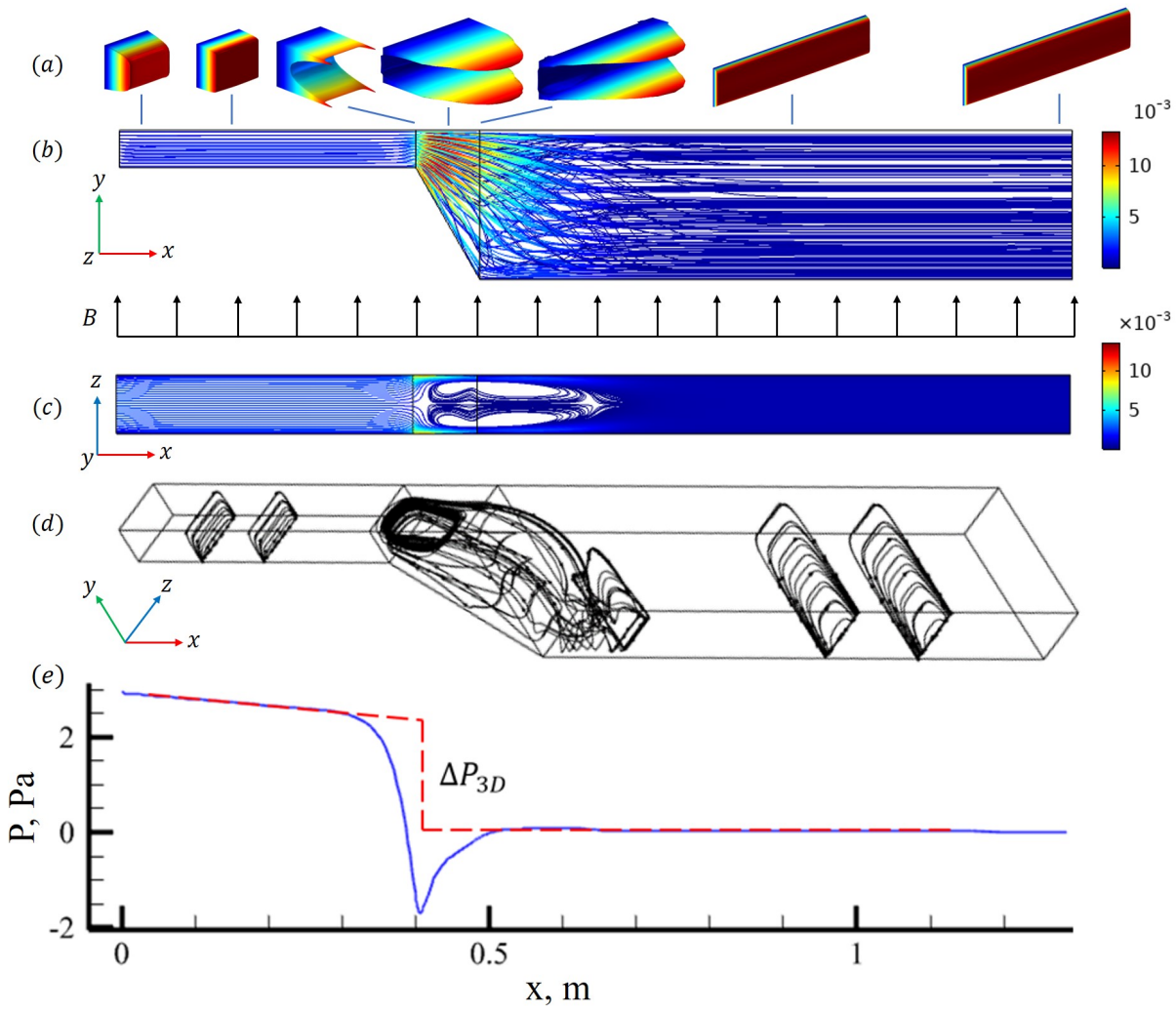

Figure 6.12: Characterization of the MHD flow in a gradual expansion at $Ha = 5000$, $Re = 1000$, $\theta = 60°$. (a) 2D velocity profiles (axial velocity component u) at several axial locations. (b) 3D velocity streamlines in the xy direction parallel to the magnetic field. (c) 3D velocity streamlines in the xz direciton perpendicular to the magnetic field. (d) 2D/3D streamlines of the induced electric current. (e) 1D pressure distribution along the duct centerline showing the definition of ΔP_{3D}.

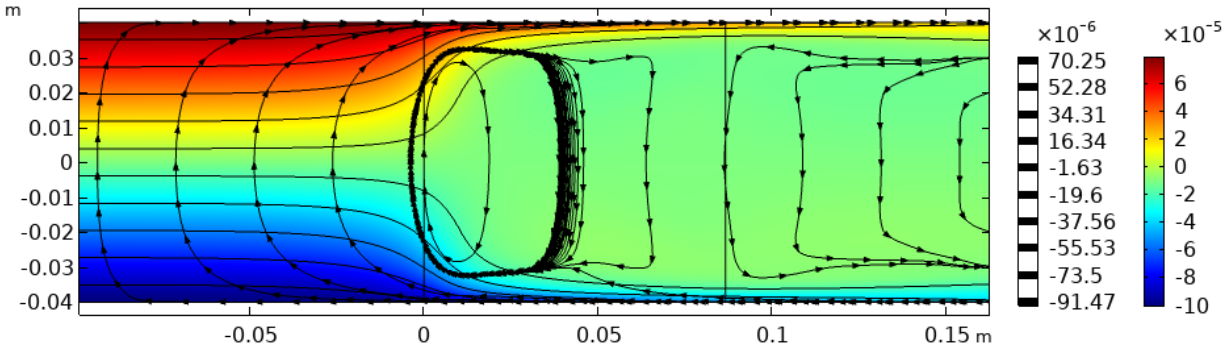

Figure 6.13: Electric current streamlines and electric potential contours in the center xz plane for $Ha = 5000, Re = 1000, \theta = 60°$.

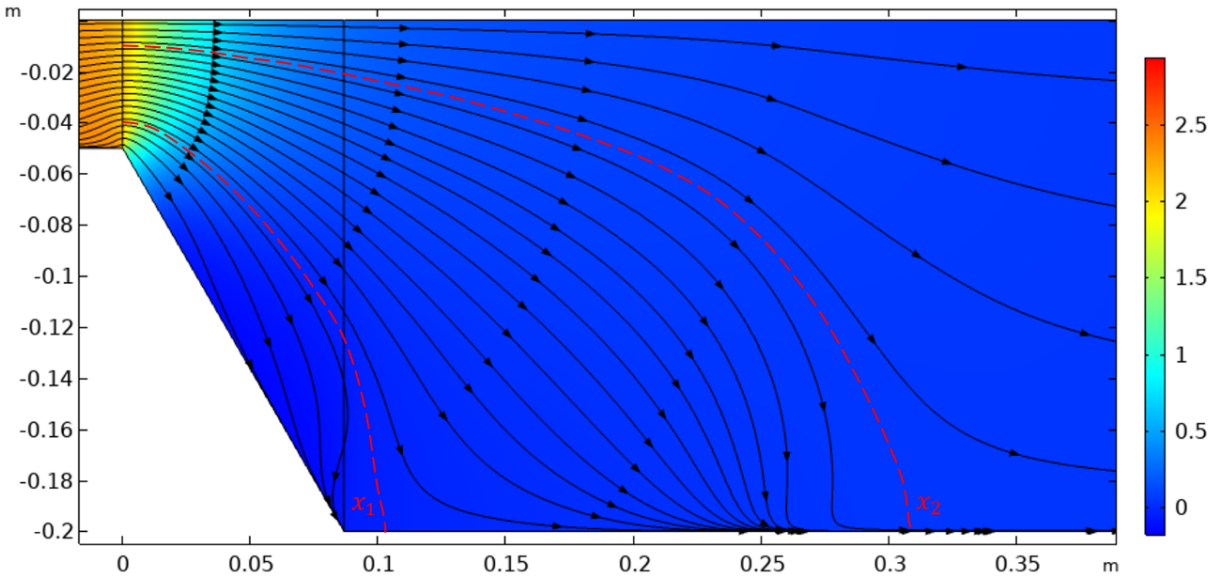

Figure 6.14: Pressure contour and streamlines in the side layer xy plane at $z = a - \frac{a}{2\sqrt{Ha}}$ for $Ha = 5000, Re = 1000, \theta = 60°$.

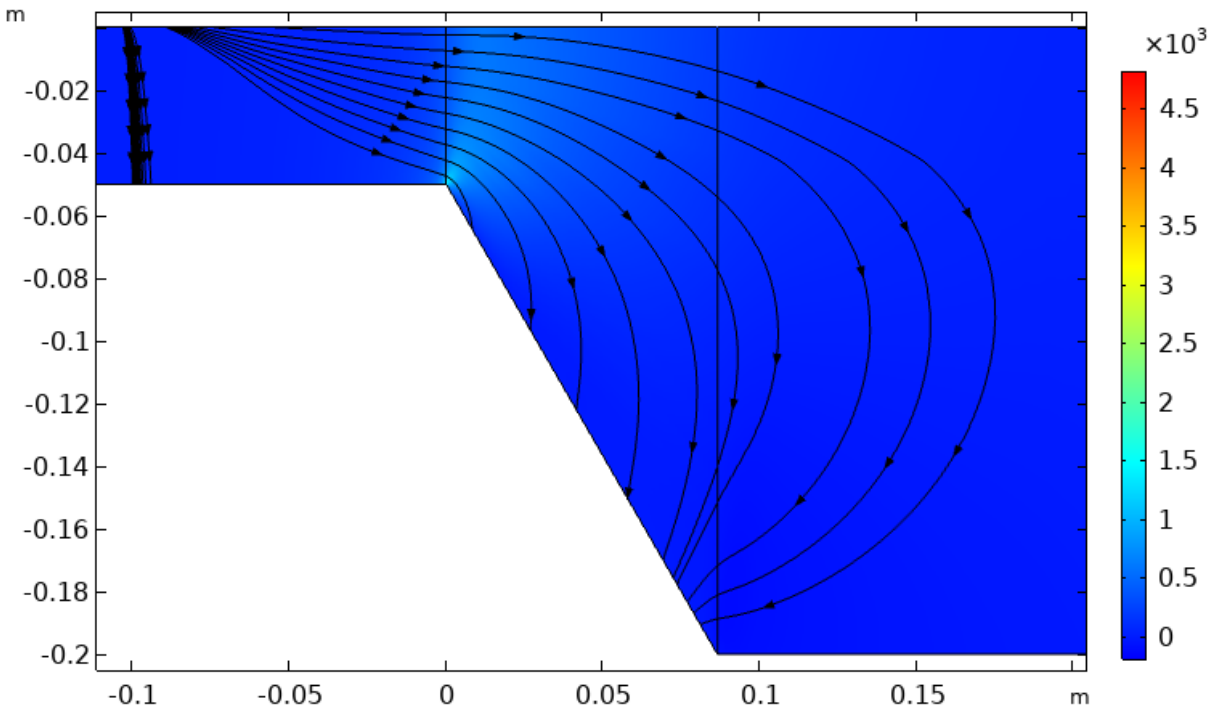

Figure 6.15: Electric currents and z direction Lorentz force in the side layer at $z = a - \frac{a}{2\sqrt{Ha}}$ for $Ha = 5000, Re = 1000, \theta = 60°$.

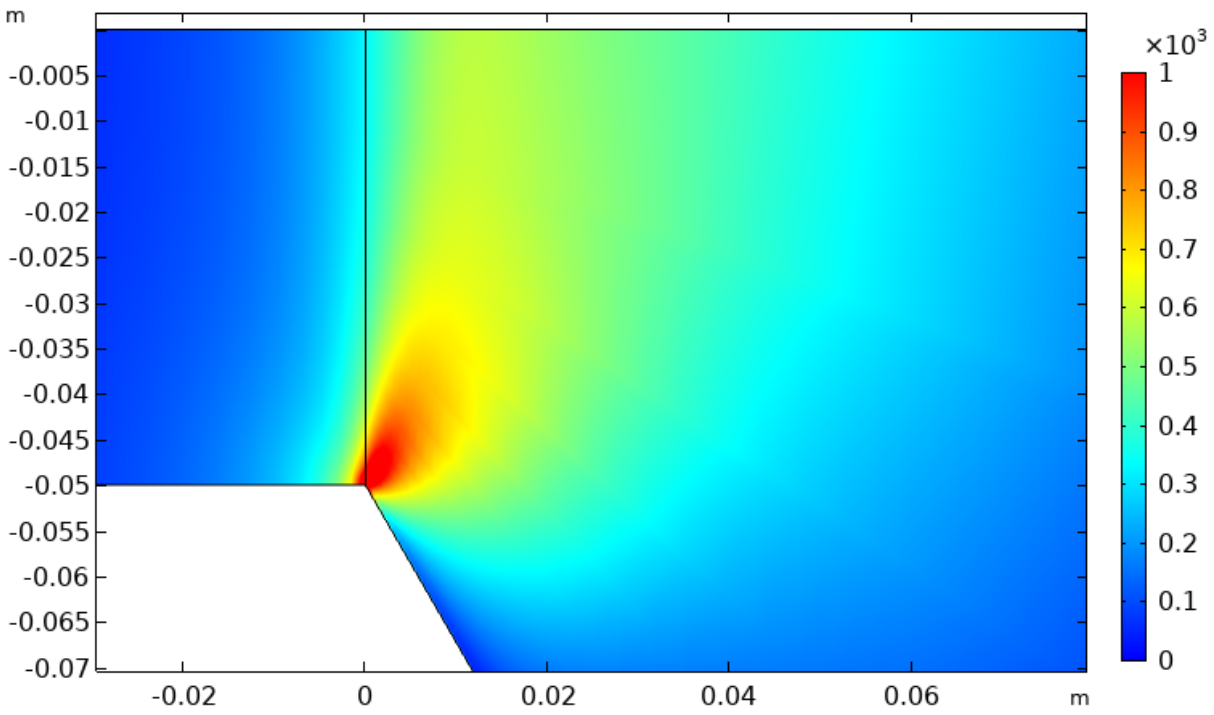

Figure 6.16: A more detailed contour of z direction Lorentz force in the side layer at $z = a - \frac{a}{2\sqrt{Ha}}$ for $Ha = 5000, Re = 1000, \theta = 60°$.

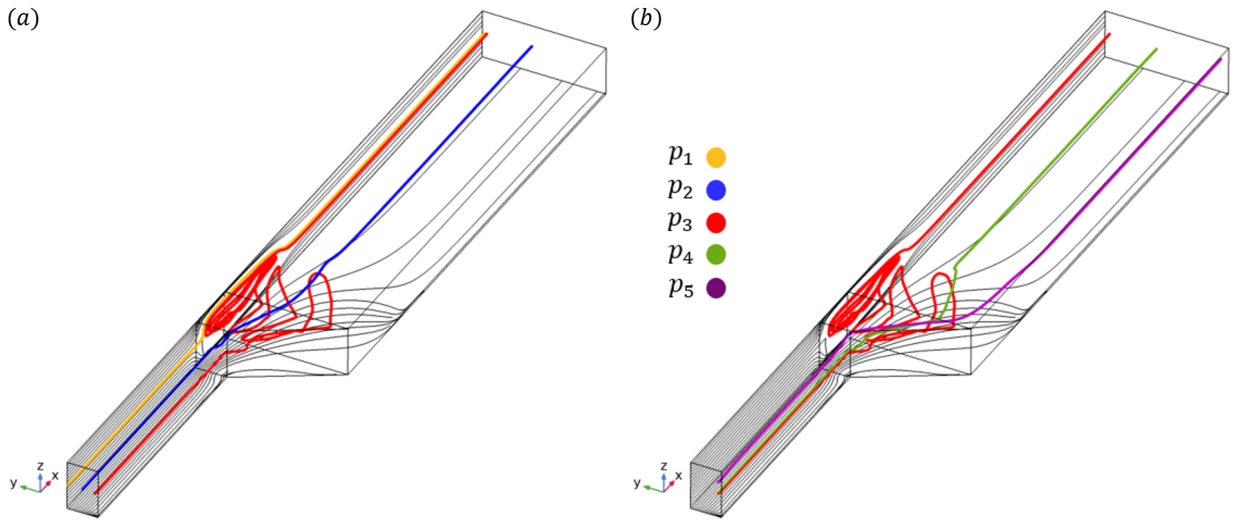

Figure 6.17: Five different particle paths in the manifold flow for $Ha = 5000, Re = 1000, \theta = 60°$.

Figure 6.17 shows the five different particle paths in the manifold. The left figure (Figure 6.17(a)) is three different paths in the y direction. Near the center of the duct ($y = 0, z = 0$), the fluid particle p_1 will go straight through the expansion area in y direction, but will change its path into the side layer due to the Lorentz forces. The particle p_2 entering near ($y = -\frac{d}{2}, z = 0$) will be diverted in the larger duct and eventually exit through the outer side of the duct. Close to the Hartmann wall, the particle p_3 will go straight along the wall in the small duct, involved in the vortex in the expansion region and eventually exit through the center of the duct. This phenomenon is caused by the difference of pressure (outer side has lower velocity and higher static pressure, downstream has higher pressure than upstream), the Lorentz force has a component in $+z$ direction, so the particle is pushed upwards and form a stationary vortex in the middle across the expansion region and also in the large duct. The right figure (Figure 6.17(b)) shows the different paths in the z direction near the wall. Particle p_4 enters the small duct in a position near the Hartmann wall and in the $+z$ region. It shows a path similar to p_2 by flowing in the expansion direction and then exit the duct through straight line in the large duct. Particle p_5 represents the flow in the corner of the duct. It goes through the small duct in the boundary layers and then continues its path in the boundary layers of the expansion region as well as the large duct. The viscous force in the boundary layer helps keep the flow in this region consistent and not entering the main flow during expansion or the core flow with vortices. Overall, the flow downstream after expansion quickly turns into fully developed state due to the Lorentz force balancing the pressure, and creating a 2D MHD flow pattern. The main flow changes happen in the expansion region with particles moving from the side to the middle of the duct through vortices, middle to outer middle through expansion and side to side due to viscous force.

6.5 3D MHD pressure drop

As mentioned before, the 3D MHD pressure drop can be expressed by $\Delta P_{3D} = k \times \frac{\rho U^2}{2}$, where k is the 3D pressure drop coefficient. For each expansion angle, the pressure drop coefficient was calculated by extending the fully developed pressure curve upstream and downstream to intersect with the expansion region center position, and subtracting the values of two points. The calculated values for k for different angles are shown in Table 6.5, 6.6 and 6.7.

Table 6.5: Pressure drop coefficient k for expansion angle 45°

Re/Ha	1000	3000	5000	7000	10000
50	1.380E+03	8.097E+03	1.760E+04	2.915E+04	4.912E+04
100	7.060E+02	4.124E+03	8.872E+03	1.463E+04	2.438E+04
200	3.644E+02	2.122E+03	4.544E+03	7.053E+03	1.165E+04
400	1.914E+02	1.111E+03	2.347E+03	3.699E+03	6.132E+03
600	1.312E+02	7.673E+02	1.612E+03	2.590E+03	4.293E+03
1000	8.000E+01	4.893E+02	1.042E+03	1.723E+03	2.375E+03
2000	3.768E+01	2.714E+02	5.866E+02	9.720E+02	1.458E+03
3000	2.180E+01	1.925E+02	4.169E+02	6.967E+02	1.060E+03
5000	7.794E+00	1.242E+02	2.833E+02	4.921E+02	7.057E+02
10000		9.566E+01	1.702E+02	2.847E+02	4.501E+02

6.5.1 Effect of expansion angle θ, Ha and Re

Characterizing the effect of the expansion angle is one of the key outcome of this study as adjustments of this parameter can result in optimized manifold designs with a lower MHD pressure drop and a more uniform flow distribution at the exit of the manifold. The manifold with gradual expansion can reduce the 3D MHD pressure drop across the expansion region compared to sudden expansion geometry. Two cases with different Hartmann numbers are

Table 6.6: Pressure drop coefficient k for expansion angle 60°

Re/Ha	1000	3000	5000	7000	10000
50	1.637E+03	9.207E+03	2.137E+04	3.394E+04	5.769E+04
100	8.322E+02	4.692E+03	1.048E+04	1.780E+04	2.987E+04
200	4.463E+02	2.444E+03	5.349E+03	8.808E+03	1.462E+04
400	2.394E+02	1.318E+03	2.834E+03	4.671E+03	7.846E+03
600	1.659E+02	9.392E+02	1.992E+03	3.316E+03	5.489E+03
1000	1.056E+02	6.144E+02	1.299E+03	2.135E+03	3.587E+03
2000	5.444E+01	3.280E+02	7.340E+02	1.239E+03	2.079E+03
3000	3.548E+01	2.319E+02	5.530E+02	8.862E+02	1.522E+03
5000	1.688E+01	1.561E+02	3.772E+02	5.958E+02	1.026E+03
10000			2.137E+02	3.430E+02	6.159E+02

Table 6.7: Pressure drop coefficient k for expansion angle 75°

Re/Ha	1000	3000	5000	7000	10000
50	1.913E+03	1.037E+04	2.357E+04	3.960E+04	6.826E+04
100	1.001E+03	5.409E+03	1.167E+04	2.012E+04	3.480E+04
200	5.307E+02	2.858E+03	6.124E+03	1.042E+04	1.776E+04
400	2.889E+02	1.563E+03	3.400E+03	5.667E+03	9.608E+03
600	2.036E+02	1.126E+03	2.383E+03	4.055E+03	6.838E+03
1000	1.302E+02	7.342E+02	1.584E+03	2.635E+03	4.426E+03
2000	6.935E+01	4.277E+02	9.151E+02	1.519E+03	2.556E+03
3000	4.686E+01	3.098E+02	6.637E+02	1.101E+03	1.794E+03
5000	2.611E+01	2.057E+02	4.568E+02	7.307E+02	1.273E+03
10000		1.109E+02	2.670E+02	4.401E+02	

computed: $Ha = 1000, 5000$. The results derived from definition of ΔP_{3D} are shown in Figure 6.18. As can be clearly seen from the figure, the coefficient for pressure drop is reduced by approximately 30% when switching from sudden expansion geometry to a more gradual one.

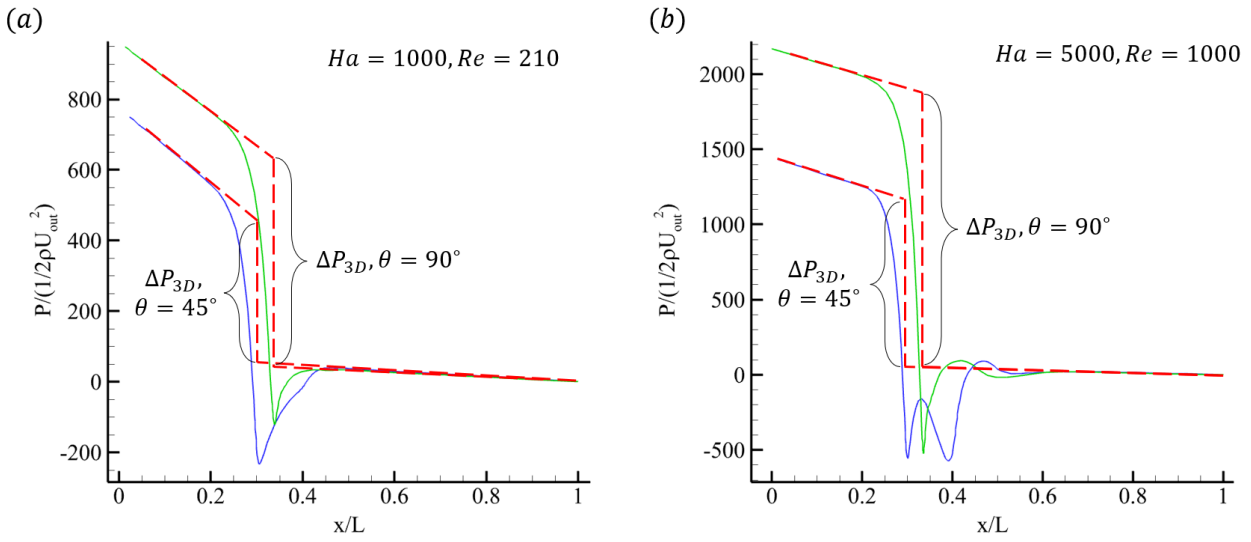

Figure 6.18: Comparison of 3D pressure drop across expansion region between sudden and gradual expansion manifolds.

The pressure distributions along the duct center axis for three selected angles are shown in Figure 6.19. It confirms that smaller expansion angles would result in a significant reduction of the manifold pressure drop coefficient. This trend of reducing the 3D MHD pressure drop at smaller expansion angles persists at all other Ha and Re computed in this study. The effect of the Reynolds number Re and Hartmann number Ha on pressure drop coefficient k is shown in Figure 6.20 for $1000 < Ha < 10,000$ and $50 < Ha < 10,000$. For all Ha numbers, the pressure drop coefficient decreases as Re increases but the most significant changes in k occur at lower $Re < 1000$. The increase of Ha always results in higher k as seen in Figure 6.20. However, this effect is more pronounced at lower Re.

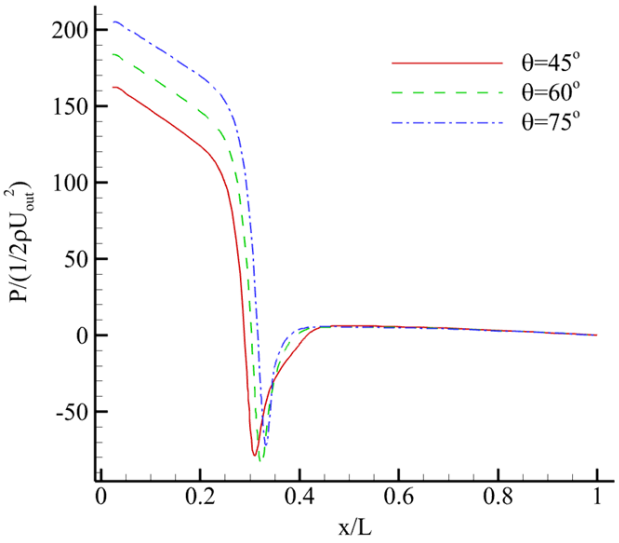

Figure 6.19: Effect of expansion angle on the pressure distribution along the center axis.

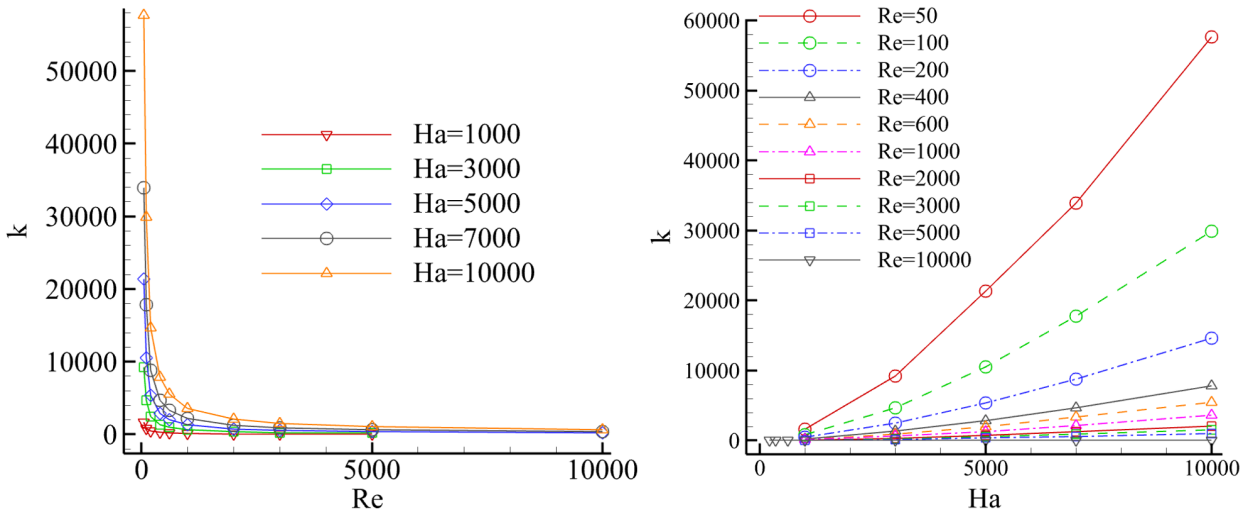

Figure 6.20: Effect of Ha and Re. Pressure drop coefficient k (a) as a function of Re and (b) as a function of Ha.

6.5.2 Construction of correlation

As stated in Chapter 1, the main goal of the manifold study is to deduce accurate 3D MHD pressure drop correlations based on all 150 cases computed. In the initial effort to develop a correlation for k, we attempted to use the parameters suggested in the 2D Ludford layer theory for MHD flows with abrupt changes in the duct geometry that occur in the plane parallel to the applied magnetic field [30]. This theory attributes high MHD pressure drop to the formation of a thin internal MHD shear boundary layer located near the sudden geometry change.

The asymptotic analysis of Ludford layers (see e.g. [78]) suggests the existence of essentially three possible flow regimes depending on the force balance inside the Ludford layer. The viscouselectromagnetic (VE) regime holds for $N \gg Ha^{\frac{3}{2}}$, and the inertial-electromagnetic (IE) regime for $N \ll Ha^{\frac{3}{2}}$. A third regime where all three forces might be important is the inertial-viscouselectromagnetic (IVE) regime that holds for $N \sim Ha^{\frac{3}{2}}$. In accordance with the Ludford layer theory, the pressure drop coefficient scales as $NHa^{-\frac{1}{2}}$ in the VE regime and as $N^{\frac{2}{3}}$in the IE regime. The earlier analysis and the developed correlations for k in the MHD flow with a sudden expansion ($\theta = 90°$) in [4, 56] suggest two regimes, resembling VE and IE regimes in the Ludford layer theory, with the transition threshold at $Ha^{\frac{3}{2}}$. The same two regimes were initially sought in our studies for $\theta = 45°, 60°$ and $75°$. However, the analysis of the 150 computed cases has not clearly confirmed the existence of these two regimes. In fact, the best fit for all computed cases was found using $NHa^{-\frac{1}{2}}$, which in the Ludford layer theory represents the VE regime. This departure from the classical Ludford layer theory can be attributed to its limitations compared to the full computations. Namely, the present computations indicate various 3D flow features, whereas the Ludford layer theory is 2D. Moreover, the Ludford layer theory cannot predict the formation of a recirculation flow bubble as seen in the present studies, which is an important flow characteristic with a significant impact on the pressure drop.

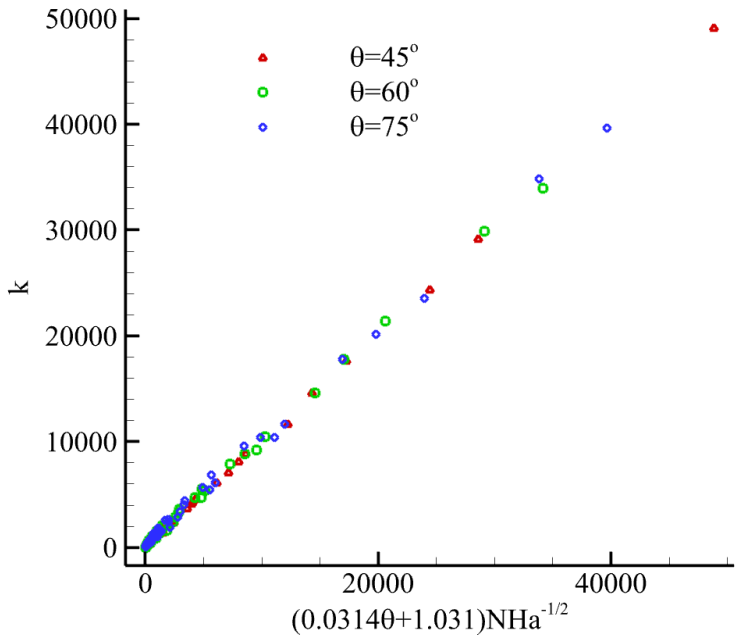

Figure 6.21: Best fit for the obtained data for the 3D MHD pressure drop coefficient k for different expansion angles, based on the 150 computed cases.

The linear regression analysis that incorporated all computed data point for three expansion angles suggests the following correlation:

$$k = (0.0314\theta + 1.031) \cdot NHa^{-\frac{1}{2}} \tag{6.1}$$

where θ is in degree. The high accuracy of this fitting formula is illustrated in Figure 6.21 that suggests the R-squared parameter R^2 at 0.9992, which is very close to unity, meaning that the proposed linear regression function in Eq. 6.1 fits the computed data very well. To compare, R^2 in the proposed correlations for the flow with sudden expansion [4] is close but slightly lower: 0.9989 in the VE regime and 0.9980 in the IE regime.

6.6 Recirculation and flow development length

Apart from the MHD pressure drop, the flow field in the manifold requires a special consideration. In the blanket developments, the optimal manifold design should provide a uniform

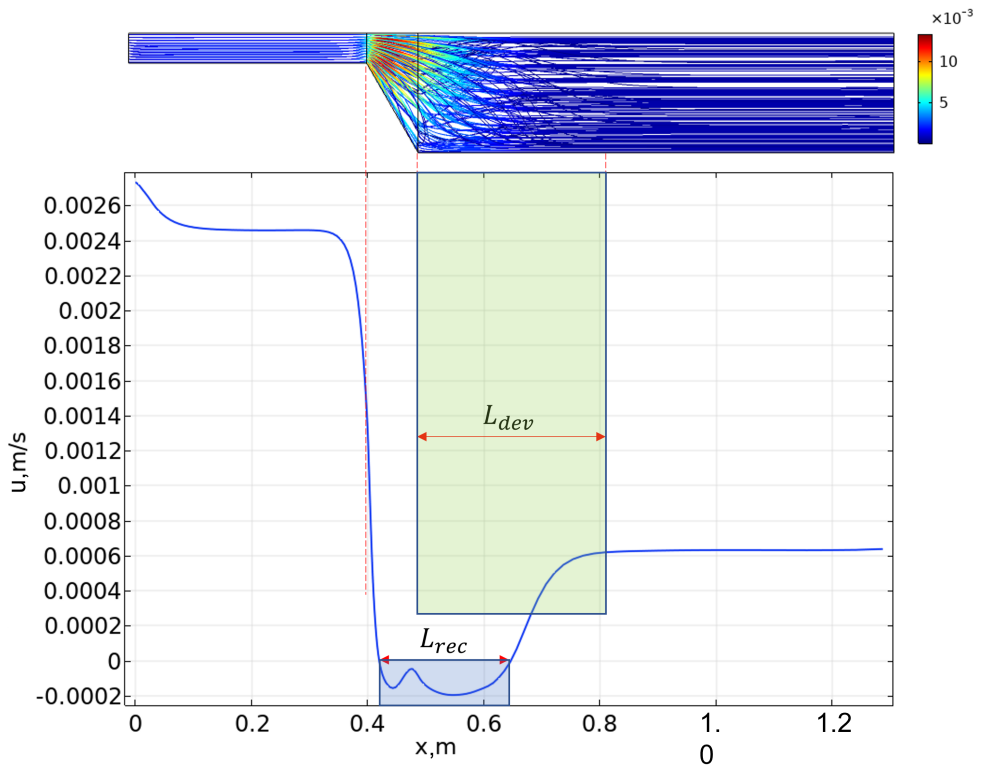

Figure 6.22: To the definition of the recirculation length L_{rec} and the flow development length L_{dev}. Velocity distribution and flow streamlines are shown for $Ha = 5000$, $Re = 1000$, $\theta = 60°$.

flow distribution at the exit of the big duct to guarantee that all poloidal channels are equally fed. Therefore, it is important to make sure that the big duct is long enough so that a uniform fully developed flow can be formed before the liquid turns to flow poloidally. In practice, this requirement cannot be easily met because of the limited available space at the bottom of the vacuum chamber of a fusion reactor where the manifolds are usually placed. The two related flow characteristics that need to be assessed are the flow recirculation length L_{rec} and the flow development length L_{dev} as shown in Figure 6.22.

Here, L_{rec} is defined as a length over which the axial velocity component at the duct axis is negative. The negative axial velocity indicates the formation of the two symmetric vortical

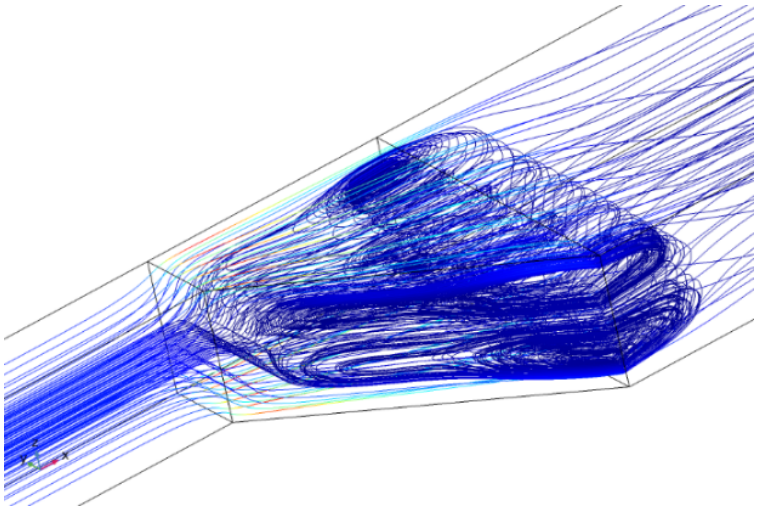

Figure 6.23: A recirculation flow bubble in the expansion region at $Ha = 1000, Re = 1000, \theta = 45°$. 3D flow streamlines are shown.

structures stretched in the flow direction as shown in Figure 6.12(c), which we also refer to as a "recirculation flow bubble". The other parameter, L_{dev}, is a length of the duct section located downstream of the expansion zone where the flow develops to the fully established one. Both L_{rec} and L_{dev} are strongly affected by Re and Ha and depend on θ.

The recirculation flow bubble is shown in Figure 6.23, where the 3D flow streamlines are plotted inside the expansion region and the two short adjacent duct sections upstream and downstream. As seen in this figure, at relatively low Re, the recirculation flow bubble is slightly bigger than the expansion section. The effect of the Ha number on the recirculation flow is illustrated in Figure 6.24, where 2D flow streamlines are plotted in the duct midplane $y = 0$. The figure shows that the recirculation flow bubble becomes less stretched in the flow direction and moves closer to the entrance of the expansion region as the Ha number increases. When Ha is increased from 1000 to 10,000 the recirculation flow length becomes roughly two times shorter.

The effect of Re on the recirculation flow is more complicated as shown in Figure 6.25. At the lowest Re of 50, the recirculation flow bubble is almost all localized within the expan-

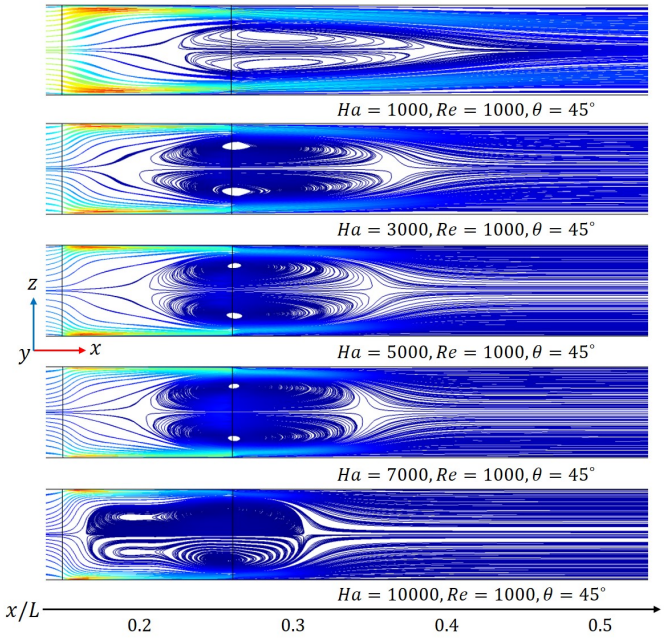

Figure 6.24: Effect of Ha on the recirculation flow at $Re = 1000, \theta = 60°$. 3D streamlines are plotted in the xz direction.

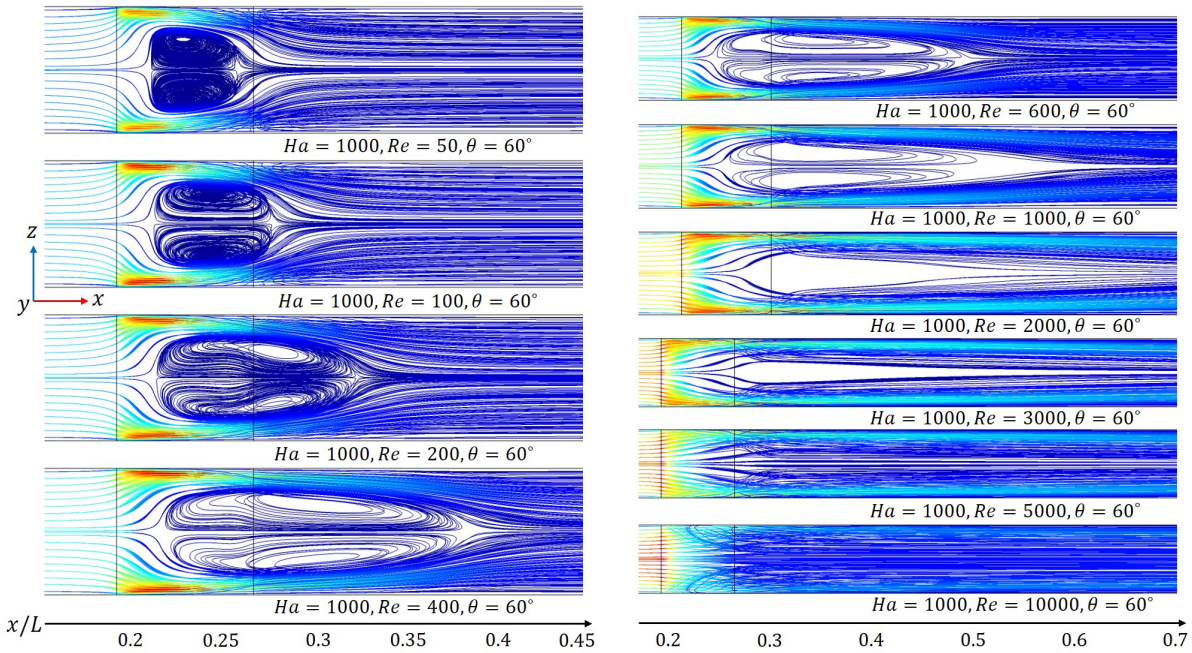

Figure 6.25: Effect of Re on the recirculation flow bubble for $Ha = 1000, \theta = 60°$.

sion region. At higher Re ($100 < Re < 3000$) it stretches further downstream outside the expansion region reaching several sizes of the expansion region. If Re further increases, the recirculation bubble disappears as seen in Figure 6.25 for $Re = 5000$ and $Re = 10,000$. This phenomenon can be explained by the fact that when Re is high enough compared to Ha, the flow is closer to hydrodynamic state with Lorentz forces stabilizing it. Typical hydrodynamics flow in a gradual expansion duct will not form recirculation structure naturally. When Ha is relatively high, the flow obstructing electromagnetic force will push the flow to the boundary layers, thus resulting in a recirculation zone in the bulk flow. Figure 6.26 shows the effect of the expansion angle θ, which manifests in more stretching the recirculation flow bubble in the flow direction and moving it closer to the entrance of the expansion region as θ is increased.

The computed L_{rec} and L_{dev} for all 150 flow cases are summarized in Figure 6.27 and Figure 6.28. In these figures, the two lengths are scaled using the size of the expansion region L_{exp}, which seems to be a relevant length scale for this problem (not counting the case of

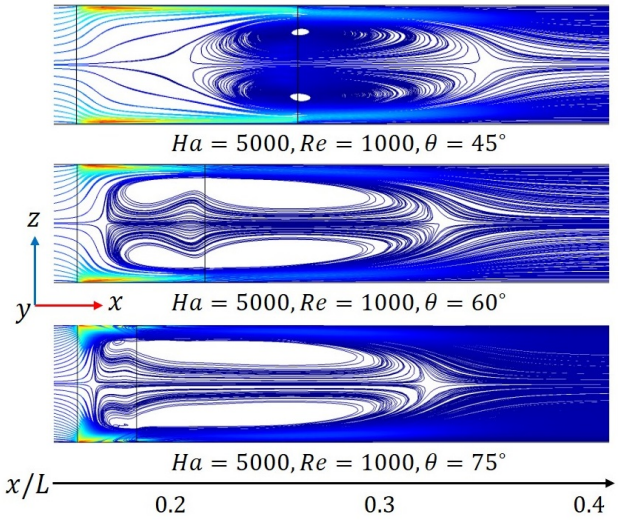

Figure 6.26: Effect of the expansion angle on the recirculation flow bubble at $Ha = 5000, Re = 1000$. The two vertical lines show the location of the expansion region.

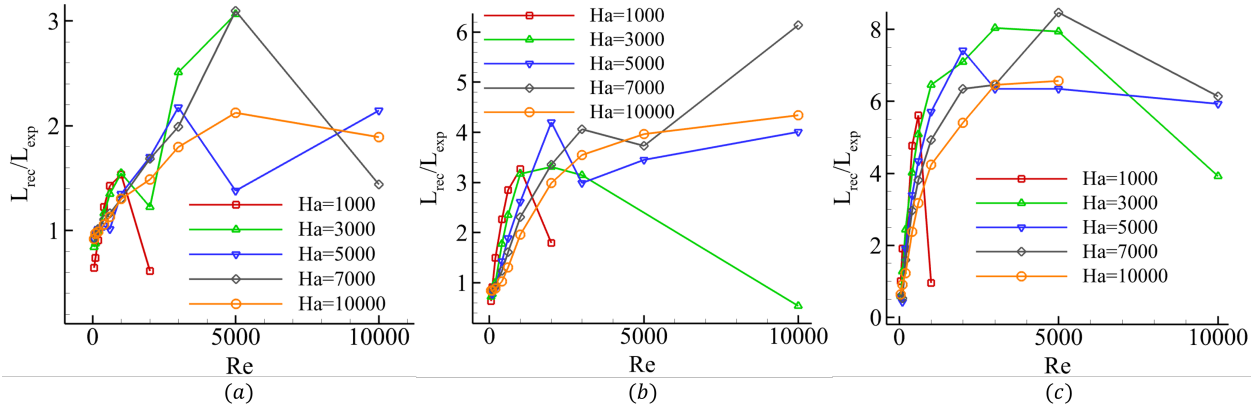

Figure 6.27: Effect of Re and Ha on the recirculation flow length: (a) $\theta = 45°$, (b) $\theta = 60°$, and (c) $\theta = 75°$.

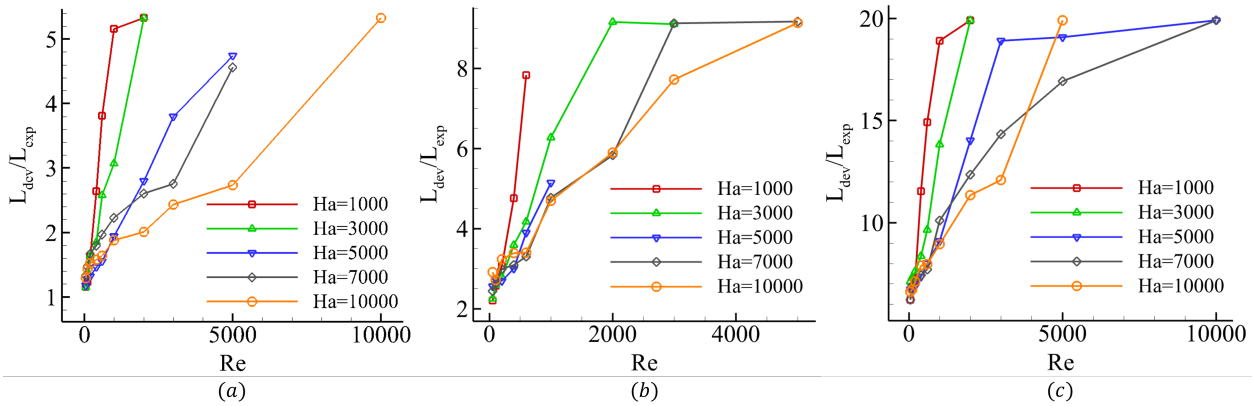

Figure 6.28: Effect of Re and Ha on the flow development length: (a) $\theta = 45°$, (b) $\theta = 60°$, and (c) $\theta = 75°$.

$\theta = 90°$ where $L_{exp} = 0$). The general trend in the changes of L_{rec} for all computed expansion angles is the fast increase with Re for $Re < 5000$ followed by its saturation for $Re \sim 5000$. At higher Re, the recirculation flow bubble has not been identified for almost all Ha and θ as appears to be a consequence of a strong inertia impact on the flow. The flow development length increases almost linearly with Re for the majority of the computed cases. The slope of the line $\frac{L_{rec}}{L_{exp}}$ as a function of Re depends on the Hartmann number. Higher slopes are seen at lower Ha. This suggests the trend of reducing the flow development length in a stronger magnetic field. Typically, the flow development length is significantly higher than the size of the recirculation bubble. The highest $\frac{L_{rec}}{L_{exp}}$ of 20 was observed in the case of the most abrupt expansion of $\theta = 75°$, while the maximal $\frac{L_{rec}}{L_{exp}}$ is 9 at $Re = 5000$ for the same expansion angle.

6.7 Importance of inertia forces

In the first analyses of MHD flows with sudden changes of the duct geometry that occur in the plane parallel to the applied magnetic field, the computational model was limited to the so-called inertialess approximation. In this approach, following the order of magnitude

analysis at high Hartmann numbers, the inertia forces are neglected in the entire flow domain. In doing so, the flow can be subdivided into an inviscid core, where strong electromagnetic forces are balanced by pressure gradients, and thin viscous boundary layers, including near-wall (Hartmann and side layers) and internal shear layers, e.g. the Ludford layer. In [42], a special term "expansion layer" was coined to emphasize differences between the 2D Ludford layer and the actual internal boundary layer that forms in the 3D expansion region near the abrupt change in the flow geometry. The role of inertia forces was further investigated in the consequent studies (see e.g. [44]). Strong inertia effects that manifest themselves through the velocity distribution, pressure and electric currents were found as the Reynolds number increases or/and the Hartmann number decreases.

In the present study of MHD flows in ducts with a gradual expansion, the important role of the inertia forces was also found for almost all computed cases except for several cases at lower Re (typically, $Re < 1000$). In Figure 6.29, all forces acting on the flow are plotted along the duct axis, i.e. within the core flow region. It is clearly seen that the inertia and viscous forces here are negligibly small, while the electromagnetic forces are balanced by the pressure gradient. The effect of inertia forces, which are localized within the thin internal boundary layer at the entrance to the expansion region are illustrated in this study by comparing the full computations where all forces are retained with the computations based on a reduced flow model, where the convective terms in the momentum equation are dropped. The reduced flow model can easily be chosen in COMSOL without any programming. In fact, the full computations were performed first and then the inertialess computations were run using the results from the full model as an initial condition to reduce the computational time. Although the inertia forces are confined in the thin boundary layer, their effect is global, i.e. significant changes can be seen in the integral flow characteristics, such as the overall pressure drop and the size of the recirculation zone. The comparisons are made in Figure 6.30 for the MHD pressure drop and in Figure 6.31 for the recirculation flow.

For a very small flow velocity ($Re = 100$) and high Ha of 5000 the difference in the

pressure drop between the two models is only 3% (Figure 6.30(a)). This suggests that for such a low Re, the flow is inertialess. If Re increases, the discrepancy increases dramatically, showing a difference of 16% at $Re = 1000$ (Figure 6.30(b)) and 40% at $Re = 5000$ (Figure 6.30(c)). This obviously emphasizes a strong inertia effect. Similar trends showing higher pressure drops computed with the full model can be seen at other Ha and expansion angles. The 3D flow streamlines computed with the two models are compared in Figure 6.31. Both Ha and Re in this comparison are high ($Ha = 5000$, and $Re = 5000$) so that the differences between the two models are more distinctive. When the inertialess flow model is used, the recirculation flow bubble is confined to the expansion region, and the flow upstream and downstream of the bubble is fully developed. When using the full flow model with the inertia forces, the recirculation flow extends over the downstream duct. The flow development length being significantly higher than the length of the expansion region is clearly seen. All these observations do confirm that under the real blanket conditions where both Ha and Re can be significantly higher compared to the parameters in the present study, using the full flow model is mandatory. Using the inertialess flow model will significantly underestimate the MHD pressure drop.

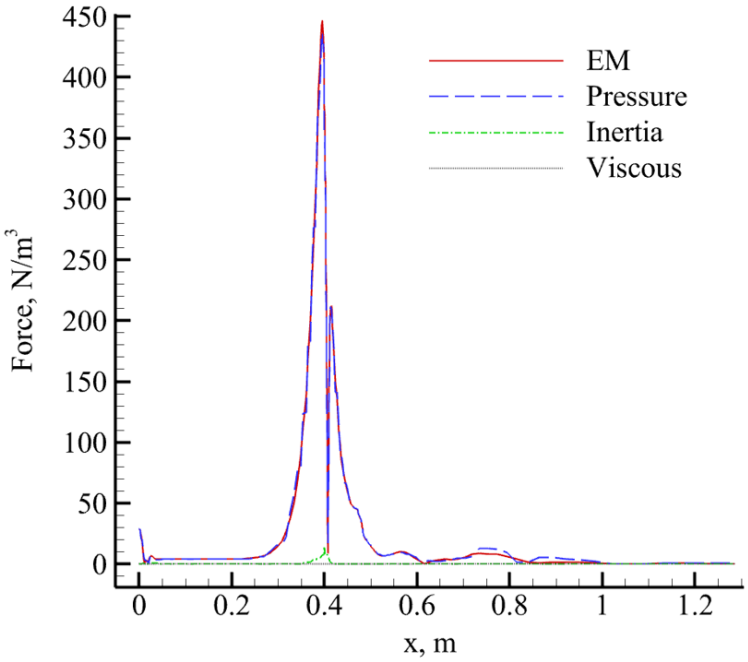

Figure 6.29: Force balance in the core flow at $Ha = 5000, Re = 3000, \theta = 60°$. The forces are plotted along the duct axis.

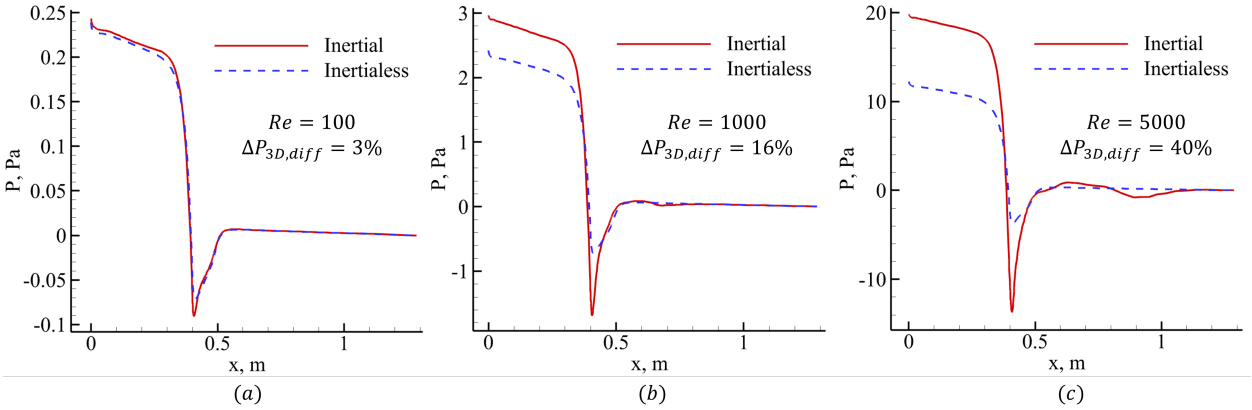

Figure 6.30: Effect of inertia forces on the pressure distribution for $Ha = 5000, \theta = 60°$ for different Re.

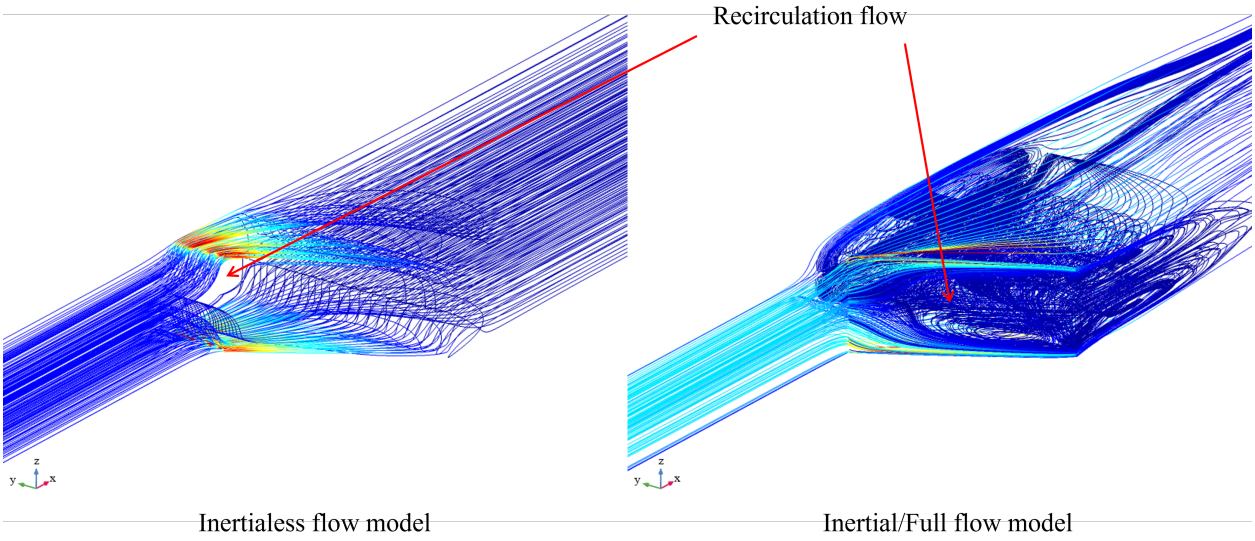

Figure 6.31: Recirculation flow bubble in 3D computed with and without inertia forces for $Ha = 5000, Re = 5000, \theta = 60°$.

CHAPTER 7

MHD flow in a supply duct (flow in a fringing magnetic field)

7.1 Mathematical formulation of the problem

The sketch showing a MHD flow in the rectangular access duct under the influence of fringing magnetic field is shown in Figure. 7.1. The outlet of the access duct was selected to avoid turbulent hydrodynamic flow under high Hartmann and Reynolds numbers. The LM flows into the access duct with width $2d$, height $2a$, and length L at the velocity U_{in}. The flow occurs in the presence of a transverse fringing magnetic field B, which has uniform regions at the beginning and end of the section, and steep change in the middle.

As shown in the figure, the cartesian coordinate system is chosen such that the LM flows in x direction, which is aligned with center axis of the duct. The magnetic field is applied in y direction. Different fringing fields with various maximum magnetic field intensity gradient $\left(\frac{dB}{dx}\right)_{max}$ are used for study and will be explained later.

The rectangular duct has a similar dimension to DCLL blanket design with $d = a = 0.0439m$. The length of the duct should meet the requirement for the flow to change from fully developed 2D MHD flow to 3D MHD flow and then hydrodynamic flow. Here the duct length $L = 30d$. The flow enters the duct under the influence of a constant magnetic field. In the middle of the duct, the magnetic field decreases suddenly. At the exit of the duct, a small constant magnetic field B_{add} is intentionally added to assure that laminar flow model could be used. The eutectic alloy $PbLi$ is used as a working fluid, and the properties including

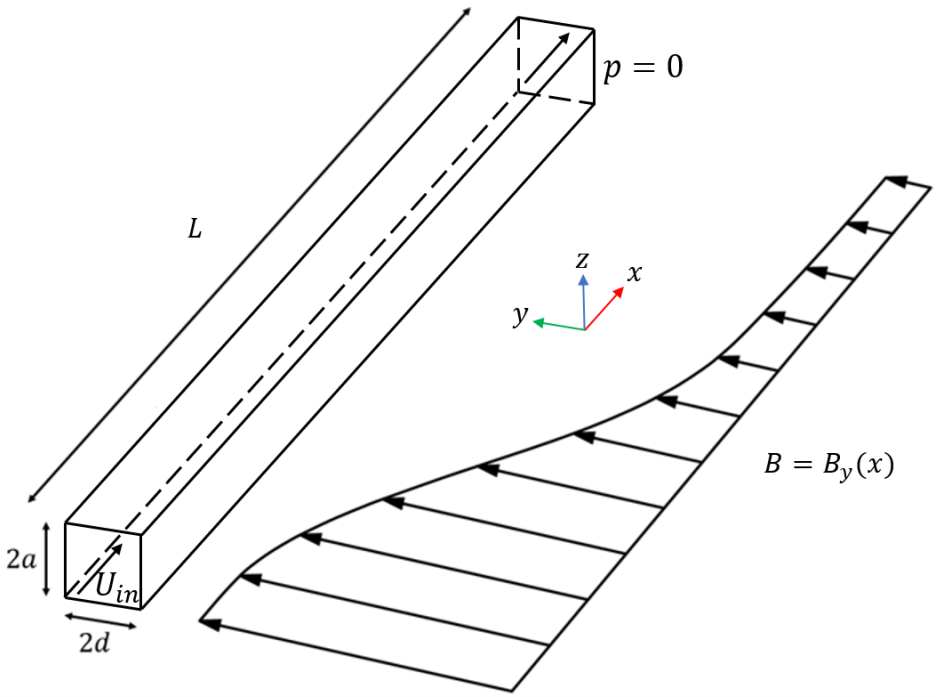

Figure 7.1: Schematic illustration of formulation of the problem.

density ρ, dynamic viscosity μ and electric conductivity σ are defined at $500°C$. In real blanket, the $PbLi$ flow is decoupled from electrically conducting walls through insulating flow channel insert. Therefore, the computations in current study are limited to the fluid flow domain. The fringing magnetic field and inlet velocity are varied to ensure the flow Hartmann and Reynolds numbers can reach 10,000.

For LM MHD flow in a fringing magnetic field, the basic equations used are the same as those in MHD duct and manifold flow for incompressible, isothermal, laminar flow written in inductionless approximation [78] which assumes that the induced magnetic field can be neglected compared to the applied one. The boundary conditions for fluid flow includes the no slip condition at the duct side walls, U_{in} as uniform inlet velocity and $p = 0$ at the outlet. Due to the insulating duct assumption, the Neumann boundary condition which enforces no electric current through the wall is applied to all the duct boundaries.

Similar to the MHD flow in a manifold, the Hartmann number Ha and Reynolds number

Re are chosen to help characterize the flow. Here, the Hartmann number is given by $Ha = B_{max} d\sqrt{\frac{\sigma}{\mu}}$ and B_{max} is the maximum magnitude of the magnetic field at the inlet of the duct. In order to help establish the correlation for 3D MHD pressure drop, which is one of the main goals of the study, another dimensionless parameter Ha^* is constructed as $Ha^* = abs\left(\left(\frac{dB}{dx}\right)_{max}\right) d^2\sqrt{\frac{\sigma}{\mu}}$.

As mentioned, the fringing magnetic field can be represented through approximation relation $B_y = B_0 \times \frac{1-\tanh[\gamma(\frac{x}{d}-c)]}{2} + B_{add}$, where $\frac{1-\tanh[\gamma(\frac{x}{d}-c)]}{2}$ is the function to simulate the distribution of real magnetic field decaying in the fringing region [61]. B_0 is the difference between the maximum and minimum intensity of the magnetic field, B_{add} is the additional magnetic field component, and c is a constant. In this formula, γ determines the maximum gradient of the magnetic field. Four different values of γ are chosen: 0.3, 0.45, 0.75 and 1. The resulting magnetic field distributions are shown in Figure 7.2. The magnetic field gradient increases with γ and the change becomes more sudden at the same time. The Ha^* is related to the absolute value of maximum magnetic field gradient, and therefore, by taking the derivative of the relation for magnetic field and finding the maximum value, the Ha^* can be expressed as $Ha^* = \frac{\gamma d}{2}\sqrt{\frac{\sigma}{\mu}}$. From this relation, Ha^* is linearly related to γ as $Ha^* = 585.02\gamma$.

Naturally, the magnetic field should meet the "curl free/divergence free" condition, or $\nabla \cdot B = 0, \nabla \times B = 0$. The magnetic field that satisfies the conditions is named as "full field" or "consistent field" [61], while the magnetic field with only one component is called "reduced field" or "inconsistent field". The reduced field has only one component and is given by $B_{red} = (0, B_y(x), 0)$ where $B_y(x)$ is defined as $B_y(x) = B_0 \times \frac{1-\tanh[\gamma(\frac{x}{d}-c)]}{2}$. The full field takes the form $B_{full} = (B_x(x,y), B_y(x,y), 0)$, and the components are related to the reduced field by

$$B_y = B_0 \times \left[B_y(x) - \frac{\partial^2 B_y(x)}{\partial x^2} \cdot \frac{y^2}{2} + \frac{\partial^4 B_y(x)}{\partial x^4} \cdot \frac{y^4}{24}\right];$$

$$B_x = B_0 \times \left[\frac{\partial B_y(x)}{\partial x} \cdot y - \frac{\partial^3 B_y(x)}{\partial x^3} \cdot \frac{y^3}{6}\right].$$

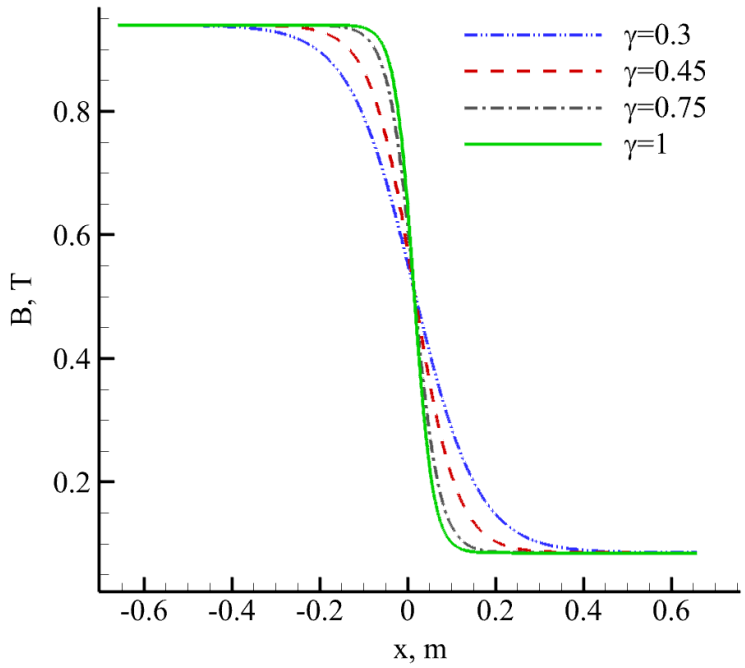

Figure 7.2: Magnetic fields used in current study with varying γ.

[61]. It depends on both x and y directions. Figure 7.6 shows the comparison of results computed by full field, reduced field and from the experiment [5]. Two pressure related characteristics are compared, the center axis pressure gradient scaled as $\frac{dP}{dx}^* = \frac{\frac{dP}{dx}}{\sigma U B^2}$ and the difference of pressure (transverse pressure difference) in Hartmann layer and side layer, which is given by $\Delta P^* = \frac{\Delta P}{\sigma d U B^2}$. The difference of pressure gradient distribution along the axial direction between reduced field and full field is quite small, and slightly different from the experiment. For the transverse pressure difference in the Hartmann layer and side layer, the relative difference of peak value between reduced field and full field is less than 10%, while the experiment gives a significantly higher value (35% difference) than the full field. Therefore, we consider that the reduced field is enough for capturing flow characteristics and generating precise 3D MHD pressure drop for measurement. The observation from the results of COMSOL is consistent with Chico [61] that the effect of other field components on the pressure drop is small.

In this study, the Ha and Re are chosen as $Ha = 1000, 2000, 3000, 5000, 10000$ and $Re =$

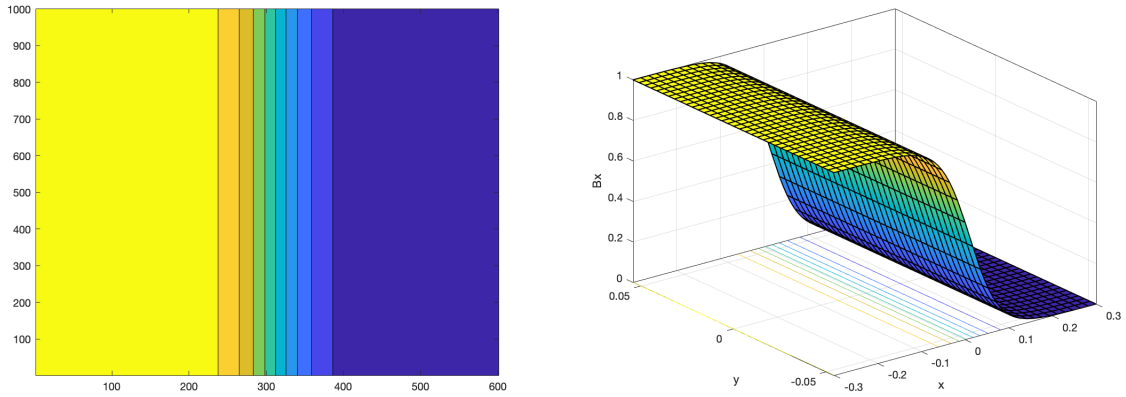

Figure 7.3: Reduced magnetic field with only y-component $B_y(x)$ in (left) 2D, (right) 3D.

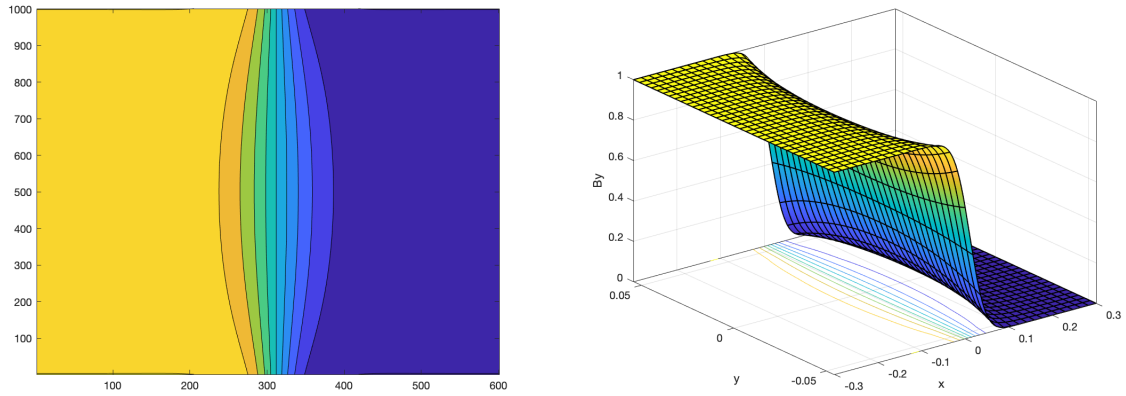

Figure 7.4: Full magnetic field $B_y(x, y)$ in (left) 2D, (right) 3D.

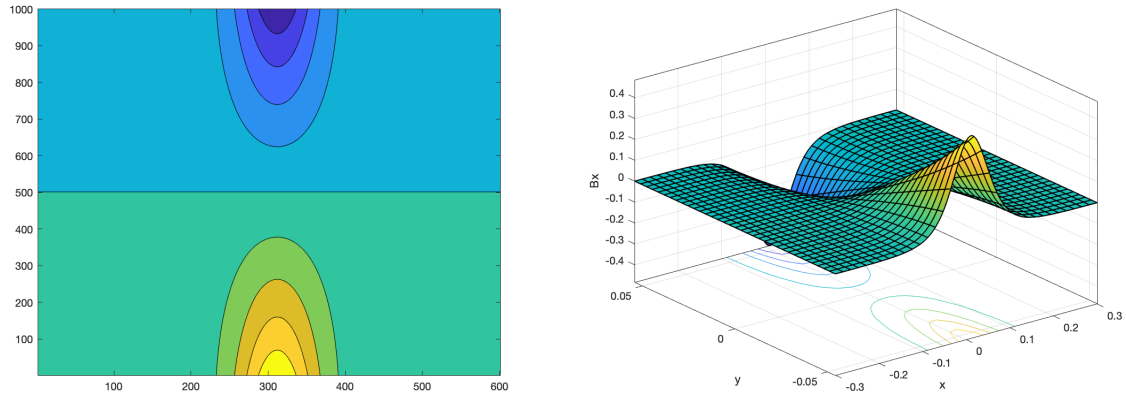

Figure 7.5: Full magnetic field $B_x(x, y)$ in (left) 2D, (right) 3D.

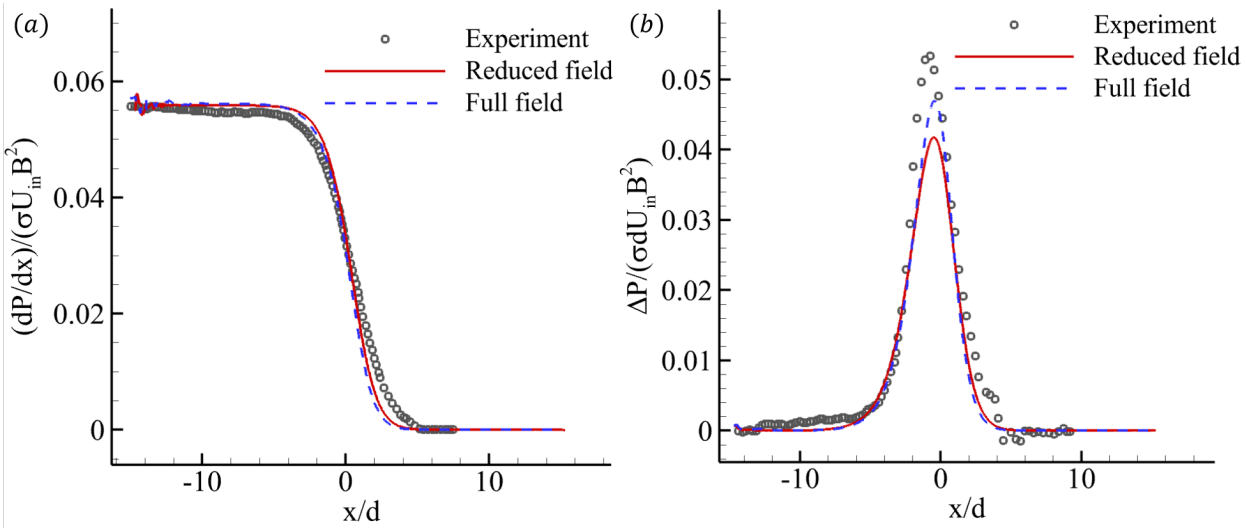

Figure 7.6: Comparison of full/reduced field computational results and ALEX [5] experimental results for pressure gradient and transverse pressure difference.

$1000, 2000, 5000, 10000$, $Ha^* = 175.5, 263.3, 438.8, 585.0$. The total number of computed cases is 80, with corresponding interaction number N shown in Table 7.1. Based on the experimental data [75], the flow is assumed to be laminar based on the empirical criterion for turbulence suppression in MHD channel flows for the case of a wall-normal magnetic field that suggests the MHD flow laminarization for $\frac{Ha}{Re} > \left(\frac{Ha}{Re}\right)_{cr} \approx \frac{1}{200}$. In this study, the lowest Ha is 1000 and the highest Re is 10,000, and therefore the minimum value of $\frac{Ha}{Re}$ is 0.1, which means the flow is laminar. Due to the nature of fringing magnetic field distribution, the magnetic field intensity at the outlet of the duct can reach a value where turbulence cannot be suppressed by electromagnetic force anymore. Therefore, the added magnetic field B_{add} functions as the artificial term to meet the minimum laminar flow requirement.

7.2 Validation case for quasi-2D MHD flow

The validation case of 2D fully developed MHD duct flow under the influence of a uniform magnetic field was already mentioned in the last manifold problem. However, COMSOL's

Table 7.1: Interaction number N for different Ha and Re cases

Ha/Re	1000	2000	5000	10000
1000	1000	500	200	100
2000	4000	2000	800	400
3000	9000	4500	1800	900
5000	25000	12500	5000	2500
10000	100000	50000	20000	10000

capability of predicting MHD flow in a spatially-varying magnetic field is still unknown. Therefore, a validation case was created which involves the same geometry and magnetic field given in [62]. The magnetic field is expressed by one component:

$$B_y = B_u \times \frac{1 + \tanh(10x + 7.315)}{2}.$$

The geometry and magnetic field distribution are shown in Figure 7.7. In this case, R_i=0.0111 m, R_o=0.0127 m, L=0.8 m, Re = 9700, Ha = 322. Here the characteristic length is chosen to be the inner radius R_i.

The formula of 2D fully developed MHD flow pressure drop in a circular conducting duct is given by Miyazaki et al. [79]:

$$\Delta p = L_e \cdot \frac{c_w}{1 + c_w} \cdot \sigma_f U B_0^2,$$

where the wall conductance ratio is defined by:

$$c_w = \frac{\sigma_w}{\sigma_f} \cdot \frac{R_o^2 - R_i^2}{R_o^2 + R_i^2}.$$

For the estimation of pressure drop for MHD flow in a strong fringing magnetic field region, Miyazaki et al. [6] proposed a simple integral method of pressure gradient along magnetic field:

$$\Delta p = \frac{c_w}{1 + c_w} \int \sigma_f U B^2 dx,$$

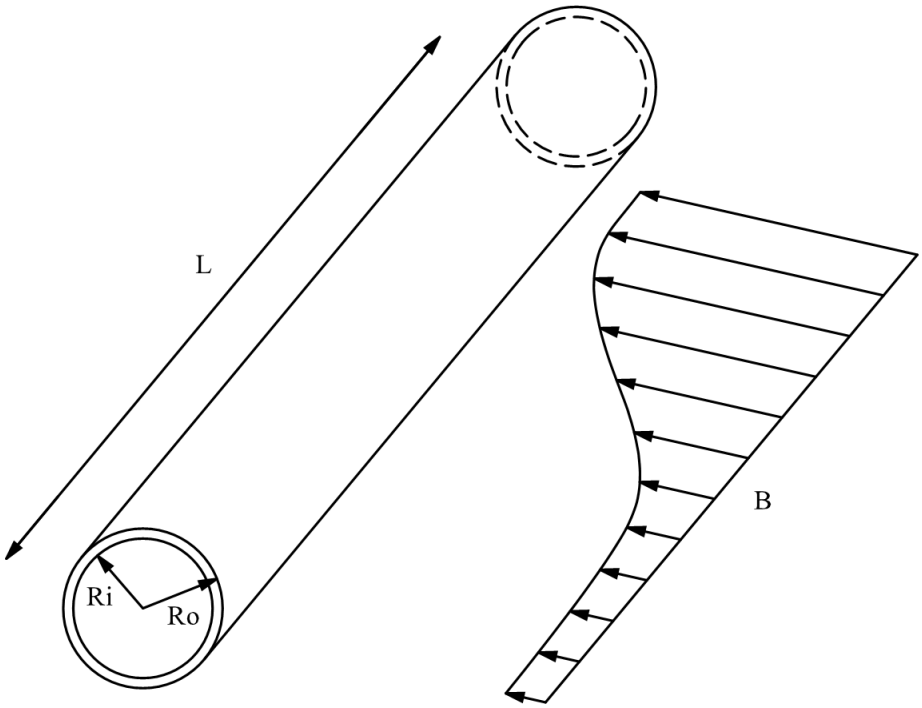

Figure 7.7: Schematic illustration of 3D MHD flow in fringing magnetic field for validation.

while for a steady flow with constant temperature, the relation can be simplified by:

$$\Delta p = \frac{c_w}{1 + c_w} \cdot \sigma_f U \int B^2 dx.$$

Therefore, by comparing results computed by COMSOL and predicted by Miyazaki, the computational tool can be shown to have the ability to simulate MHD flow in a fringing magnetic field. The comparison of pressure drop for a fixed distance of ΔL=0.6 m using same fully developed pressure gradient estimation method in [62] by COMSOL and by Miyazaki et al. [6] is shown in Figure 7.8. An excellent agreement can be seen from the figure, indicating that the prediction of pressure distribution is precise for such a flow.

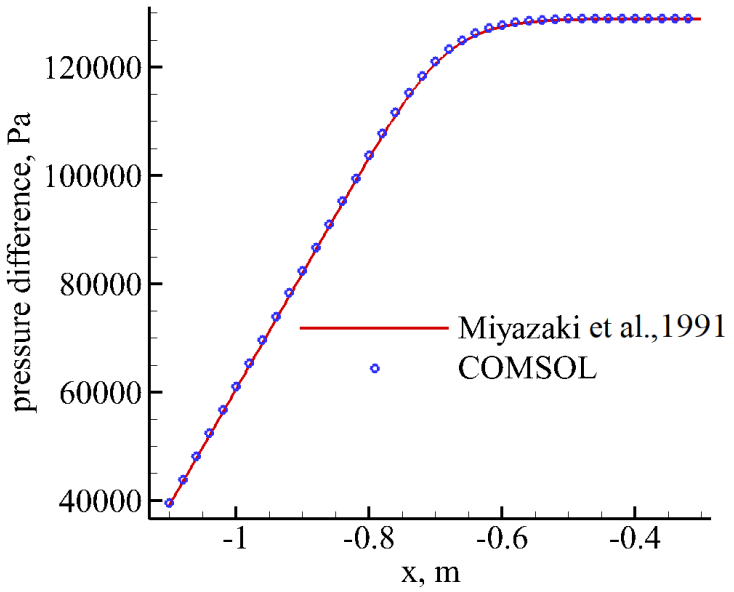

Figure 7.8: Comparison of results given by Miyazaki et al [6] and COMSOL.

7.3 Validation case for the rectangular duct for high Hartmann number

Despite the successful validation of quasi-fully developed MHD flow in a fringing magnetic field for COMSOL, more studies are needed for high Hartmann number cases where the axial currents will dominate over the cross-sectional currents, when 3D effects are more prominent. The computational results for high Hartmann number cases would be compared against experimental data for rectangular duct obtained in [5] (ALEX results), in which measurements of MHD pressure drop were performed for both rectangular duct and circular pipe geometries, and for two sets of Ha/Re combinations. The details of the ALEX experiments are shown in Table 7.2. The axial pressure distribution and the transverse pressure difference within Hartmann and side layers are shown in Figure 7.9. In this validation, the rectangular duct case with $Ha = 2900$ and $Re = 540$ was selected.

The geometry used for the validation is shown in Figure 7.10, in which $d = a = 0.0439m$,

Table 7.2: Details of ALEX experimental cases

Parameter	Round	Square
duct half width, cm	5.41	4.39
wall conductance ratio	0.03	0.07
B field (max/min), T	2.08/0.97	2.3/1.1
Ha (max/min)	6640/3070	5800/2900
N (max/min)	11000/606	126000/540
U (max/min), cm/s	27.9/7.0	33.9/0.58

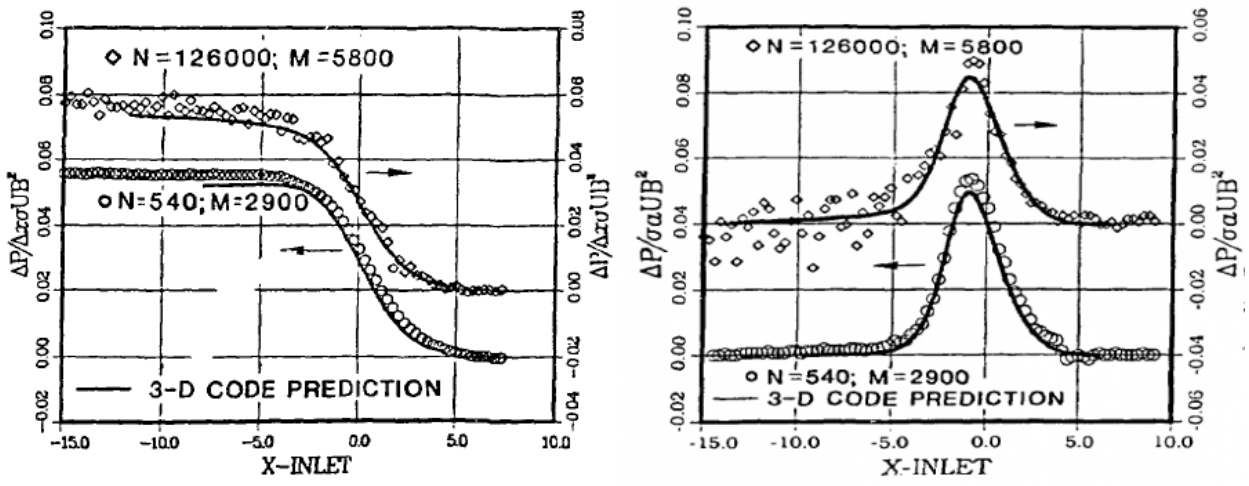

Figure 7.9: ALEX results for rectangular (square) duct: (left) axial pressure distribution at centerline, (right) transverse pressure difference for Hartmann and side layers.

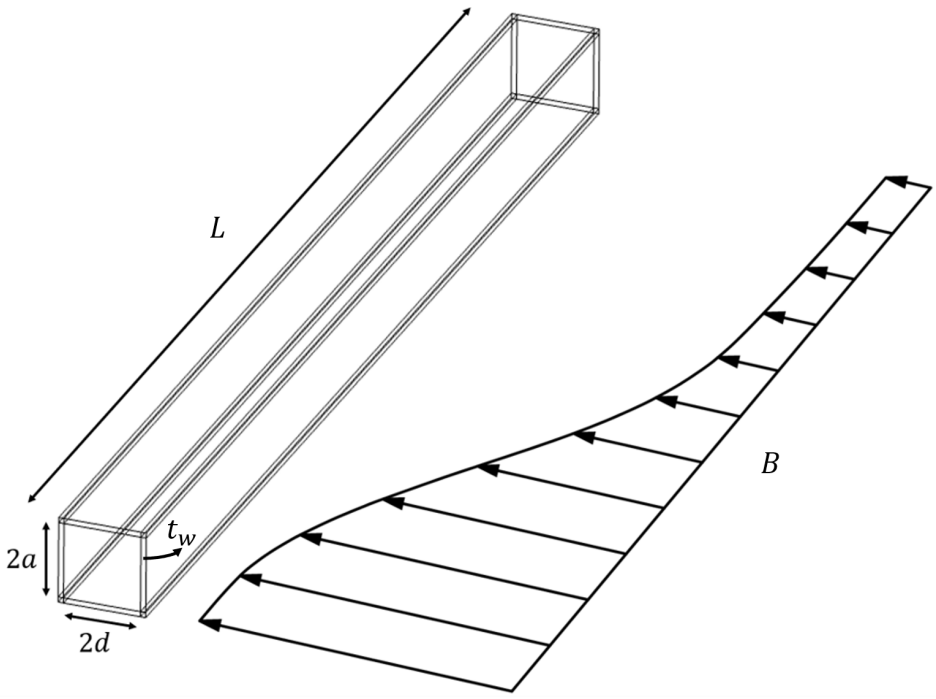

Figure 7.10: Schematic illustration of case validation of ALEX results.

$L = 30d$. In this case, a reduced form of magnetic field was chosen with the maximum magnetic field intensity being $1.1T$. A specific form of the magnetic field with γ and d defined in [61] was used for approximation of experimental magnetic field, which gives:

$$B_y = 1.1 \times \frac{1 - \tanh[0.45(\frac{x}{0.0439} - 0.33)]}{2}.$$

The magnetic field defined in computation is plotted against the experimental field in Figure 7.11, in which the two fields correspond with each other very well.

The comparisons of results from Reed et al. [5] and COMSOL for the described case are shown in Figure 7.12. Also, the computed results from HIMAG by previous studies are plotted on the figure. As mentioned in [5], the axial pressure gradient is scaled as: $\frac{dP}{dx}^* = \frac{\frac{dP}{dx}}{\sigma U B^2}$ and transverse pressure difference scaled as: $\Delta P^* = \frac{\Delta P}{\sigma b U B^2}$. A good match can be observed for the results from all three data for the dimensionless pressure gradient along axis. While for the transverse pressure difference, HIMAG and COMSOL correspond well with each other, with slight deviation from the experimental data. The results indicate that

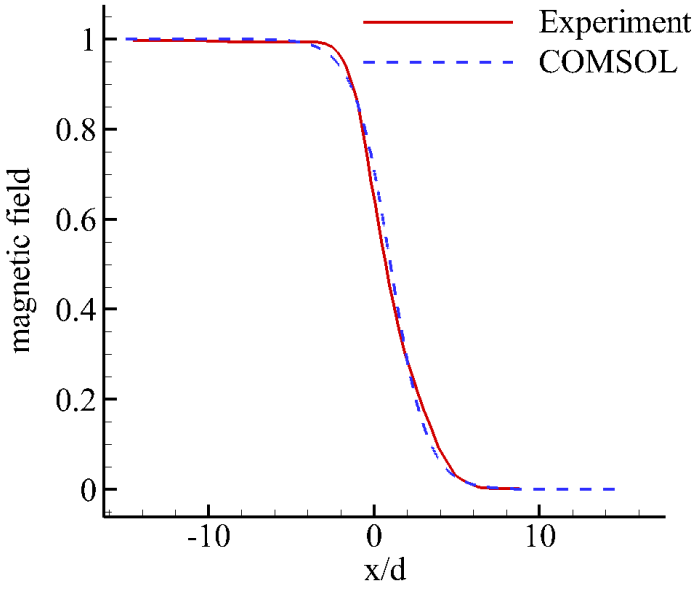

Figure 7.11: Comparison of magnetic field used in experiment and COMSOL.

COMSOL can accurately predict the MHD flow in a fringing magnetic field.

7.4 Computational setup in COMSOL

The computational setup for MHD flow in a fringing magnetic field in COMSOL is quite similar to that in the expansion/contraction manifold. Instead of being constant, a spatially-varying magnetic field should be defined properly, which can be realized through analytical function definition in COMSOL. The electric currents caused by fluid motion and the Lorentz forces are user-defined in the laminar flow and electric currents physics section. Also, various solvers can be chosen for computations, with iterative/segregated solvers consuming less memory but require more time for convergence, compared to the direct solver which can be more efficient but needs a large amount of memory. Based on the study of the relation between number of mesh elements and virtual memory required, a total maximum number of around 500,000 elements can be used for computation considering the 512GB RAM capacity

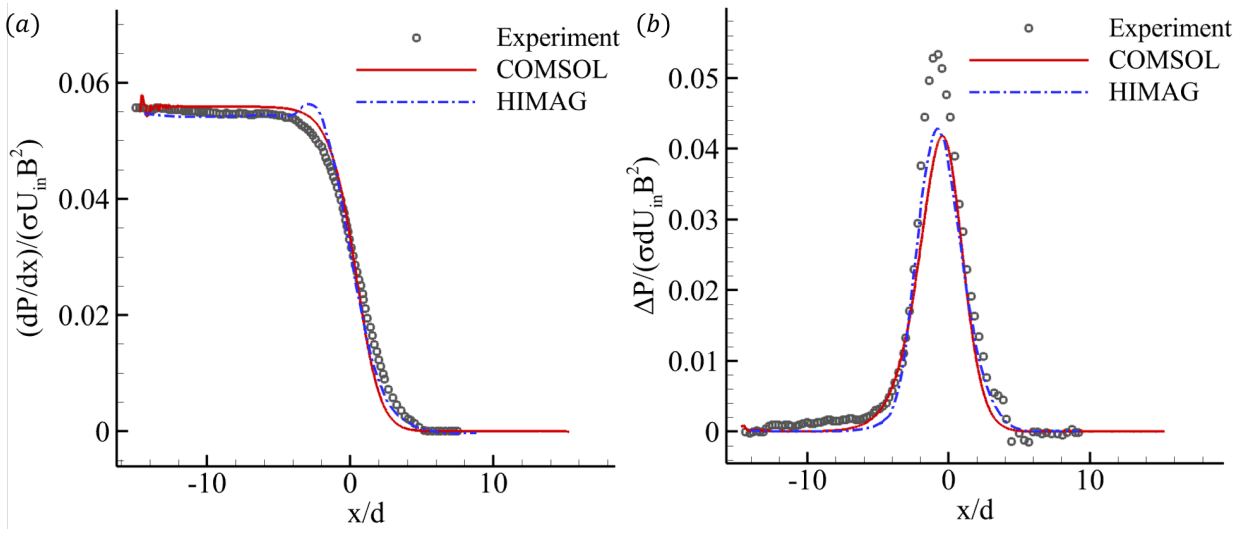

Figure 7.12: Comparison of axial pressure gradient from experiment, HIMAG and COMSOL.

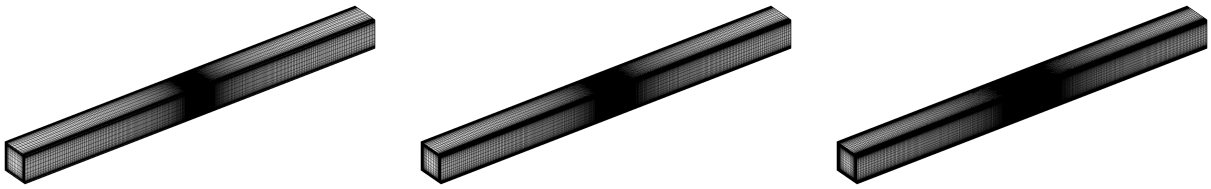

Figure 7.13: Three types of structured meshes used in mesh sensitivity study: (left) coarse, (middle) normal and (right) fine.

using direct solver. The mesh elements are clustered near the center of the duct where the absolute value of magnetic field gradient reaches maximum to better resolve the flow characteristics. Again, at least 7 elements in the Hartmann layer and 12 points in the side layer are guaranteed to precisely compute the flow in these regions.

Before continuing with the computational matrix, a mesh sensitivity study was conducted. Three types of meshes were created, as shown in Figure 7.13. The coarse mesh consists of 1,075,200 elements, the normal mesh has 2,100,000 elements and the fine mesh has 4,963,200 elements. Results of axial pressure gradient and transverse pressure difference for three types of meshes are shown in Figure 7.14. The normal and fine meshes exhibit

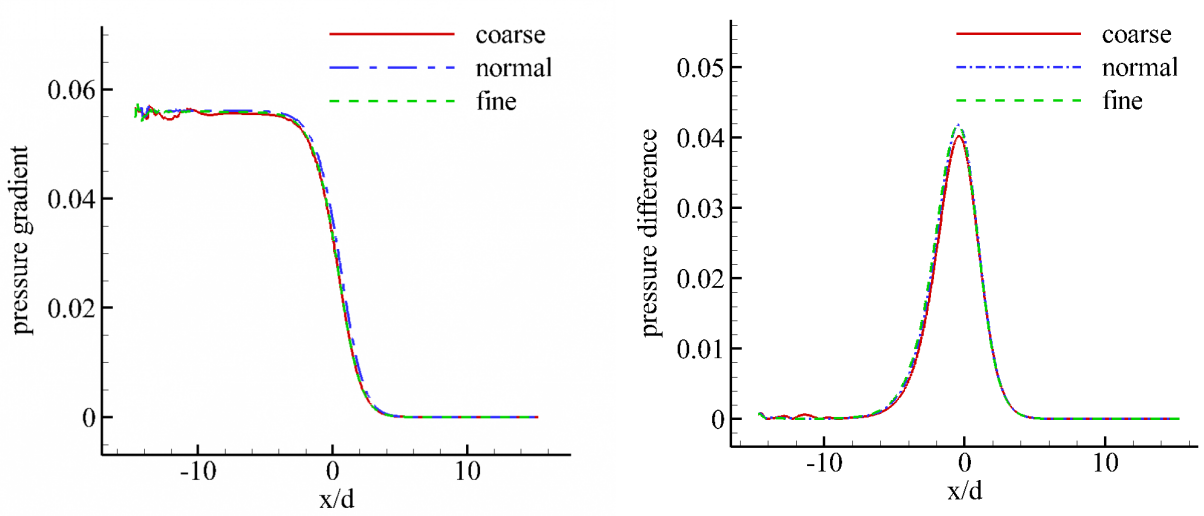

Figure 7.14: Comparison of results for (left) axial pressure gradient and (right) transverse pressure difference for three meshes.

very small difference for the results, which are not exactly the same as the coarse mesh. Therefore, the normal mesh is considered to be enough for solving this problem.

7.5 Flow characterization and distributions

Similar to description of flow in a manifold, the flow in a fringing magnetic field needs to be characterized for velocity, pressure, electric current changes.

The liquid metal *PbLi* enters the non-conducting rectangular duct and quickly becomes fully developed 2D MHD flow in the uniform magnetic field region. When approaching the middle of the duct, the flow experiences 3D effects for both velocity, pressure, electric potential and electric currents. Such a region is related to the abrupt change of magnetic field and the resulting Lorentz force. The Lorentz force reshapes the flow velocity field, causing the induced electric currents to change from 2D cross-sectional to 3D with axial component. This change will also cause dramatic 3D MHD pressure drop, which resembles

the effect of a sudden change in geometry. The 3D effects are also determined by Ha^*, which controls the gradualness of the change of magnetic field. The extreme case of uniform magnetic field will provide lowest pressure drop but is not realistic for fringing field. In this section, the typical characteristics of the flow will be shown for particular case of $Ha = 3000, Re = 2000, Ha^* = 263.3$, which is about in the middle of the computational matrix and thus considered a representative case of the flow. The effect of Ha, Re, Ha^* on the flow is prominent and will be further explained. The characteristics of the flow includes 3D electric currents, 3D MHD pressure drop, flow redistribution near the center of the duct and 2D cross section flow velocity contours, which will be illustrated through 1D, 2D and 3D figures.

Figure 7.15 shows the main characteristics of the MHD flow in a fringing magnetic field. The 2D velocity contour illustrates axial velocity change along the duct, shown in Figure 7.15(a). The flow enters the rectangular non-conducting duct with plateau-like fully developed velocity, and continues to remain the same profile until close to the center of the duct, where $\frac{dB}{dx}$ increase dramatically, and the flow is diverted into the side layers due to Lorentz forces. The mid-plane ($y = 0$) velocity streamlines in Figure 7.15(b) clearly describe the flow characteristics in the middle of the duct, and it can be observed that two steady counter-rotating vortices are present. The vortices are created by the flow-obstructing Lorentz force due to axial electric currents, which will be explained later. The pressure along axial direction shown in Figure 7.15(d) is made up of three parts: a fully-developed 2D MHD for 1/4 of the total duct length, a rapidly dropping and slowly rising 3D MHD pressure change for 1/2 of the duct, followed by another fully-developed 2D MHD with weaker magnetic field for 1/4 of the duct. The 3D MHD pressure drop ΔP_{3D} is defined such that it is measured by intersecting the middle position of the duct (where $\frac{dB}{dx}$ reaches maximum value) with upstream and downstream fully developed 2D MHD pressure line. Besides velocity and pressure, the electric currents are also changing in different sections of the duct, shown in Figure 7.15(c). Near the inlet, the electric currents gradually become 2D cross-sectional due to the nature

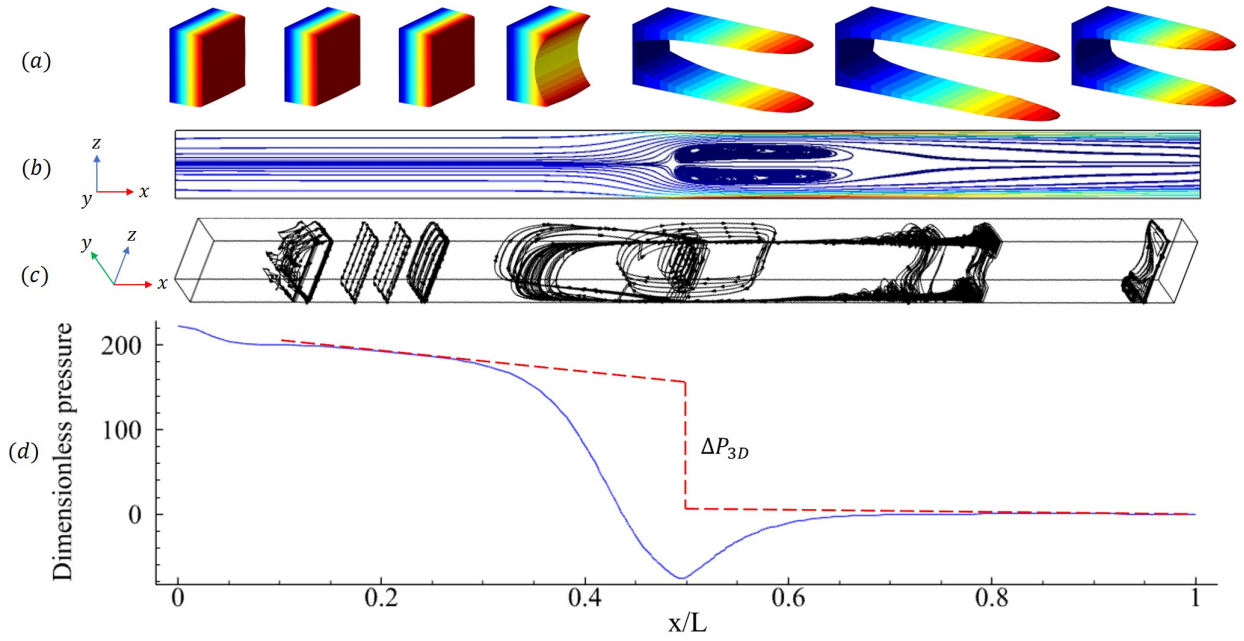

Figure 7.15: Characterization of MHD flow in a fringing magnetic field for $Ha = 3000, Re = 2000, Ha^* = 263.3$. (a) 2D velocity contour along axial direction for MHD flow in fringing field. (b) 3D velocity streamlines in xz direction (c) 2D/3D electric currents streamlines (d) 1D pressure distribution along the center line showing the definition of ΔP_{3D}.

of fully developed 2D MHD flow. In this section, the Lorentz force $\mathbf{J} \times \mathbf{B}$ is pointing at $-x$ direction and obstruct the core flow to create a flat velocity profile with very thin Hartmann and side layers. Under the effect of fringing magnetic field, the electric currents develop an axial component, and the corresponding Lorentz force alters its direction to y, pushing the flow to side layers. Such a phenomenon becomes less prominent when entering the second developing section, where the electric currents return to 2D near the outlet and the velocity takes a much longer distance to become fully developed again.

In order to understand the 3D MHD effects in the middle of the duct where abrupt change of magnetic field happens, the electric potential and electric currents at $y = 0$ plane are shown in Figure 7.16. For the region right after fully developed flow $x < -0.15m$, the

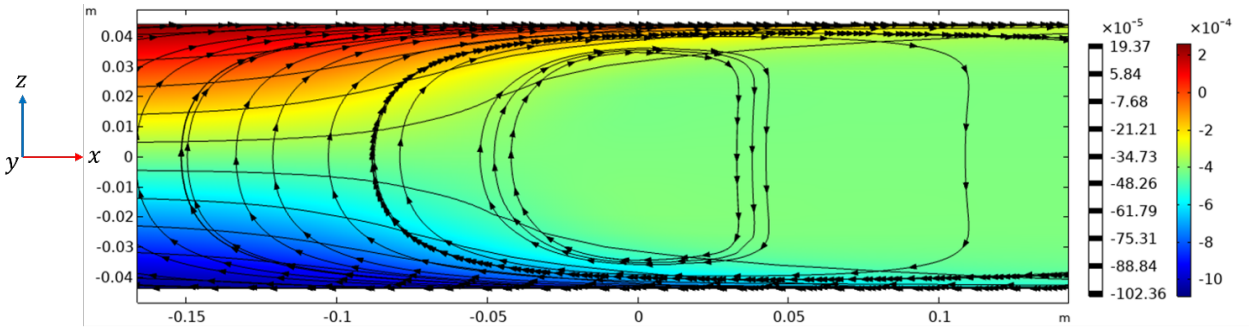

Figure 7.16: Electric current paths and electric potential contour in the $y = 0$ center plane for $Ha = 3000, Re = 2000, Ha^* = 263.3$.

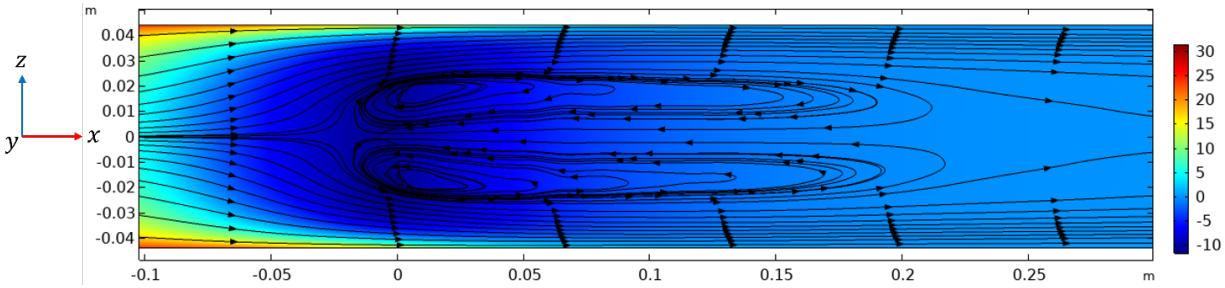

Figure 7.17: Pressure contour and velocity streamlines in $y = 0$ center plane for $Ha = 3000, Re = 2000, Ha^* = 263.3$.

electric potential is more linearly distributed. The 3D effect can be observed when electric potential is more uniform in the y direction and steeply changes near the wall. Such a phenomenon causes the electric currents to flow in the axial direction, whose circuit is closed upstream and downstream of each xz plane. The resulting Lorentz force will exhibit different directions, pointing $+y$ for the $y > 0$ region and $-y$ for $y < 0$ region.

Figure 7.17 shows the pressure and streamlines in Hartmann layer at $y = -b + \frac{b}{2Ha}$. Near $x = 0$, there exists a low pressure area, where the pair of counter-rotating vortices starts. The pressure recovery after $x = 0$ cause the flow to recirculate in the middle of the duct. The flow which is not involved in the center vortices is diverted into the region near the wall, and after passing the recirculation zone, gradually returns to the center of the duct.

The streamlines clearly illustrates this phenomenon, which also helps explain the effect of Lorentz force on the flow characteristics.

7.6 3D MHD pressure drop

The 3D MHD pressure drop is closely related to the 3D nature of the flow near the center of the duct, which is caused by the sudden change of fringing magnetic field, and the resulting 3D electric currents. The detailed observation of physics of the flow are already explained in previous section, and in this section the main focus is on the analysis of pressure drop and establishment of correlations. The measurement of 3D MHD pressure drop ΔP_{3D} has been defined in Figure 7.15(d). As mentioned, in this study, the dimensionless parameters are chosen such that $Ha = 1000, 2000, 3000, 5000, 10000; Re = 1000, 2000, 5000, 10000$ and $Ha^* = 175.5, 263.3, 438.8, 585.0$. In total, 80 cases were finished and the corresponding pressure drops were computed to fill into matrix, shown in Table 7.3, 7.4, 7.5 and 7.6.

Table 7.3: Pressure drop coefficient k for $Ha^* = 175.5$

Ha/Re	1000	2000	5000	10000
1000	4.419E+01	2.385E+01	1.155E+01	7.273E+00
2000	1.173E+02	6.984E+01	3.374E+01	2.020E+01
3000	2.098E+02	1.271E+02	6.085E+01	3.563E+01
5000	4.427E+02	2.505E+02	1.196E+02	7.034E+01
10000	1.099E+03	6.415E+02	2.664E+02	1.901E+02

7.6.1 Effect of Ha, Ha^* and Re

Characterizing effect of Ha^* on the pressure drop coefficient is one of the main goals of the study for the reason that it is related to the suddenness of change of magnetic field. Figure 7.18 shows the dimensionless pressure distribution along center axis of the duct for

Table 7.4: Pressure drop coefficient k for $Ha^* = 263.3$

Ha/Re	1000	2000	5000	10000
1000	6.055E+01	3.350E+01	1.552E+01	8.700E+00
2000	1.644E+02	9.549E+01	4.493E+01	2.645E+01
3000	2.847E+02	1.623E+02	8.155E+01	4.726E+01
5000	5.802E+02	3.284E+02	1.630E+02	9.671E+01
10000	1.423E+03	7.853E+02	3.747E+02	2.236E+02

Table 7.5: Pressure drop coefficient k for $Ha^* = 438.8$

Ha/Re	1000	2000	5000	10000
1000	7.755E+01	4.510E+01	2.176E+01	1.291E+01
2000	2.094E+02	1.219E+02	6.543E+01	4.010E+01
3000	3.704E+02	2.158E+02	1.085E+02	7.051E+01
5000	7.477E+02	4.360E+02	2.096E+02	1.348E+02
10000	1.936E+03	1.167E+03	5.012E+02	3.163E+02

Table 7.6: Pressure drop coefficient k for $Ha^* = 585.0$

Ha/Re	1000	2000	5000	10000
1000	9.153E+01	5.305E+01	2.500E+01	1.511E+01
2000	2.472E+02	1.447E+02	7.551E+01	4.279E+01
3000	4.246E+02	2.502E+02	1.270E+02	9.221E+01
5000	8.924E+02	5.012E+02	2.607E+02	1.594E+02
10000	2.100E+03	1.158E+03	7.099E+02	4.307E+02

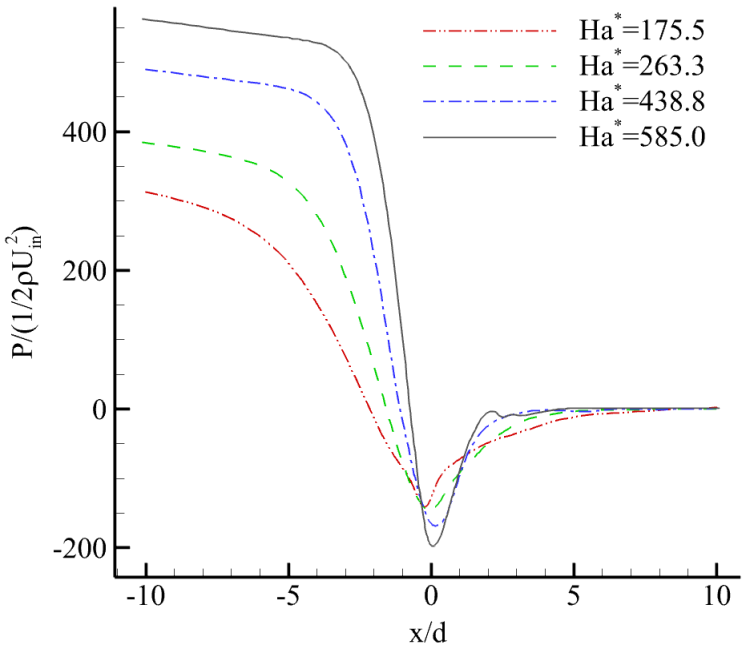

Figure 7.18: Effect of Ha^* on pressure distribution. Dimensionless pressure is shown along the duct center axis.

all Ha^*, for $Ha = 5000, Re = 2000$. As can be seen, the pressure drop coefficient significantly increases by over 2 times when Ha^* increase, which corresponds to the steeper change of the magnetic field. This trend persists for all other Ha and Re combined and is vital in studying the effect of fringing field on the MHD flow.

The effect of Re and Ha on k is shown in Figure 7.19. The 3D MHD pressure drop coefficient decreases with Re when Ha, Ha^* are fixed, which is a result of increased flow velocity and the inertia force making the flow pressure distribution smoother. While for the same Re, Ha^*, the pressure drop coefficient will increase with Ha. This is caused by higher flow-obstructing Lorentz force due to the increase of magnetic field intensity. When Ha, Re are fixed, the pressure drop coefficient becomes higher when Ha^* increases.

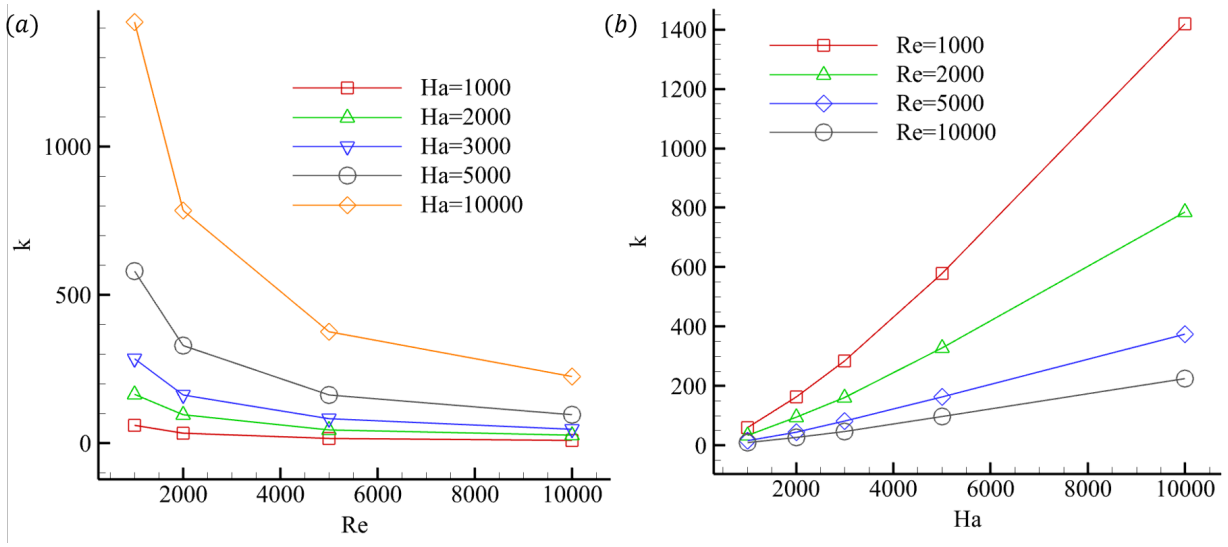

Figure 7.19: Pressure drop coefficient k (a) as a function of Re, and (b) as a function of Ha.

7.6.2 Construction of correlation

After studying the effect of Ha, Ha^* and Re on 3D MHD pressure drop, the correlation is constructed using the form $\Delta P_{3D} = \left(s \cdot Ha^a Re^b\right) \cdot \left(\frac{\rho U^2}{2}\right)$, where s, a, b are three coefficients that need to be determined. The power coefficients a, b are computed using R-square linear regression analysis to find the highest R-square value from the range $a = -3 \sim 3, b = -3 \sim 3$. The optimum a, b values are obtained for different Ha^* and the results are highly consistent. The linear regression gives the value of $a = 1.33, b = -0.8$. This indicates that the pressure drop is dependent on Ha, Re at the same time as expected. The last step is to find out the relationship between s and Ha^*, and with a, b fixed, the s values can be easily calculated for curve-fitting against Ha^*. The second-order polynomial gives a perfect fitting with the correlation $s = -5.09 \times 10^{-6} Ha^{*2} + 6.96 \times 10^{-3} Ha^* + 0.2416$, so that the correlation for the 3D MHD pressure drop coefficient k is constructed such that:

$$k = (-5.09 \times 10^{-6} Ha^{*2} + 6.96 \times 10^{-3} Ha^* + 0.2416) \cdot Ha^{1.33} Re^{-0.8} \tag{7.1}$$

This correlation describes the pressure drop for a data range of $1000 < Ha < 10000$, $1000 < Re < 10000$, $175 < Ha^* < 585$. The data points for 80 cases are plotted on

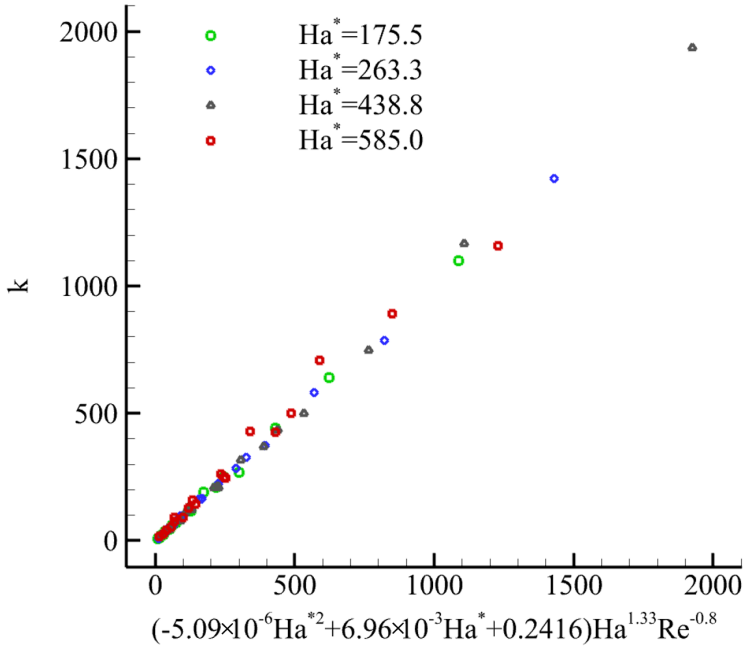

Figure 7.20: Best fit for the obtained data for the 3D MHD pressure drop coefficient k for different magnetic fields, based on 80 computed cases.

the same figure against the correlation, and the R-square value is 0.9967, which indicates the correlation to be a perfect fit for predicting the 3D MHD pressure drop, as shown in Figure 7.20.

7.7 Recirculation and flow development zone

Besides the 3D MHD pressure drop, the flow demonstrates other 2D and 3D characteristics. At the sudden change of magnetic field, the flow is obstructed by the Lorentz forces, and hence two symmetric counter-rotating vortices form. The vortices exist in a certain region, defined here as the recirculation zone. After this region, the flow axial velocity in the center line will increase and reach a constant value after certain distance. This process is described through the flow development zone, where the flow transits from full 3D to quasi-2D state.

The recirculation flow structure is shown in Figure 7.21, where 3D streamlines are plotted

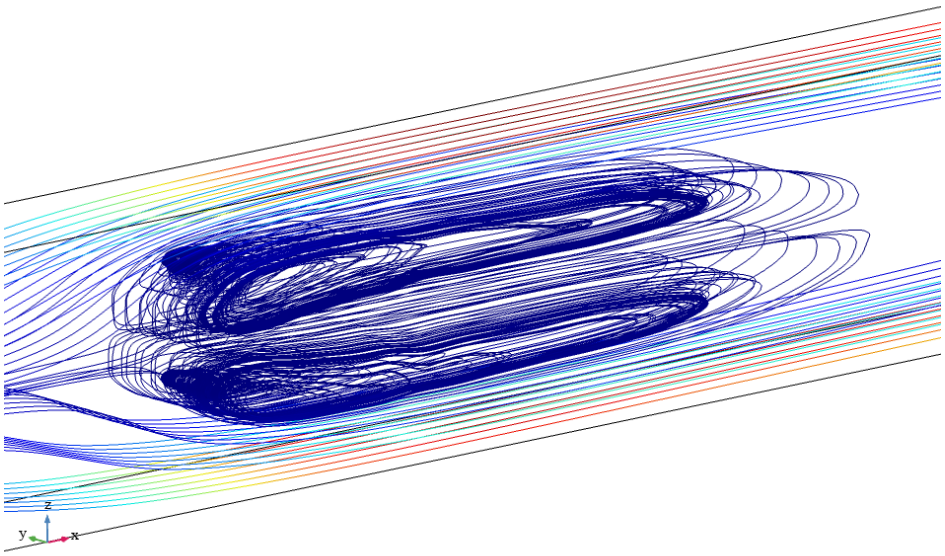

Figure 7.21: A recirculation flow bubble in the recirculation zone at $Ha = 3000, Re = 2000, Ha^* = 263.3$. 3D flow streamlines are shown.

near the center of the duct to show the detailed recirculation flow bubble. As shown in the figure, the recirculation zone extends through the duct width in y direction and further downstream of the duct in x direction.

The effect of Ha on the recirculation flow is shown in Figure 7.22, in which the streamlines are plotted in the middle xz plane at $y = 0$ for $Re = 2000, Ha^* = 263.3$ for different Ha. When $Ha = 1000$, the recirculation zone is not formed. As the increase of Ha, the recirculation zone begins to exist and is more stretched into the downstream region, and the recirculation bubble expands in the z direction.

Figure 7.23 illustrates the effect of different Re on the recirculation flow for $Ha = 1000, Ha^* = 263.3$. Re plays the opposite role in the formation of recirculation zone. As can be seen in the figure, the increase of Re will lead to the shrinkage and finally disappearance of recirculation zone above 2000. At the same time, the flow becomes fully developed in a shorter distance downstream of the duct.

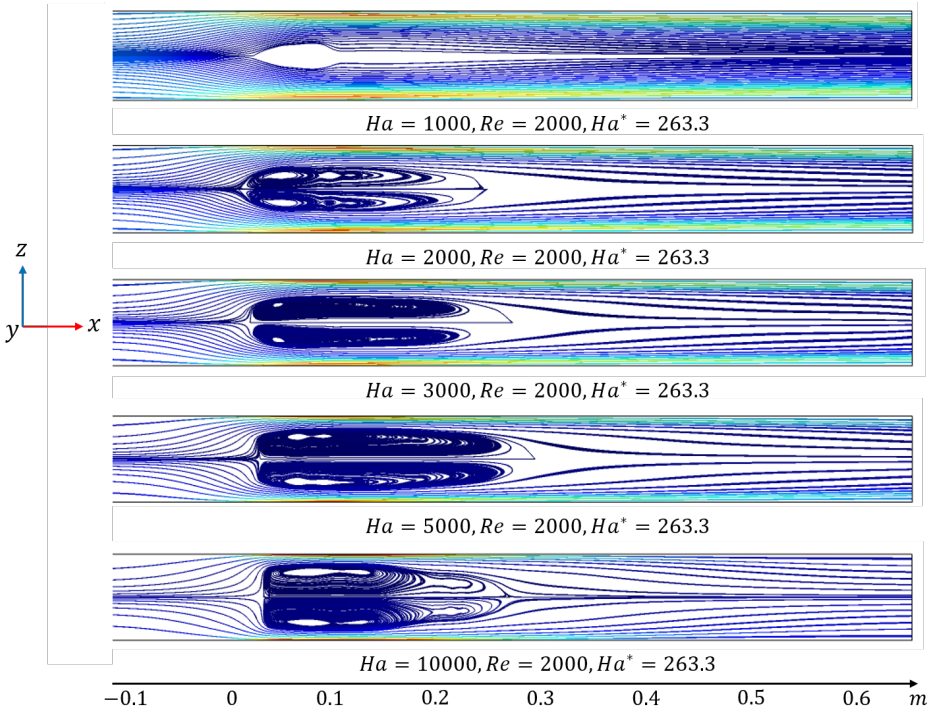

Figure 7.22: Effect of Ha on the flow recirculation zone at $Re = 2000, Ha^* = 263.3$, flow streamlines plotted on the middle plane.

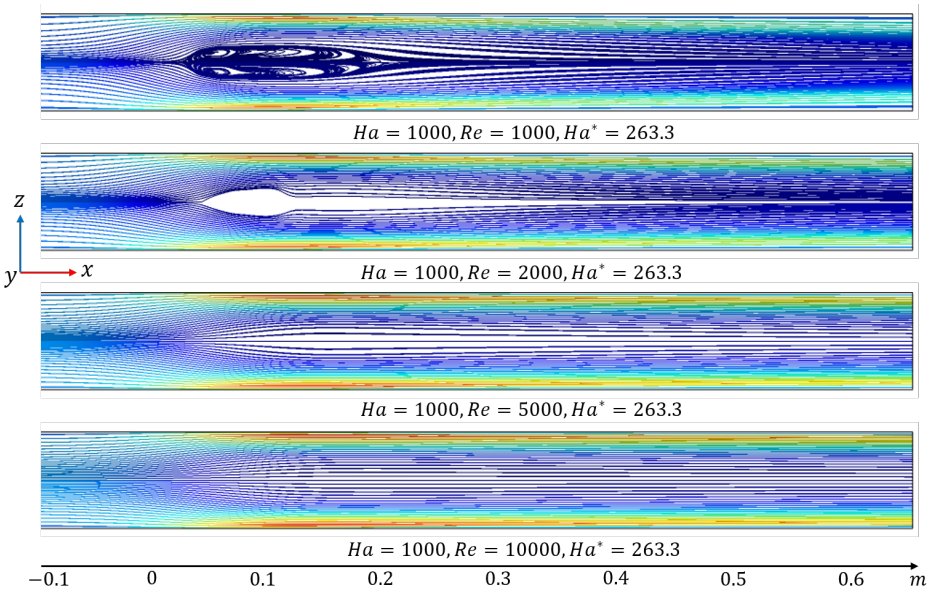

Figure 7.23: Effect of Re on the recirculation flow for $Ha = 1000, Ha^* = 263.3$.

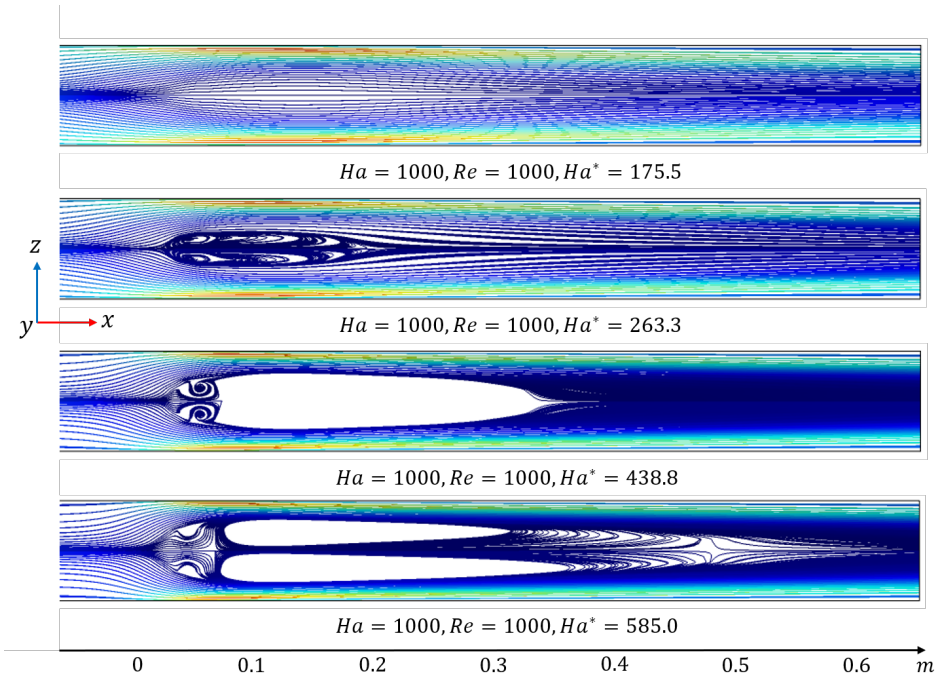

Figure 7.24: Effect of Ha^* on the recirculation flow for $Ha = 1000, Re = 1000$.

The gradualness of change of the fringing magnetic field also affects the recirculation zone. This influence is shown in Figure 7.24 by varying Ha^* for $Ha = 1000, Re = 1000$. For $Ha^* = 175.5$, the magnetic field is relatively smooth, and therefore the recirculation zone doesn't exist. When $Ha^* = 263.3$, the recirculation flow begins to form and takes the center region of the duct. As the further increase of Ha^*, the recirculation zone becomes larger in the y direction and stretched in the x direction.

7.8 3D effects, force balance and inertia

The MHD flow in a fringing magnetic field in this study exhibits 3D effects which cannot be predicted by the quasi-2D assumption for this type of flow. The recirculation zone is one of the key indications that the flow is not similar to the 2D developed MHD flow. To further illustrate the 3D effects, the magnitude of pressure difference in the Hartmann layer at $y = -d + \frac{d}{2Ha}, z = 0$ and side layer at $z = -a + \frac{a}{2\sqrt{Ha}}, y = 0$ non-dimensionalized by

$\sigma d U_{in} B^2$ is plotted in Figure 7.25 for $Ha = 3000, Ha^* = 263.3$. In the fully developed region, the pressure difference in the two boundary layers (transverse pressure difference ΔP^*) is 0, which indicates no difference for pressure distribution in the cross section of the duct in these regions. However, in the fringing region where magnetic field experiences sudden change, the pressure difference is obvious and changes with Re. As the increase of Re, ΔP^* also increases, which explains the strong 3D effects experienced by the flow. To reveal the 3D effects on the flow caused by change of magnetic field furthermore, the pressure gradient at the center axis is calculated using quasi-2D assumption, where the locally defined pressure drop coefficient λ is related to the pressure gradient as $\frac{\Delta P}{x} = \frac{\lambda(B)}{d} \cdot \frac{\rho U_{in}^2}{2}$. For a rectangular duct with insulating wall, the pressure drop coefficient is given by $\lambda = \frac{2Ha}{Re}\left(1 - \frac{1}{Ha} - \frac{0.852}{\beta Ha^{\frac{1}{2}}}\right)^{-1}$ where β is the duct aspect ratio. The results of comparison between COMSOL computations and quasi-2D calculations are shown in Figure 7.26(a) for $Ha = 1000, Re = 1000$ and Figure 7.26(b) for $Ha = 1000, Re = 5000$. It can be clearly observed that the flow pressure gradient is totally different from a locally 2D flow, which indicates the significant 3D effects present. As the increase of Re, the 3D effect will become more prominent.

In the present study of MHD flow in the fringing magnetic field, the effect of inertia on the flow is prominent for cases with higher Re ($Re > 2000$). In Figure 7.27, all the forces acting on the flow, including electromagnetic forces, pressure, inertia and viscous forces are shown along the duct center axis, which falls in the core flow region. It can be clearly observed that the electromagnetic force and pressure are balancing each other in the bulk flow, while the inertia and viscous forces are negligible compared to them.

The effect of inertia forces on the flow can be shown by comparing the full flow model which includes all existing forces with the reduced model with no convective term in the momentum equation. In COMSOL, the inertialess approximation can be applied by choosing "neglect inertia forces" and using so-called "creeping flow" for the fluid model. Although the inertia forces are confined in the thin boundary layers, the effect of them on the flow is non-negligible, such as the pressure drop in Figure 7.28 and recirculation zone in Figure 7.29.

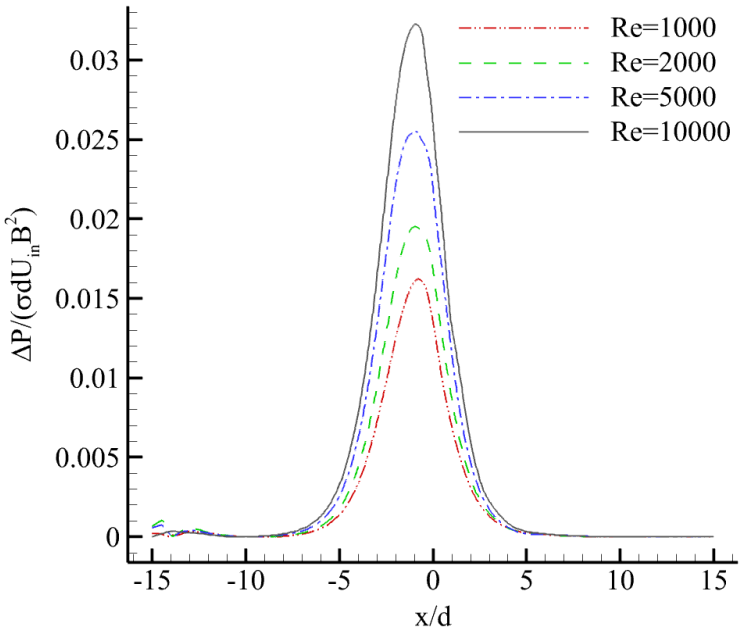

Figure 7.25: Transverse pressure difference for $Ha = 3000, Ha^* = 263.3$ for different Re.

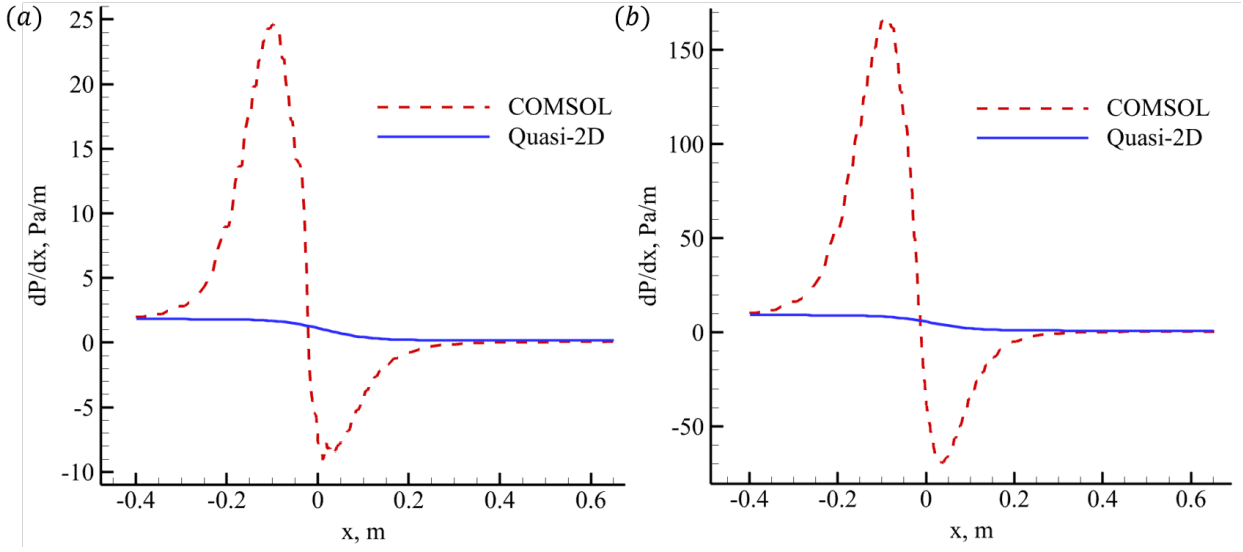

Figure 7.26: Comparison of pressure gradient at center axis computed by quasi-2D relation and 3D simulation for (a) $Ha = 1000, Re = 1000$ (b) $Ha = 1000, Re = 5000$.

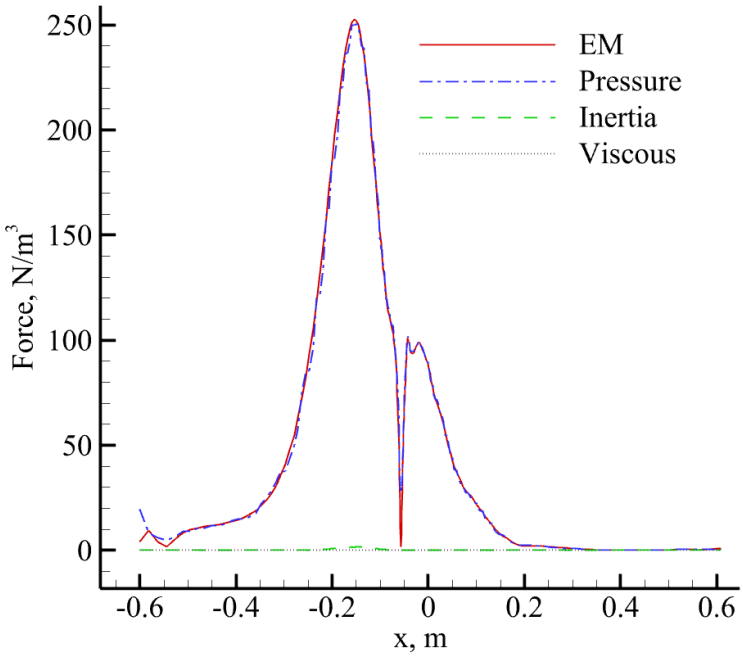

Figure 7.27: Force balance in the core flow at duct center axis for $Ha = 3000, Re = 2000, Ha^* = 263.3$.

For small velocity ($Re = 1000$) and $Ha = 5000$, the relative difference of pressure drop coefficient k using inertia/inertialess model is 8%, which indicates that the inertia effect is small. However, as flow velocity and Re increases the discrepancy between two flow models increases rapidly, with 20% for $Re = 2000$ and 34% for $Re = 5000$. This shows that the inertia effects are strong and the flow cannot be treated as "creeping" any more. The recirculation bubble length and size are also different for the two flow models. When using the full model, the recirculation flow extends more downstream of the duct, and the corresponding pressure drop caused by the recirculation will be larger. Also, the full flow model predicts two pairs of recirculation bubbles while the reduced model only predicts one. Such a phenomenon further confirms that under the real blanket conditions when Ha and Re are significantly higher than in the current study, the inertia effects must be considered and a full momentum equation should be solved, otherwise the pressure drop will be underestimated.

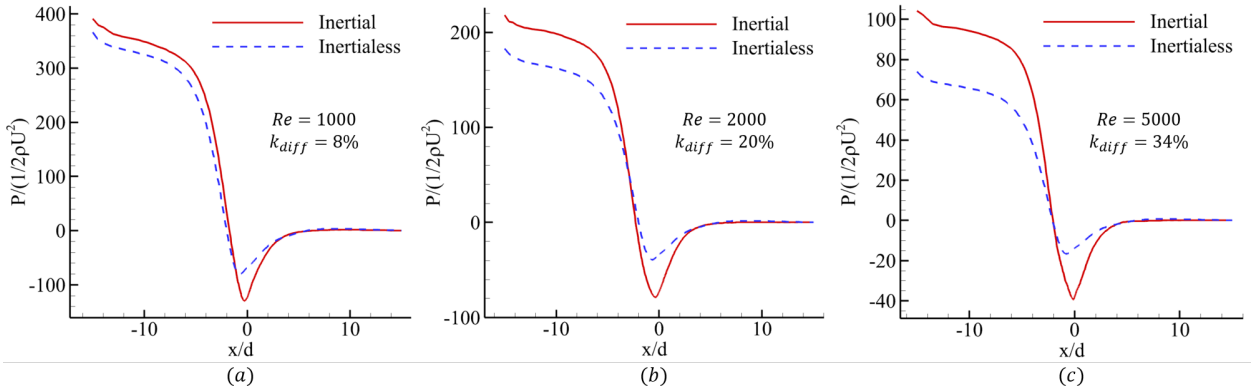

Figure 7.28: Effect of inertia forces on the pressure distribution for $Ha = 3000, Ha^* = 263.3$ for different Re.

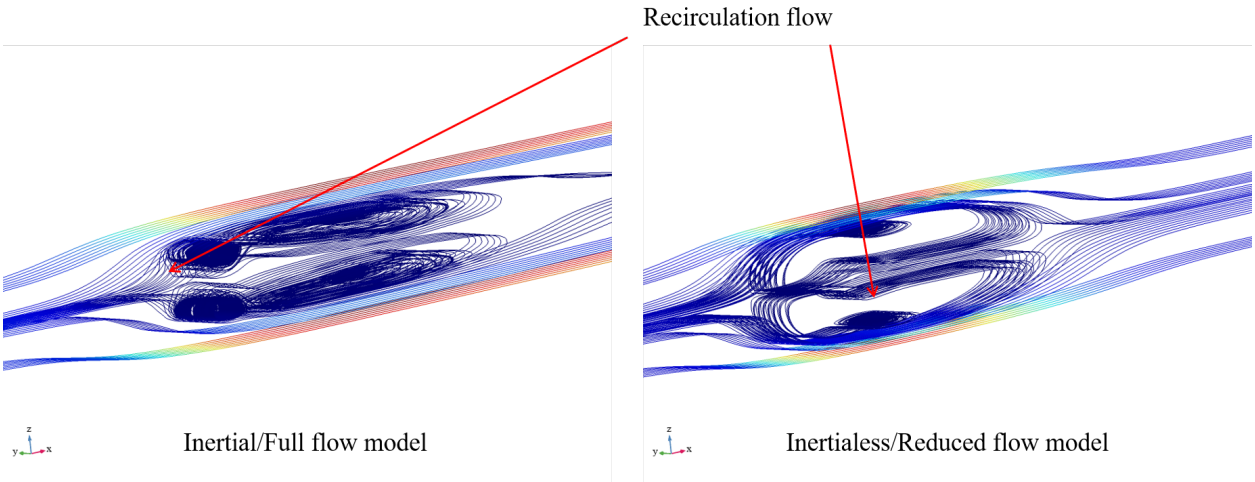

Figure 7.29: Recirculation flow bubble in 3D computed with and without inertia forces for $Ha = 3000, Re = 2000, Ha^* = 263.3$.

CHAPTER 8

Conclusions and future studies

In this dissertation, three topics related to liquid metal systems in DCLL blanket were investigated thoroughly through numerical analyses.

For the thermal convection loop simulation, the developed thermohydraulics code and the computational model in COMSOL Multiphysics are effective predictive capability tools for the design and analysis of a thermal convection loop, for the experimental planning and for the analysis of experimental data. The thermohydraulics code can especially be recommended for a rapid analysis when designing a new loop, while the COMSOL model allows for detailed computations of the 3D velocity and temperature field in the flowing fluid.

The main observations were made including elucidations of the flow phenomena and recommendations to the experimentalists. The conclusions are valid for the specific data range of $Ha \sim 10^4, Gr \sim 10^7$ and $Pr = 0.015$. The flow in the TCL is turbulent, of a circulation type, with the liquid flowing upwards in the hot leg and downwards in the cold leg. It is predicted that the $PbLi$ flow is about fully developed over the major length of the hot and cold leg and is in is steady state. The most significant changes in the flow occur in the corner regions where Dean vortices were observed in all computed cases. There is anti-symmetry between the cold and hot leg in both the velocity and temperature. Over the fully developed flow section, the temperature profile demonstrates only small variations in the radial direction. Placing samples inside the loop causes flow obstruction resulting in lower velocities, higher maximum temperatures and lower minimum temperatures. Using a permanent magnet $0.2 \sim 1T$ as a part of the electromagnetic flow meter can significantly

reduce the circulation velocity in the loop by a factor of $2 \sim 3$. The surface emissivity of the flow containing pipe is a very important parameter that needs to be carefully controlled in the experiments as its change in the course of the experimental studies (e.g. due to oxidation) can cause significant variance of the loop temperature.

The main accomplishment of the manifold study is the development of a correlation for the 3D MHD pressure drop in a non-conducting duct with a gradual expansion that occurs in the plane parallel to the applied magnetic field. The correlation was obtained in the wide range of flow parameters: $1000 < Ha < 10,000; 50 < Re < 10,000$ and $45^\circ < \theta < 75^\circ$. Although the magnitudes of Ha and Re in this study are significantly higher compared to other studies, they are still lower compared to the fusion blanket parameters where Ha and Re can be as high as 10^5. Therefore, more analysis at higher Ha and Re can be recommended in the future to proof the applicability of the obtained correlation to a real blanket or provide additional information that might help in constructing a better correlation. Also, a real manifold design may differ from that considered in this study. If the differences are not very significant, the obtained correlation can still be recommended for the pressure drop estimates. For example, the correlation could still be useful if the expansion angles $\sim 30^\circ$. For the expansion angle $\sim 90^\circ$, we recommend correlations obtained earlier for the duct with a sudden expansion by Rhodes et al [4]. The correlation can also be applied to the outlet manifold, in which the flow experiences contraction; as shown in [56], the difference in the MHD pressure drop between the expansion and contraction is not higher than 10%. The new correlation suggests a significant reduction in the MHD pressure drop at smaller expansion angles, but such manifold designs may require a long downstream section to assure that the flow at the exit of the manifold is uniform. The present study suggests that the flow development length can be as high as 20 expansion lengths at the highest Re numbers employed in these investigations. As shown in this study, the observed high MHD pressure drop is related to the thin internal boundary layer formed at the entrance to the expansion region. Here, significant changes occur not only in the pressure distribution but

also in the velocity field and induced electric currents. These observations are consistent with all previous computations for similar MHD flows where abrupt changes in the flow geometry occur, which are referred to in this article. However, it was found that the Ludford layer theory, which is often used to explain the 3D MHD pressure drop in the flows with expansions or contractions, is insufficient to explain the present results. The discrepancies can be attributed to the fact that the Ludford layer theory is limited to 2D MHD flows, while the present results suggest distinctive 3D flow features. Also, the Ludford layer theory cannot predict the formation of a recirculation zone, which was found in almost all computations in the present study and is one of the peculiar features of the MHD flow in a manifold. Due to the fact that the major designs for blanket involve poloidal manifold, the focus of recent studies are on this type of orientation in the paper where the magnetic field applied is parallel with the expansion. Some previous studies also took a look at the case with magnetic field in different directions. As to the expansion design, the wall shape can be linear or curved. The curved wall design is also interesting but may result in higher pressure drop, which is worth further examination.

In the study for flow in access duct, MHD flow in a non-conducting rectangular duct with applied fringing magnetic field was studied using COMSOL Multiphysics for the range of $1000 < Ha < 10000, 50 < Re < 10000, Ha^* = 175.5, 263.3, 438.8, 585.0$. The flow experiences 3D effects characterized by 3D MHD pressure drop, 3D electric currents and velocity changes. The sudden change of magnetic field is responsible for the generation of axial electric currents, and the Lorentz forces that influence velocity distribution. The flow enters the duct and becomes fully developed MHD flow in a short distance. In the middle of the duct, two counter-rotating vortices are formed and the majority of flow enters the side layers, which have high velocity near the wall. More downstream in the duct, the flow remains in the side layers for a long distance and re-enters the center of the duct. The recirculation zone length is related to Ha, Re, Ha^* and the size of vortex bubbles change with these parameters. The flow development length is also affected by Ha, Re, Ha^* and shows similar pattern as recir-

culation zone length. The most important feature – 3D MHD pressure drop was computed for a total of 80 cases. Since k cannot be related to Ha or Re alone, a linear regression analysis was carried out and $Ha^{1.33}Re^{-0.8}$ gave the best fit. Then the slop was fitted for different Ha^* to describe the pressure drop coefficient such that $k = f(Ha^*)Ha^{1.33}Re^{-0.8}$. The acquired correlation can be applied to future design of the breeding blanket for pressure loss estimation.

In real blanket, the Ha and Re are higher, which will cause difficulty in solving the problem. The purpose of the current study is to reveal the primary influence of a fringing magnetic field on liquid metal flow and to estimate 3D MHD pressure drop caused by sudden change of magnetic field. This is similar to what the flow will experience in the access duct in the inlet and outlet section. In this study, the highest Ha is 10,000 and Re is 10,000, and the magnetic field changes for $Ha^* = 175.5, 263.3, 438.8, 585.0$. The correlation established provides a good estimation through this data range, and can be potentially used in real blanket conditions. The computational model used in the current study is examined and verified for MHD flow simulation, which is not limited by the geometry. The geometry used in the study is a simple straight rectangular duct to take into consideration just the effect of fringing magnetic field on the flow. For DCLL blanket, the access duct is connected to the manifold, and further downstream flow channels, with also change of flow and duct directions. In this situation, it is hard to predict the flow characteristics and the source of the MHD pressure drop. However, the computational model can still be used to solve larger problems.

Further study should focus on testing the applicability of the correlation for 3D MHD pressure drop prediction of inlet access duct with similar fringing magnetic field, and at the same time the examination for precision of the MHD computational model on higher flow parameters. Such studies can make the design of the blanket to be more complete and help test the durability of the model and correlation obtained.

REFERENCES

[1] S. J. Pawel and K. A. Unocic. Compatibility of an FeCrAl alloy with flowing Pb-Li in a thermal convection loop. *Journal of Nuclear Materials*, 492:41–51, 2017.

[2] J. Jun, K. A. Unocic, M. J. Lance, H. M. Meyer III, and B. A. Pint. Compatibility of FeCrAlMo with flowing pbli at 500°-650°C. *Journal of Nuclear Materials*, 528:151847, 2020.

[3] S. Smolentsev. Private communication with Dr. S. Smolensev, 2020.

[4] T. J. Rhodes, S. Smolentsev, and M. A. Abdou. Magnetohydrodynamic pressure drop and flow balancing of liquid metal flow in a prototypic fusion blanket manifold. *Physics of Fluids*, 30(5):057101, 2018.

[5] C. B. Reed, B. F. Picologlou, T. Q. Hua, and J. S. Walker. ALEX results: a comparison of measurements from a round and a rectangular duct with 3-D code predictions. Technical report, Argonne National Lab., 1987.

[6] K. Miyazaki, K. Konishi, and S. Inoue. MHD pressure drop of liquid metal flow in circular duct under variable transverse magnetic field. *Journal of Nuclear Science and Technology*, 28(2):159–161, 1991.

[7] D. L. Smith, C. C. Baker, D. K. Sze, G. D. Morgan, M. A. Abdou, S. J. Piet, K. R. Schultz, R. W. Moir, and J. D. Gordon. Overview of the blanket comparison and selection study. *Fusion Technology*, 8(1P1):10–44, 1985.

[8] V. Dostal, P. Hejzlar, and M. J. Driscoll. The supercritical carbon dioxide power cycle: comparison to other advanced power cycles. *Nuclear Technology*, 154(3):283–301, 2006.

[9] P. Bondioli, C. Mariani, A. Lanzani, E. Fedeli, A. Mossa, and A. Muller. Lampante olive oil refining with supercritical carbon dioxide. *Journal of the American Oil Chemists' Society*, 69(5):477–480, 1992.

[10] D. E. Kim, M. H. Kim, J. E. Cha, and S. O. Kim. Numerical investigation on thermal–hydraulic performance of new printed circuit heat exchanger model. *Nuclear Engineering and Design*, 238(12):3269–3276, 2008.

[11] D. J. Close. The performance of solar water heaters with natural circulation. *Solar Energy*, 6(1):33–40, 1962.

[12] D. B. Kreitlow, G. M. Reistad, C. R. Miles, and G. G. Culver. Thermosyphon models for downhole heat exchanger applications in shallow geothermal systems. *Journal of Heat Transfer*, 100(4):713–719, 1978.

[13] H. Yamaguchi, X. Zhang, and K. Fujima. Basic study on new cryogenic refrigeration using CO2 solid–gas two phase flow. *International Journal of Refrigeration*, 31(3):404–410, 2008.

[14] H. Cohen and F. J. Bayley. Heat-transfer problems of liquid-cooled gas-turbine blades. *Proceedings of the Institution of Mechanical Engineers*, 169(1):1063–1080, 1955.

[15] H. R. McKee. Thermosiphon reboilers – a review. *Industrial & Engineering Chemistry*, 62(12):76–82, 1970.

[16] S. Kaga, T. Nomura, K. Seki, and A. Hirano. Development of compact inverter refrigerating system using R600a/CO2 by thermo-siphon. In *Proceedings of the 8th Gustav Lorentzen Conference on Natural Working Fluids, Copenhagen, Denmark*, pages 3–04, 2008.

[17] P. Sabharwall, Y. J. Yoo, Q. Wu, and J. J. Sienicki. Natural circulation and linear stability analysis for liquid-metal reactors with the effect of fluid axial conduction. *Nuclear Technology*, 178(3):298–317, 2012.

[18] B. T. Swapnalee and P. K. Vijayan. A generalized flow equation for single phase natural circulation loops obeying multiple friction laws. *International Journal of Heat and Mass Transfer*, 54(11-12):2618–2629, 2011.

[19] M. Broc, P. Fauvet, T. Flament, and J. Sannier. Compatibility of 316L stainless steel with liquid and solid tritium breeding materials. *Journal of Nuclear Materials*, 141:611–616, 1986.

[20] M. Broc, T. Flament, P. Fauvet, and J. Sannier. Corrosion of austenitic and martensitic stainless steels in flowing 17Li-83Pb alloy. *Journal of Nuclear Materials*, 155:710–714, 1988.

[21] G. Casini and J. Sannier. Research and development on liquid Pb-17Li breeder in europe. *Journal of Nuclear Materials*, 179:47–52, 1991.

[22] P. F. Tortorelli, J. H. DeVan, and J. E. Selle. Corrosion in lithium-stainless steel thermal-convection systems. Technical report, Oak Ridge National Lab., 1980.

[23] K. Britsch, M. Anderson, P. Brooks, and K. Sridharan. Natural circulation FLiBe loop overview. *International Journal of Heat and Mass Transfer*, 134:970–983, 2019.

[24] M. Kondo, K. Shibano, T. Tanaka, and T. Muroga. Heat-pulse flowmeter for a liquid breeder blanket. *Plasma and Fusion Research*, 8:2405086–2405086, 2013.

[25] P. F. Tortorelli and J. H. DeVan. *Thermal Convection Loop Study of the Corrosion of Fe-Ni-Cr Alloys by Molten NaNO3-KNO3*. Oak Ridge National Lab., 1982.

[26] M. A. Abdou, N. B. Morley, S. Smolentsev, A. Ying, S. Malang, A. Rowcliffe, and M. Ulrickson. Blanket/first wall challenges and required R&D on the pathway to DEMO. *Fusion Engineering and Design*, 100:2–43, 2015.

[27] J. Sannier, T. Flament, and A. Terlain. Corrosion of martensitic steels in flowing Pb17Li. In B.E. KEEN, M. HUGUET, and R. HEMSWORTH, editors, *Fusion Technology 1990*, pages 901–905. Elsevier, Oxford, 1991.

[28] S. Smolentsev, T. Rhodes, G. Pulugundla, C. Courtessole, M. Abdou, S. Malang, M. Tillack, and C. Kessel. Mhd thermohydraulics analysis and supporting r& d for dcll blanket in the fnsf. *Fusion Engineering and Design*, 135(B):314–323, 2018.

[29] S. Smolentsev. Physical background, computations and practical issues of the magnetohydrodynamic pressure drop in a fusion liquid metal blanket. *Fluids*, 6(3), 2021.

[30] J. C. R. Hunt and S. Leibovich. Magnetohydrodynamic flow in channels of variable cross-section with strong transverse magnetic fields. *Journal of Fluid Mechanics*, 28(2):241–260, 1967.

[31] S. Smolentsev, R. Moreau, L. Bühler, and C. Mistrangelo. MHD thermofluid issues of liquid-metal blankets: phenomena and advances. *Fusion Engineering and Design*, 85(7-9):1196–1205, 2010.

[32] J. Hartmann. *Theory of Laminar Flow of an Electrically Conductive Liquid in a Homogeneous Magnetic Field*. Munksgaard, 1937.

[33] J. A. Shercliff. Steady motion of conducting fluids in pipes under transverse magnetic fields. *Mathematical Proceedings of the Cambridge Philosophical Society*, 49(1):136–144, 1953.

[34] J. A. Shercliff. The flow of conducting fluids in circular pipes under transverse magnetic fields. *Journal of Fluid Mechanics*, 1(6):644–666, 1956.

[35] C. C. Chang and T. S. Lundgren. Duct flow in magnetohydrodynamics. *Zeitschrift für angewandte Mathematik und Physik ZAMP*, 12(2):100–114, 1961.

[36] J. C. R. Hunt. Magnetohydrodynamic flow in rectangular ducts. *Journal of Fluid Mechanics*, 21(4):577–590, 1965.

[37] J. C. R. Hunt and K. Stewartson. Magnetohydrodynamic flow in rectangular ducts. II. *Journal of Fluid Mechanics*, 23(3):563–581, 1965.

[38] J. S. Walker. Magneto-hydrodynamic flows in rectangular ducts with thin conducting walls. 1. constant-area and variable-area ducts with strong uniform magnetic-fields. *Journal de Mécanique*, 20(1):79–112, 1981.

[39] G. S. S. Ludford. Inviscid flow past a body at low magnetic Reynolds number. *Reviews of Modern Physics*, 32(4):1000, 1960.

[40] A. Sterl. Numerical simulation of liquid-metal MHD flows in rectangular ducts. *Journal of Fluid Mechanics*, 216(1):161–191, 1990.

[41] T. Zhou, Z. Meng, H. Zhang, H. Chen, and Y. Song. Code validation for the magnetohydrodynamic flow at high Hartmann number based on unstructured grid. *Fusion Engineering and Design*, 88(11):2885–2890, 2013.

[42] L. Bühler. Inertialess magnetohydrodynamic flows in expansions and contractions. In *FZK–6904*, 2003.

[43] S. Horanyi, L. Bühler, and E. Arbogast. Experiments on magnetohydrodynamic flows in a sudden expansion of rectangular ducts at high Hartmann numbers. In *Proceedings of the joint 15th Riga and 6th Pamir international conference*, volume 1, pages 243–246. Citeseer, 2005.

[44] C. Mistrangelo. *Three-dimensional MHD flow in Sudden Expansions*. Forschungszentrum Karlsruhe, 2006.

[45] C. Mistrangelo. Topological analysis of separation phenomena in liquid metal flow in sudden expansions. part 2. magnetohydrodynamic flow. *Journal of Fluid Mechanics*, 674:132–162, 2011.

[46] L. Bühler, S. Horanyi, and E. Arbogast. Experimental investigation of liquid-metal flows through a sudden expansion at fusion-relevant Hartmann numbers. *Fusion Engineering and Design*, 82(15-24):2239–2245, 2007.

[47] S. Molokov. *Liquid Metal Flows in Manifolds and Expansions of Insulating Rectangular Ducts in the Plane Perpendicular to a Strong Magnetic Field*. Kernforschungszentrum Karlsruhe, 1994.

[48] T. N. Aitov, A. I. Kalyutik, and A. V. Tananaev. Numerical analysis of three-dimensional MHD flow in channel with abrupt change of cross section. *Magnetohydrodynamics*, 19(2):223–229, 1983.

[49] M. V. Myasnikov and A. I. Kalyutic. Numerical simulation of incompressible MHD flows in channels with a sudden expansion. *Magnetohydrodynamics*, 33(4):342–349, 1997.

[50] H. Kumamaru. Numerical analyses on liquid-metal magnetohydrodynamic flow in sudden channel expansion. *Journal of Nuclear Science and Technology*, 54(2):242–252, 2017.

[51] C. N. Kim. Liquid metal magnetohydrodynamic flows in an electrically conducting rectangular duct with sudden expansion. *Computers & Fluids*, 89:232–241, 2014.

[52] C. N. Kim. A liquid metal magnetohydrodynamic duct flow with sudden contraction in a direction perpendicular to a magnetic field. *Computers & Fluids*, 108:156–167, 2015.

[53] H. Kumamaru. Numerical analyses on liquid-metal magnetohydrodynamic flow in sudden channel contraction. *Journal of Nuclear Science and Technology*, 54(12):1300–1309, 2017.

[54] L. Chen, S. Smolentsev, and M-J. Ni. Toward full simulations for a liquid metal blanket: MHD flow computations for a PbLi blanket prototype at Ha $\sim$ 104. *Nuclear Fusion*, 60(7):076003, 2020.

[55] S. Smolentsev, C. Wong, S. Malang, M. Dagher, and M. A. Abdou. MHD considerations for the DCLL inboard blanket and access ducts. *Fusion Engineering and Design*, 85(7-9):1007–1011, 2010.

[56] T. Rhodes and S. Smolentsev. Pressure drop in a prototypical 3D magnetohydrodynamic flow across contraction of a fusion blanket manifold. *Journal of Nuclear Science and Technology*, 2021.

[57] S. Smolentsev L. Chen and M.-J. Ni. Toward full simulations for a liquid metal blanket: part 2. computations of mhd flows with volumetric heating for a pbli blanket prototype at ha $\tilde{1}$04 and gr $\tilde{1}$012. *Nuclear Fusion*, 62(2):026042, jan 2022.

[58] E. V. Votyakov and E. Zienicke. Numerical study of liquid metal flow in a rectangular duct under the influence of a heterogenous magnetic field. *Fluid Dynamics and Materials Processing*, 3(2):97–114, 2007.

[59] R. Moreau, S. Smolentsev, and S. Cuevas. Flow in an insulated rectangular duct at the entry of a magnet. *Magnetohydrodynamics*, 45(2):181–192, 2009.

[60] T. Zhou, H. Chen, and Z. Yang. Effect of fringing magnetic field on magnetohydrodynamic flow in rectangular duct. *Fusion Engineering and Design*, 86(9-11):2352–2357, 2011.

[61] X. Albets-Chico, E. V. Votyakov, H. Radhakrishnan, and S. Kassinos. Effects of the consistency of the fringing magnetic field on direct numerical simulations of liquid–metal flow. *Fusion Engineering and Design*, 86(1):5–14, 2011.

[62] F. Li, D. Sutevski, S. Smolentsev, and M. A. Abdou. Experimental and numerical studies of pressure drop in pbli flows in a circular duct under non-uniform transverse magnetic field. *Fusion Engineering and Design*, 88(11):3060–3071, 2013.

[63] G. Pulugundla, S. Smolentsev, T. Rhodes, C. Kawczynski, and M. A. Abdou. Transition to a quasi-fully developed MHD flow in an electrically conducting pipe under a transverse non-uniform magnetic field. *Fusion Science and Technology*, 68(3):684–689, 2015.

[64] R. Moreau, S. Smolentsev, and S. Cuevas. MHD flow in an insulating rectangular duct under a non-uniform magnetic field. *PMC Physics B*, 3(1):1–43, 2010.

[65] Y. Li and O. Zikanov. Laminar pipe flow at the entrance into transverse magnetic field. *Fusion Engineering and Design*, 88(4):195–201, 2013.

[66] Stockholm COMSOL AB. *Sweden. COMSOL Multiphysics v. 5.4.* Accessed: Feb, 2018.

[67] H. F. Creveling, J. F. De Paz, J. Y. Baladi, and R. J. Schoenhals. Stability characteristics of a single-phase free convection loop. *Journal of Fluid Mechanics*, 67(1):65–84, 1975.

[68] B. E. Launder and B. I. Sharma. Application of the energy-dissipation model of turbulence to the calculation of flow near a spinning disc. *Letters in Heat and Mass Transfer*, 1(2):131–137, 1974.

[69] W. R. Dean. Fluid motion in a curved channel. *Proceedings of the Royal Society of London. Series A, Containing Papers of a Mathematical and Physical Character*, 121(787):402–420, 1928.

[70] V. A. Kalpakli. *Vortices in turbulent curved pipe flow-rocking, rolling and pulsating motions*. PhD thesis, KTH Royal Institute of Technology, 2014.

[71] P. M. Ligrani. A study of Dean vortex development and structure in a curved rectangular channel with aspect ratio of 40 at Dean numbers up to 430. Technical report, Naval Postgraduate School Monterey CA Dept OF Mechanical Engineering, 1994.

[72] Y. Jiang, S. Smolentsev, J. Jun, B. Pint, and C. Kessel. Prediction of PbLi fluid flow and temperature field in a thermal convection loop for qualification of fusion materials. *International Journal of Heat and Mass Transfer*, 172:121198, 2021.

[73] E. Mas de les Valls, L.A. Sedano, L. Batet, I. Ricapito, A. Aiello, O. Gastaldi, and F. Gabriel. Lead–lithium eutectic material database for nuclear fusion technology. *Journal of Nuclear Materials*, 376(3):353–357, 2008. Heavy Liquid Metal Cooled Reactors and Related Technologies.

[74] S. Smolentsev, M. Abdou, N.B. Morley, M. Sawan, S. Malang, and C. Wong. Numerical analysis of mhd flow and heat transfer in a poloidal channel of the dcll blanket with a sicf/sic flow channel insert. *Fusion Engineering and Design*, 81(1):549–553, 2006. Proceedings of the Seventh International Symposium on Fusion Nuclear Technology.

[75] H. Branover. *Magnetohydrodynamic Flow in Ducts*. Halsted Press, 1978.

[76] J. A. Shercliff. *The Theory of Electromagnetic Flow-measurement*. CUP Archive, 1962.

[77] V. A. Glukhih, A. V. Tananaev, and I. R. Kirillov. Magnetohydrodynamics in power engineering. *Energoatomizdat: Moscow*, 1987.

[78] U. Müller and L. Bühler. *Magnetofluiddynamics in Channels and Containers*. Springer Berlin, 2001.

[79] K. Miyazaki, S. Kotake, N. Yamaoka, S. Inoue, and Y. Fujii-E. MHD pressure drop of NaK flow in stainless steel pipe. *Nuclear Technology-Fusion*, 4(2P2):447–452, 1983.

[80] S. Smolentsev, T. Rhodes, Y. Jiang, P. Huang, and C. Kessel. Status and progress of liquid metal thermofluids modeling for the U.S. fusion nuclear science facility. *Fusion Science and Technology*, 2021, in press.

[81] A. Patel and R. Bhattacharyay. Application of ANSYS FLUENT MHD code for liquid metal magnetohydrodynamic studies. *Nuclear Fusion*, 59(9):096024, 2019.

[82] E. V. Votyakov and S. C. Kassinos. Simple models of heterogenous magnetic fields for liquid metal flow simulations. *Theoretical and Computational Fluid Dynamics*, 23(6):571–578, 2009.